Heitor Fernandes Credidio

Schramm-Loewner Evolutions of Strongly Anisotropic Systems

Fortaleza, Brasil

19 de Agosto de 2016

Heitor Fernandes Credidio

Schramm-Loewner Evolutions of Strongly Anisotropic Systems

Tese para obtenção de título de Doutor em Física da Matéria Condensada pela Universidade Federal do Ceará.

Universidade Federal do Ceará – UFC

Departamento de Física

Programa de Pós-Graduação

Orientador: Prof. Dr. André Auto Moreira

Fortaleza, Brasil

19 de Agosto de 2016

Heitor Fernandes Credidio

Schramm-Loewner Evolutions of Strongly Anisotropic Systems

Tese para obtenção de título de Doutor em Física da Matéria Condensada pela Universidade Federal do Ceará.

Prof. Dr. André Auto Moreira
Orientador

Prof. Dr. José Soares de Andrade Jr.
Universidade Federal do Ceará

Prof. Dr. Humberto de Andrade Carmona
Universidade Federal do Ceará

Prof. Dr. Roberto Fernandes Silva Andrade
Universidade Federal da Bahia

Prof. Dr. Giovani Lopes Vasconcelos
Universidade Federal de Pernambuco

Fortaleza, Brasil
19 de Agosto de 2016

Dados Internacionais de Catalogação na Publicação
Universidade Federal do Ceará
Biblioteca Universitária
Gerada automaticamente pelo módulo Catalog, mediante os dados fornecidos pelo(a) autor(a)

C935s Credidio, Heitor Fernandes.
Schramm-Loewner Evolutions of Strongly Anisotropic Systems / Heitor Fernandes Credidio. – 2016.
98 f. : il. color.

Tese (doutorado) – Universidade Federal do Ceará, Centro de Ciências, Programa de Pós-Graduação em Física , Fortaleza, 2016.
Orientação: Prof. Dr. André Auto Moreira.
Coorientação: Prof. Dr. José Soares de Andrade Jr..

1. Transições de Fase. 2. Física Estatística. 3. SLE. 4. Evoluções de Schramm-Loewner. I. Título.
CDD 530

Acknowledgements

I'd like to thank family, friends and all responsible directly or indirectly with the making of this work, specially my advisor Prof. André Auto Moreira, Prof. Hans Jürgen Herrmann and Prof. José Soares de Andrade Jr. Also government funding agencies CAPES, CNPq and Funcap.

Abstract

We disclose the origin of anisotropic percolation perimeters in terms of the Stochastic Loewner Evolution (SLE) process. Precisely, our results from extensive numerical simulations indicate that the perimeters of multi-layered and directed percolation clusters at criticality have as scaling limits the Loewner evolution of an anomalous Brownian motion, being superdiffusive and subdiffusive, respectively. The connection between anomalous diffusion and fractal anisotropy is further tested by using long-range power-law correlated time series (fractional Brownian motion) as driving functions in the evolution process. The fact that the resulting traces are distinctively anisotropic corroborates our hypothesis. Under the conceptual framework of SLE, our study therefore reveals new perspectives for mathematical and physical interpretations of non-Markovian processes in terms of anisotropic paths at criticality and vice-versa.

Keywords: SLE. Criticality. Percolation. Anisotropy.

Resumo

Usamos Evoluções de Schramm-Loewner (SLE) para expor a origem de interfaces anisotrópicas presentes em percolação. Mais precisamente, nossos resultados, obtidos através de extensas simulações numéricas, indicam que os perímetros de agregados encontrados em duas variantes do modelo de percolação têm como limite termodinâmico evoluções de Loewner dirigidas por movimentos Brownianos anômalos. Percolação em multi-camadas exibe comportamento superdifusivo e percolação direcionada subdifusivo. Testamos a conexão entre difusão anômala e anisotropia usando séries temporais com correlação de longo alcance em lei de potência (movimentos Brownianos fracionários) como funções diretoras nas SLE. Nossa hipótese é corroborada pelo fato de que os traços obtidos são distintamente anisotrópicos. Sob a estrutura conceitual das SLE, nosso estudo revela novas perspectivas para interpretações matemáticas e físicas de processos não-Markovianos em termos de caminhos anisotrópicos em criticalidade, e vice-versa.

Palavras-chaves: SLE. Criticalidade. Percolação. Anisotropia.

Contents

1 Introduction

The existence of phase transitions have been a part of the human experience ever since a person first boiled a pot of water, or saw the melting of snow. The observation that a substance can radically change its physical properties without changing its composition raises a number of questions that have only started to be answered in the last century or so. The quest for understanding what drives these changes on a microscopic level, and how it relates to the peculiar macroscopic behavior observed, is the starting point of the complex but profoundly insightful area of phase transitions and critical phenomena.

Although the phenomenon of phase transitions is known since immemorial time, the first scientific observation that can be linked to the modern theory of critical phenomena was made by Cagniard de La Tour in 1822 [1], who observed that the surface tension between the liquid and gas phases of several substances disappear under certain conditions of temperature and pressure, thus discovering what we call today a supercritical fluid phase. In 1869, Thomas Andrews coined the term *critical point* for the point in phase space where the liquid and gas phases become indistinguishable [2]. He also noted the milky opaque aspect the substances took when near the critical point, which he called critical opalescence. In 1895, Pierre Curie discovered the ferromagnetic transition, when a material lose its magnetic properties when subject to a high enough temperature [3]. More importantly, he was the first to notice universal characteristics in the behavior of different systems near the critical point. This property would eventually be regarded one of the pillars of critical phenomena theory [4].

At the same time as these discoveries were being made, a new area of physics was flourishing: statistical mechanics. After Gibb's foundational work [5] it was pretty clear that this new formalism was the perfect fit for exploring critical phenomena, which allowed the first half of the 20th century to bear witness to great advances including the introduction of the ubiquitous Ising model in 1925 [6] and its celebrated solution in 2D by Onsager in 1944 [7]. The 50's saw the introduction of the elegant and broadly applicable percolation theory by Broadbent and Hammersley [8].

What is considered the modern era of phase transitions started in the 60's when several theoreticians (including Heller [9], Domb [10], and many others [11]) came to the realization that the critical point exponents were entities that deserved special attention [4, 12]. This was followed by another major advance in the form of renormalization group theory, led by Leo Kadanoff [13].

The 80's saw the application of conformal invariance as an extension of scaling invariance, which, along with a well developed field theoretical apparatus, allowed for the

computation of the critical exponents of various models [14, 15]. Along that, propelled by the idea of self-organized criticality [16], the scope of applications for the concepts of scale invariance and criticality started expanding well beyond the physics realm, reaching areas as distinct as ecology, economics and social sciences [17, 18]. Also at the same time, new methods like the Coulomb gas [19, 20] allowed for a new perspective on how to study phase transitions, by looking at the interfaces present in critical systems instead of the fields themselves.

The last big theoretical step in phase transitions came from mathematicians unsatisfied with the many implicit assumptions and unproved statements that permeate quantum field theory [21, 22]. Using techniques from complex analysis developed in the 20's by Charles Loewner [23], Oded Schramm came up with an elegant formalism he called stochastic Loewner evolutions [24], but appropriately renamed Schramm-Loewner evolutions after its resounding success in explaining the critical properties of a number of phase transition models, most notably percolation. Not surprisingly the area yielded two Fields medals: one to Wendelin Werner, who was deeply involved in the early developments of the theory [25], and other to Stanislav Smirnov for using it to prove the conformal invariance of the percolation and Ising models [26]. Sadly Schramm himself was not awarded, as he was ineligible for being over 40 years old (by less than a month!).

The study of phase transitions and critical phenomena is a century-old theory in the making. In this work, we endeavor to take a small step in its development by exploring the critical properties of an often ignored class of systems, the ones that present strong anisotropy [27]. We will do that under the umbrella of the Schramm-Loewner evolution formalism, and, with help of numerical simulations, shed some light in the relationship between anomalously diffusive stochastic processes and anisotropic scaling.

2 Phase Transitions and Critical Phenomena

When trying to analyze a physical system, a big part of a physicist effort is dedicated to identifying the parts that compose the system and how they interact with each other. It is usually a daunting task to find an interaction model that captures all the relevant properties of a system. That is because the macroscopic (i.e. collective) behavior does not follow trivially from the microscopic forces in place. In no area of physics this is more clear than in that of phase transitions and critical phenomena. What is so special about the critical point, that allows a set of simple building blocks, which contain no global information about the system, display such a distinct and complex large scale behavior? This is the question scientists have been trying to solve in the last century or so, with each generation providing significant contributions to this end.

To start, let us take a step back and look at the building blocks of a physical system. These are the smallest subdivision that can be used to understand the system as whole. They can be elementary particles when studying high energy physics [28], living cells when observing the growing pattern of a colony of bacteria [29], or even people when studying crowd dynamics [30].

Many properties of such systems can be inferred by understanding their constituent parts, but what is more interesting is the fact that these building blocks can organize themselves in several different ways, each with radically different macroscopic behavior. The most elementary example here is water. Ice, vapor and liquid water are all composed of the same substance, H_2O, the only difference is how these molecules are arranged: immobile and organized when solid; moving through each other in a dense crowded mess as a liquid; and dashing chaotically and isolated in the gas state. See Figure 1 for an illustration of how a water molecule moves in the three states. Each pattern of organization is called a *phase*, and in which phase the systems finds itself depends on the value of some external parameters, normally the temperature (but not necessarily).

Not all systems have phases related with the states of matter, however. Some are related to magnetic or electric properties. This is the case of ferromagnetic materials, materials that exhibit a persistent magnetization after being subject to a strong magnetic field, like your everyday fridge magnet. This phenomenon is a result of the alignment of the magnetic spins of the atoms or molecules that compose the material. In contrast, paramagnetic materials show no permanent magnetization. If you take a magnet and raise its temperature, eventually the thermal fluctuations will misalign the spins, zeroing out the magnetization and turning the ferromagnetic material into a paramagnetic one. Other examples of phase transitions also include the transition of a material into a

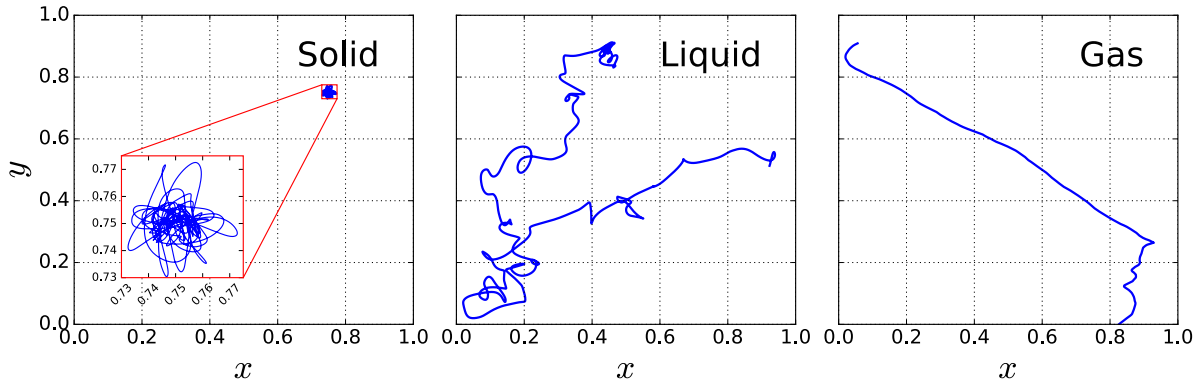

Figure 1 – How a system of particles behave in the three phases of matter. Here a simulation of 100 particles was done, but the trajectory of only one is shown. In the solid state the particles are confined to small region by the interactions of its neighbors. In the liquid state the particle is unconfined, but still interacts strongly with the other particles. In the gas state the kinetic energy of the particles is large enough that they barely interact with one another, making a ballistic trajectory until they make a head-on collision with another particle.

superconductive state [31] or when helium turns into into a superfluid [32], both happening at very low temperatures.

To better visualize the different phases of systems, it is common to make use of a *phase diagram*. Simply put, a phase diagram is a graph where each axis represent one control parameter, and every point in this graph is labeled according to the phase the system finds itself for that value of the parameters. Figure 2a shows the very famous phase diagram of water as a function of temperature and pressure. The three main phases (solid, liquid and gas) are clearly marked, and the black lines are the boundary between the phases. Crossing any of these lines is followed by a sharp change on the properties of the system, as described previously. This is know as a *phase transition*.

2.1 Classification of Phase Transitions

Phase transitions are usually classified into two categories: first and second order. There is no consensus on the precise definition of each, but this does not matter a lot, since they behave quite differently. An old, but still often used definition was proposed by Ehrenfest [34]. But, before we get into that, we have to find a quantitative way of describing the phase of a system. This is done by defining an *order parameter*, a quantity that take very distinct values in different phases (usually normalized to be zero in the most disordered phase). In the case of water, the order parameter is the density (which is just the inverse of the volume). For ferromagnetic transitions we use the spontaneous magnetization. The choice of order parameter for several systems can be seen in Table 1.

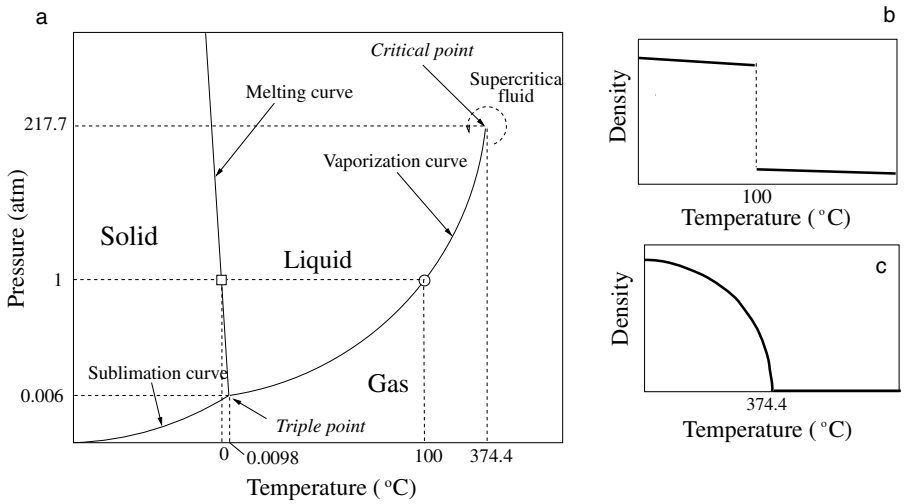

Figure 2 – Phase diagram of water (a). Here, the three usual phases are distinguished, each separated from the other by a coexistence line. The phase transition that happens when the system traverse a line is characterized by a discontinuous jump in the density, as shown in (b) for the liquid-gas transition at $P = 1$ atm. For $P = 217.7$ atm however the same transition is continuous, as shown in (c). In the vicinity of this phase transition, at $T \approx 374.4°\text{C}$, the two phases become indistinguishable, and display a number of peculiarities. Systems in such state are called critical systems. Reproduced from [33].

Following the example of water, where the temperature and pressure are the control variables, the thermodynamic properties are determined by the Gibbs free energy

$$G = E - TS + pV. \tag{2.1}$$

from which we can obtain the volume by taking its derivative

$$V = \left(\frac{\partial G}{\partial p}\right)_T. \tag{2.2}$$

If we now make an experimental apparatus to try and observe how the density of an amount of water behaves during a phase transition, say the liquid-gas transition, what we see is shown in Figure 2b. The density (and therefore the volume) makes a discontinuous jump.

This transition is characterized by the presence of latent heat, an amount of energy that the system releases or absorbs during a phase transition, which is a constant of the substance, and is independent on the temperature, pressure or other control parameters [42]. This means that when boiling a volume of water, the temperature of the liquid phase does not rise because the extra heat being added is being absorbed in form of latent heat. Because you add disorder to the system without changing its temperature, it happens that

Transition Type	Order Parameter	Example	T_c (K)
Liquid-gas	Molar volume	H_2O	647.05 [35]
Ferromagnetic	Magnetic moment	Fe	1044.0 [36]
Antiferromagnetic	Sublattice magnetic moment	FeF_2	78.26 [37]
λ-line in ^{4}He	^{4}He quantum mechanical amplitude	^{4}He	1.7–2.1 [38]
Superdonductivity	Electron pair amplitude	Pb	7.19 [9]
Binary fluid mixture	Fractional segregation of components	CCl_4-C_7F_{14}	301.78 [9]
Binary alloy	Fraction of one atomic species on one sublattice	Cu-Zn	739 [39]
Ferroelectric	Electric dipole moment	Triglycine sulfate	322.5 [40]

Table 1 – Examples of systems that display a second order phase transition. Reproduced from [41].

the entropy, another derivative of G,

$$S = -\left(\frac{\partial G}{\partial T}\right)_p, \tag{2.3}$$

is also discontinuous at the boundary of a phase transition. Because the first derivatives of the free energy display a discontinuity, we say these phase transitions are of *first order*. This sudden change happens because the equilibrium state of the system (determined by the minimum of the free energy) shifts from one part of the phase space to another [42], as illustrated in Figure 3. When the system is exactly at the boundary of the phase transition, the two phases have the same free energy, allowing them both to coexist in different regions of the system. Because of this, the transition lines are also called coexistence lines. On the point labeled triple point, the free energy has *three* equal minima, so all three phases (solid, liquid and gas) exist on the same system. Because the triple point is uniquely defined, it is the basis used to define the Kelvin temperature scale [43].

Now, looking again at Figure 2a one might ask why the liquid-gas transition line does not extend all the way through the phase diagram. This is where things start to get interesting. We have established that the free energy have two equivalent minima when the system is over the coexistence line. Now, if we walk along this line following the behavior of the free energy, what we observe is that the "dividing barrier" between the two minima gets shorter and shorter, similar to what is shown in Figure 4. At a critical temperature of approximately 374°C and pressure of 217.7atm, the two minima merge. At this point it is not that the two phases coexist, they are indistinguishable from one another.

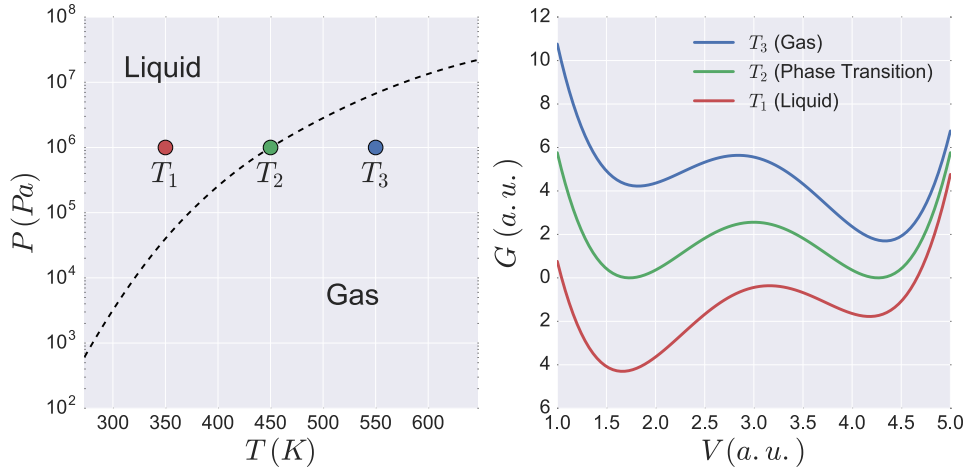

Figure 3 – Why first order transitions happen. The left graph shows three points on the phase space of water. The red one is in the liquid phase, the blue is in the gaseous state and the green right on the boundary. The right graph shows a heuristic construction of the Gibbs free energy in each of the three points (matched by color). The equilibrium state is the one of minimal free energy. Although G changes continuously with the temperature, the global minimum shifts abruptly once the phase boundary is crossed, thus occurring a first order phase transition. When the system is exactly on the boundary, the minima are equivalent, and the two phases coexist.

If we look at the order parameter when the system pass through the critical point, we see that it is no longer discontinuous, as it is shown in Figure 2c. If we set the pressure to the same as the critical point and heat an amount of liquid water, the volume will rise continuously (although not necessarily smoothly) until it reaches the gaseous state. Not all quantities are well behaved though. The ones that do display discontinuities on the critical point, are the second derivatives of the free energy, like the specific heat

$$c_p = T\left(\frac{\partial S}{\partial T}\right)_p = T\left(\frac{\partial^2 G}{\partial T^2}\right)_p, \tag{2.4}$$

or the isothermal compressibility

$$\kappa_T = -\frac{1}{V}\left(\frac{\partial V}{\partial p}\right)_T = -\frac{1}{V}\left(\frac{\partial^2 G}{\partial p^2}\right)_T. \tag{2.5}$$

Figure 5 shows two examples of such discontinuities in real system. Because the second derivative of the free energy is discontinuous, going through a critical point is know as a *second order* phase transition, and systems close to it are called *critical systems*.

Second order transitions have a whole range of peculiar behavior associated with it. The most notorious is the presence of large fluctuations. In Chapter 1 we mentioned the work of Thomas Andrews [2], who noticed that some substances become opaque at the critical point. This happens because the huge fluctuations in the spacial distribution

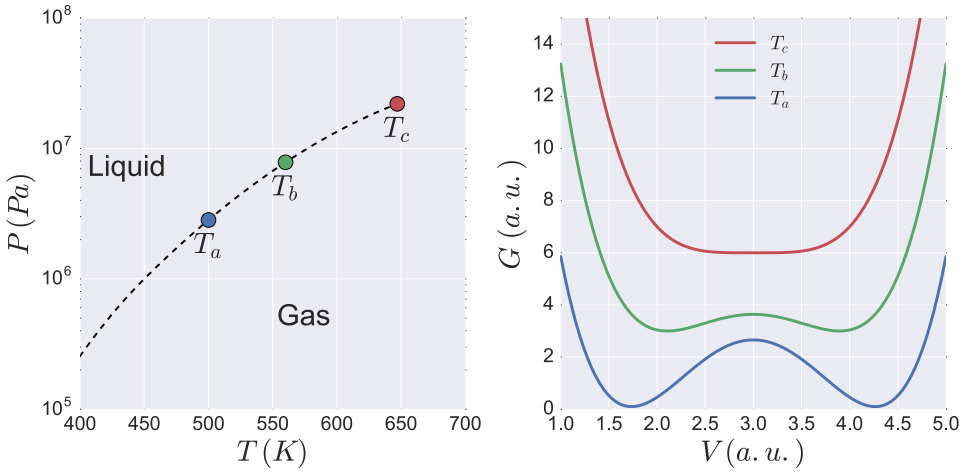

Figure 4 – If we follow the (heuristic) Gibbs free energy along the liquid-gas line, we observe that at some critical point T_c the two minima (related to the liquid and gas phases) coalesce into one. At this point the two phases are indistinguishable, which characterizes a second order phase transition. Systems close to the critical point are called critical systems.

of mass, forming water "droplets" of all sizes, including the sizes that scatter most visible light, giving the system a milky aspect.

Although we focused a lot on the example of water, the ferromagnetic transition described in the previous section is probably the most studied kind of second order phase transition. Its free energy is given by

$$dF = -SdT - Mdh \tag{2.6}$$

where M is the spontaneous magnetization (the order parameter in this case) and h is an uniform external magnetic field. It is characterized by a diverging magnetic susceptibility

$$\chi_M = \left(\frac{\partial M}{\partial h}\right)_T = -\left(\frac{\partial^2 F}{\partial h^2}\right)_T. \tag{2.7}$$

Not all phase transitions fall neatly into these two categories, however. The Kosterlitz-Thouless transition of the XY-Model (related to some superconducting transitions [46]) could be considered of infinite order, because the free energy is infinitely differentiable [47], although it shares some similarities with second order transitions.

The discussion of phase transitions presented so far, rooted on the postulates of thermodynamics and in the analyticity of the free energy, is due to Landau [48]. While this theory manages to capture a few properties of critical systems, it fails catastrophically from a quantitative standpoint. The source of this discrepancy comes from some basic assumptions of statistical mechanics. You see, the maximum entropy postulate is derived from the fact that the probability of finding a system in any given state is distributed very

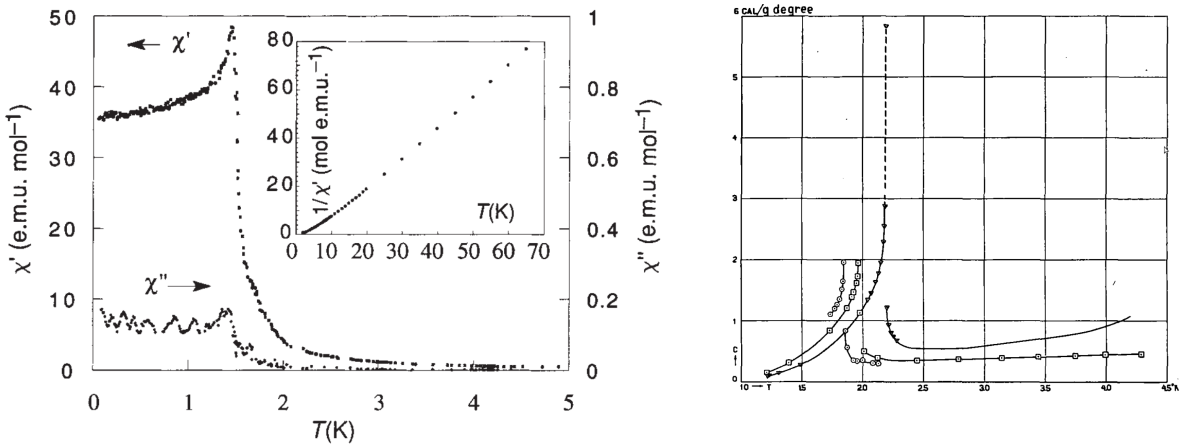

Figure 5 – Examples of thermodynamical quantities in the vicinity of a second order phase transitions. The left graph shows the diverging magnetic susceptibility on the ferromagnetic transition of dupeyredioxyl [44]. The graph on the right shows the diverging specific heat of the lambda transition of superfluid helium-4 [45].

narrowly around a value, this way we can assume the expected (average) energy of the system is the same as the most probable one. On the critical point however, because the minimum of the free energy is so shallow, the probability distribution broadens significantly, so much that the difference between most probable and average cannot be ignored [42].

2.2 Critical Exponents and Universality

We noted that several thermodynamical quantities diverge on the critical point. More important than that is to know *how* they diverge. This motivates the definition of a set of indices called *critical exponents* that characterize the behavior of the system near the critical point. Here we will use ϕ for the order parameter (the density for water, the magnetization for ferromagnets) and J for the source field (pressure for water, the external magnetic field for ferromagnets). This way we can define a generalized susceptibility $\chi = \partial\phi/\partial J$ and specific heat $c = -\partial^2 f/\partial T^2$.

In the thermodynamics domain there are four main critical exponents, each associated with a different quantity. We have the heat capacity exponent α

$$\begin{aligned} c &\sim (T - T_c)^{-\alpha} \quad \text{for} \quad T > T_c \\ c &\sim (T_c - T)^{-\alpha'} \quad \text{for} \quad T < T_c, \end{aligned} \tag{2.8}$$

the order parameter exponent β, when taken along the coexistence curve

$$\phi \sim (T_c - T)^{\beta} \quad \text{for} \quad T < T_c, \tag{2.9}$$

the generalized susceptibility exponent γ

$$\begin{array}{rcll} \chi & \sim & (T - T_c)^{-\gamma} & \text{for} \quad T > T_c \\ \chi & \sim & (T_c - T)^{-\gamma'} & \text{for} \quad T < T_c, \end{array} \tag{2.10}$$

and the order parameter exponent δ, when taken at constant temperature $T = T_c$

$$\phi \sim (J - J_c)^{1/\delta} \quad \text{for} \quad J > J_c. \tag{2.11}$$

These exponents may have different values if you take the limit from above or bellow the critical point (unprimed and primed symbols respectively), but unless explicitly noted, we will assume that they are the same, which happens often.

There are many other critical exponents outside the realm of thermodynamics. These exponents can only be studied by a full statistical mechanical framework. Two of the most important ones are related to the correlations of the system. Take the ferromagnetic transition, for instance. The influence of an individual spin is usually restricted over a finite region around it. That is to say, there is a length scale ξ that if we take two spins separated by a distance $r \ll \xi$ and flip one of the spins, the other is very likely to also flip. In the unordered (paramagnetic) phase, ξ is small because the thermal fluctuations inhibit long range correlations. On the ordered (ferromagnetic) phase, the influence of large clusters of aligned spins is stronger than that of a single one, also hindering the range of correlations. We see that too much order, as well as too much disorder, have the effect of restricting the influence of the spins over each another. Therefore, it makes sense to think that somewhere in between there is a sweet spot where the balance between order and disorder makes the correlation length as large as possible.

We can formalize this thought by defining the correlation function of a system

$$C_\phi \left(|\mathbf{r_1} - \mathbf{r_2}| \right) = \left\langle \phi \left(\mathbf{r_1} \right) \phi \left(\mathbf{r_2} \right) \right\rangle - \left\langle \phi \left(\mathbf{r_1} \right) \right\rangle \left\langle \phi \left(\mathbf{r_2} \right) \right\rangle \tag{2.12}$$

where $\phi(\mathbf{r})$ is the local value of the order parameter at any given point of the system. The macroscopic value can be recovered from its expected value $\phi = V^{-1} \int \phi(x) d^d x$. The assumption that $C(\mathbf{r_1}, \mathbf{r_2}) = C(|\mathbf{r_1} - \mathbf{r_2}|)$ comes from translation invariance, which takes no specific point of the system as special. It is natural to expect that the correlations would decay exponentially, with a decay constant ξ

$$C(r) \sim e^{-r/\xi}. \tag{2.13}$$

The relation between thermodynamics and the correlation function is governed by the fluctuation-dissipation theorem [15]

$$\chi = \frac{\partial \phi}{\partial J} = \frac{1}{T} \int C(r)\, dr. \tag{2.14}$$

We know that on the critical point χ diverges, but the integral on the right-hand side cannot diverge for finite ξ, given Eq. 2.13. The conclusion is simple, not only the correlation

length is maximal at the critical point, it is infinite! This divergence also has a critical exponent ν associated with it

$$\begin{aligned} \xi &\sim (T - T_c)^{-\nu} \quad \text{for} \quad T > T_c \\ \xi &\sim (T_c - T)^{-\nu'} \quad \text{for} \quad T < T_c. \end{aligned} \tag{2.15}$$

At the critical point, the correlation function itself also cannot decay as an exponential, and goes instead as a power law, with yet another critical exponent η

$$C(r) \sim r^{-d+2-\eta} \quad \text{for} \quad T = T_c. \tag{2.16}$$

where d is the number of spatial dimensions (usually 2 or 3, but it is often useful to leave it as a variable parameter [49]). Many authors consider this fact, that very distant particles can influence the state of each other, to be the defining characteristic of a second order phase transition.

The most notable consequence of the dominance of long range correlations is that the critical behavior of the system is determined by the general properties of the fluctuations, which in turn are mainly determined by the dimensionality of the system and of the order parameter, and not by the details of the material that compose the system [4]. As a consequence, all systems tend to group themselves into classes that share the same critical exponents. These are called *universality classes*. For example, the liquid-gas transition falls in the same universality class as the ferromagnetic transition [54]. Table 2 show some examples of universality classes, systems that belong to it, and the values of their critical exponents.

Class	**Examples**	$\boldsymbol{\alpha}$	$\boldsymbol{\beta}$	$\boldsymbol{\gamma}$	$\boldsymbol{\delta}$	$\boldsymbol{\nu}$	$\boldsymbol{\eta}$
Mean Field	—	0	1/2	1	3	1/2	0
2D Ising	Ferromagnet	0	1/8	7/4	15	1	1/4
3D Ising	Liquid-Vapor	0.11	0.33	1.24	4.79	0.63	0.036
3D XY-Model	Superfluid ^{4}He	−0.015	0.348	1.31	4.78	0.671	0.038
2D Percolation	Porous Media	−2/3	5/36	43/18	91/5	4/3	5/24

Table 2 – Non exaustive list of critical exponents of various universlity classes [42, 7, 50, 51, 52, 53]. The mean field is the result found using the Landau approach shown in Section 2.1, it is an approximation of high dimensional systems.

2.3 Scaling Invariance

The list of critical exponents shown on the last section is far from exhaustive. More exotic, but no less important exponents include the fractal dimension [55], one-arm exponent [56] and the crossing exponent [57], among others. It sure seems like a lot of work to completely describe a universality class, if one needs to compute dozens of exponents. Luckily with the very simple assumption of scaling invariance, we can greatly reduce the amount of work needed.

We will take a look at the correlation functions of the observables, which we will refer as *scaling operators*. The main ones are the order parameter distribution $\phi(\mathbf{r})$ and energy density $\varepsilon(\mathbf{r})$. The two-point correlation function of these fields is defined according to Eq. 2.12

$$C_\phi\left(|\mathbf{r_1}-\mathbf{r_2}|\right) = \left\langle\phi\left(\mathbf{r_1}\right)\phi\left(\mathbf{r_2}\right)\right\rangle - \left\langle\phi\left(\mathbf{r_1}\right)\right\rangle\left\langle\phi\left(\mathbf{r_2}\right)\right\rangle, \tag{2.17}$$

$$C_\varepsilon\left(|\mathbf{r_1}-\mathbf{r_2}|\right) = \left\langle\varepsilon\left(\mathbf{r_1}\right)\varepsilon\left(\mathbf{r_2}\right)\right\rangle - \left\langle\varepsilon\left(\mathbf{r_1}\right)\right\rangle\left\langle\varepsilon\left(\mathbf{r_2}\right)\right\rangle. \tag{2.18}$$

They are given in terms of the reduced temperature and source field

$$t = \frac{T-T_c}{T_c}, \qquad h = \frac{J-J_c}{J_c}, \tag{2.19}$$

so the critical point is exactly at $t=0$ and $h=0$. These are also known as *scaling fields*.

The scaling hypothesis postulates that the correlation functions transform under a scaling transformation $\mathbf{r}\to\mathbf{r}/b$ in the following way

$$C_\phi\left(\mathbf{r};t,h\right) = b^{-2x_\phi}C_\phi\left(\mathbf{r}/b;tb^{y_t},hb^{y_h}\right) \tag{2.20}$$

$$C_\varepsilon\left(\mathbf{r};t,h\right) = b^{-2x_\varepsilon}C_\varepsilon\left(\mathbf{r}/b;tb^{y_t},hb^{y_h}\right) \tag{2.21}$$

where x_ϕ and x_ε are the *scaling dimension* of the scaling operators ϕ and ε, and y_t and y_h are called the *renormalization group eigenvalues* of their respective scaling fields.

Following the fluctuation-dissipation theorem, Eq. 2.14, we can compute the susceptibility and the specific heat by integrating C_ϕ and C_ε respectively. This give us

$$\chi\left(t,h\right) = b^{d-2x_\phi}\chi\left(tb^{y_t},hb^{y_h}\right) \tag{2.22}$$

$$c\left(t,h\right) = b^{d-2x_\varepsilon}c\left(tb^{y_t},hb^{y_h}\right) \tag{2.23}$$

Recall that $\chi=-\partial^2 f/\partial h^2$ and $c=-\partial^2 f/\partial t^2$, therefore we can integrate Eq. 2.22 and 2.23 twice, obtaining the free energy density $f=F/\mathcal{N}$

$$f\left(t,h\right) = b^{d-2x_\phi-2y_h}f\left(tb^{y_t},hb^{y_h}\right) = b^{d-2x_\varepsilon-2y_t}f\left(tb^{y_t},hb^{y_h}\right), \tag{2.24}$$

from which we can deduce that $x_\phi+y_h=x_\varepsilon+y_t$. As a matter of fact, the sum is constant for all pairs of scaling dimension and its conjugate renormalization group eigenvalue. Since

this sum does not depend on the fields themselves, it is safe to assume they depend on the only other parameter, the number of spatial dimensions, that is

$$x_\phi + y_h = x_\varepsilon + y_t = d \tag{2.25}$$

which leaves us with the neat relation

$$f(t,h) = b^{-d} f\left(tb^{y_t}, hb^{y_h}\right). \tag{2.26}$$

It is worth noting that this is not really the free energy of the system. The actual free energy have a singular and a regular part, the one described so far is the singular part. Near the critical point, however, only the singular part makes significant contributions to the behavior of the system, so we can safely ignore the regular part.

The next step is to make the scaling parameter b a function of the temperature, in order to get rid of one of the arguments of the free energy. This can be done by making $b = t^{-1/y_t}$, which yields

$$f(t,h) = t^{d/y_t} f\left(1, ht^{-y_h/y_t}\right) = t^{d/y_t} \Psi\left(ht^{-y_h/y_t}\right), \tag{2.27}$$

where Ψ is known as a scaling function, and it is unique for a given universality class. We can re-obtain the heat capacity by taking the second derivative as usual

$$c = -\left.\frac{\partial^2 f}{\partial t^2}\right|_{h=0} \sim |t|^{d/y_h - 2}. \tag{2.28}$$

Which is the expected behavior, and from Eq. 2.8 we have that $\alpha = 2 - d/y_t$. A similar process can be done to derive a similar relation for all four thermodynamical exponents

$$\alpha = 2 - d/y_t \tag{2.29}$$
$$\beta = (d - y_h)/y_t \tag{2.30}$$
$$\gamma = (2y_h - d)/y_t \tag{2.31}$$
$$\delta = y_h/(d - y_h). \tag{2.32}$$

This system of equations can be solved to single out the eigenvalues obtaining the relations

$$\alpha + 2\beta + \gamma = 2 \tag{2.33}$$
$$\alpha + \beta(1 + \delta) = 2, \tag{2.34}$$

These are know as *scaling relations* [58, 59], and are some of the greatest results of the scaling hypothesis, because if you know the value of two of the thermodynamical exponents, you get the other two for free.

How about the other two exponents, ν and η, related to the correlations of the order parameter, you might ask. We can also find a simple relation for them by taking Eq. 2.20 and again making $b = t^{-1/y_t}$

$$C_\phi(\mathbf{r}; t, 0) = t^{2x_\phi/y_t} C_\phi\left(\frac{\mathbf{r}}{(1/t)^{1/y_t}}; 1, 0\right). \tag{2.35}$$

We can assume that close to criticality (but not exactly on the critical point) the correlation function depends only on r/ξ, because of Eq. 2.13. From this follows that

$$\xi \sim |t|^{-1/y_t}, \tag{2.36}$$

which, using Eq. 2.15, implies that

$$\nu = \frac{1}{y_t}. \tag{2.37}$$

Now we can repeat the process by making $b = r$ and $t = 0$, which will give us

$$C_\phi(r; 0, 0) = r^{-2d+2y_h}. \tag{2.38}$$

Comparing with Eqs. 2.16 and 2.25, gives the relation for η

$$\eta = d - 2y_h + 2. \tag{2.39}$$

Finally we can find a relation between ν and η using Eqs. 2.29–2.32, 2.37 and 2.39.

$$\gamma = \nu(2 - \eta) \tag{2.40}$$

$$\alpha = 2 - d\nu. \tag{2.41}$$

These are known as *hyperscaling relations*, and amazingly no new critical exponent is needed to determine them, that is, only two are necessary to completely describe the critical exponents of a second-order phase transition, which is very convenient. Sadly the hyperscaling relations are not as sturdy as the scaling relations and can break down under the presence of dangerously irrelevant operators [60].

The arguments and assumptions used throughout this section were historically motivated through the study of renormalization group theory [61], which was an important advancement in critical phenomena when it was first developed, but it goes well beyond the scope of this work. However, some authors do prefer to look at scaling invariance through an axiomatic lens, as it was done here, forming a parallel with the introduction of conformal invariance (see Section 2.6) [15].

2.4 Models of Critical Systems

Beyond the phenomenological approach shown up to this point, another way to advance the knowledge of statistical physics is through model building, where we look for simple models capable of providing useful insight into practical situations. Coming up with a fruitful model however can be a very tiresome and sometimes arcane task, with a lot of trial and error involved. Over decades of study, a select group of models have gained a significant status in the canon of phase transitions. Two that stand out due to their simplicity and historical significance are the Ising and percolation models.

2.4.1 Ising Model

Of all phase transition models, Ising's is definitely the most famous, because, despite its simplicity, it is capable of capturing all of the main features of ferromagnetic materials near the critical point. I was also the first model with a second order phase transition to be analytically solved, and because of that, today it forms the basis of our understanding of phase transitions to the point that many latter important models, like the $O(n)$ and Potts models [52], can be traced back to it.

Simply put, the model consists of a set of classical spins $\{s_i\}$, each taking one of two values: 1 or -1. They are arranged in a lattice and are allowed to interact with their nearest neighbors. The Hamiltonian of this system is given by

$$\mathcal{H} = -J \sum_{\langle i,j \rangle} s_i s_j - h \sum_i s_i, \tag{2.42}$$

Where $\sum_{\langle i,j \rangle}$ means a summation over all pairs of nearest neighbors, and J is the interaction coupling parameter. If we assume $J > 0$, then the first term of the Hamiltonian favors the alignment of the spins, while the second one favors the alignment with an external magnetic field. See Figure 6 for some configurations $\{s_i\}$ of the Ising model in two dimensions in a square lattice, which according to statistical mechanics are distributed with the probability

$$P\left(\{s_i\}\right) = \frac{e^{-\mathcal{H}(\{s_i\})/k_b T}}{\sum_{\{s_j\}} e^{-\mathcal{H}(\{s_j\})/k_b T}}. \tag{2.43}$$

We can see that for higher temperatures, more disordered states (which have higher energy) are more probable.

The order parameter here is the spontaneous magnetization $M = \sum_i s_i/N$. If the temperature is too low the spins will tend to align themselves, giving rise to an ordered state where $M > 0$, while if the temperature is too high, thermal fluctuations will misalign the spins, resulting in a highly disordered state with $M = 0$.

In his original work [6], Ising solved the model in one dimension, showing that it does not undergoes a phase transition at finite temperature. From this result, he mistakenly assumed the same would happen in higher dimensions. The argument is apparently sound: any configuration of the system with magnetization M have the same energy as the one where all the spins are flipped and the magnetization is opposite $-M$. Both configurations have therefore the same probability $\exp(-E/k_b T)$. The system should then spend as much time on a positive magnetization as in a negative one, so the average magnetization should be zero. On the other hand, Peierls presented an argument for the presence of phase transitions in $d > 1$ [62], showing that in large enough systems (that is, in the thermodynamic limit) the thermal fluctuations at low temperatures are not enough to bring the system from a positive magnetization state to a negative one (and vice-versa), so the system would be "stuck" with non-zero magnetization.

The fact that both of these contradictory arguments seemed correct, led some to believe that statistical mechanics was inadequate to deal with critical systems. The solution for this conundrum came from Onsager in 1944 [7] who solved the Ising model in a 2D square lattice. The solution, albeit very complex, demanded no further assumptions than that of standard statistical physics, a truly remarkable and well celebrated result. The mistake in Ising's argument lies on the partition function,

$$\mathcal{Z} = \sum_{\{s_i\}} \exp\left[-\frac{\mathcal{H}\left(\{s_i\}\right)}{k_b T}\right], \tag{2.44}$$

from which follow all thermodynamic properties [63]. The partition function is certainly analytical in T for a finite system, because the number of different configurations $\{s_i\}$ is finite, and a finite sum of exponentials is an analytical function. However, if the number of configurations is infinite, which should happen in the thermodynamic limit, the analyticity cannot be guaranteed, and the singularities typical of a second order phase transition are allowed to come about.

Let us take a look at the phase diagram of the Ising model. Figure 7 shows the 2D square lattice version. We observe a first order phase transition at $h = 0$ and $T < T_c$, where the magnetization discontinuously flips direction. At $T = T_c$ the transition becomes continuous. The value of the critical point is given by

$$T_c = \frac{2J}{k_b \log\left(1+\sqrt{2}\right)} \approx 2.27 \frac{J}{k_b}, \tag{2.45}$$

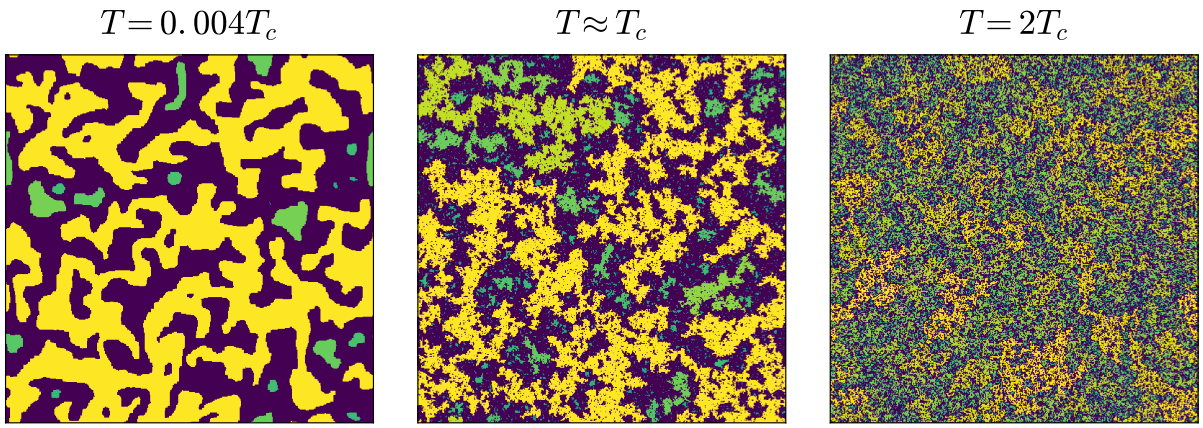

Figure 6 – Realizations of the Ising model with three different temperatures. The clusters of adjacent spin-up sites are colored according to how many sites belong to it. The subcritical regime is dominated by the large clusters. On the other hand, above the critical point, the system is dominated by thermal fluctuations, undermining cluster formation. At the critical point however, the clusters lack a characteristic length scale. One can observe that the image has a certain "depth" to it. This happens because clusters of all sizes are present, a mark of scale invariance, the most important property of critical systems.

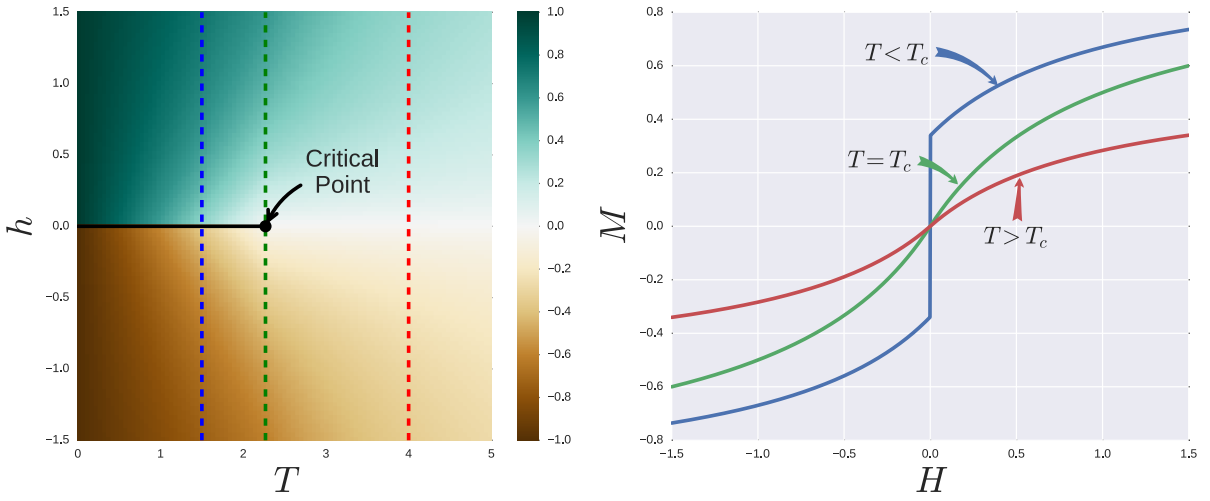

Figure 7 – The phase space of the Ising model (left). The color represents the spontaneous magnetization M as a function of the external magnetic field h and temperature T. The black line represents the coexistence line where the phase transition is of first order, which means the magnetization changes discontinuously like it is shown in the blue line. In the critical point (green line), the change becomes continuous and a second order phase transition takes place. Beyond this point (red line), the transition is always continuous.

and the magnetization along the coexistence line is [64]

$$M = \left[1 - \sinh^{-4}\left(\frac{2J}{k_b T}\right)\right]^{1/8}. \tag{2.46}$$

See Figure 8 for the overall behavior of M. From Eq. 2.46 we can determine that $\beta = 1/8$. The values of the other exponents of the Ising universality class can be seen in Table 2. The Ising universality class encompass more than just the ferromagnetic transition. For instance, the liquid-vapor critical point (like the one found in the water phase diagram) also falls in the same class. To this day no exact solution for three dimensions have been presented, as it happens with most higher dimension models.

2.4.2 Percolation

While fiercely competing with the Ising model in terms of popularity, percolation certainly wins in terms of simplicity. Introduced in 1957 by Broadbent and Hammersley [8], the question they were trying to answer was very humble: say we block a water pipe with a rock, how porous should the rock be for the water to be able to flow, even if at a very low rate? To find an answer, they modeled the rock as a square lattice where each site can be either occupied by the rocky substrate or a hole. The measure of the porosity is the ratio between the number of holes and the total number of sites in the lattice. Of course, the more porous is a rock, the more holes it has. Assuming these holes are randomly and

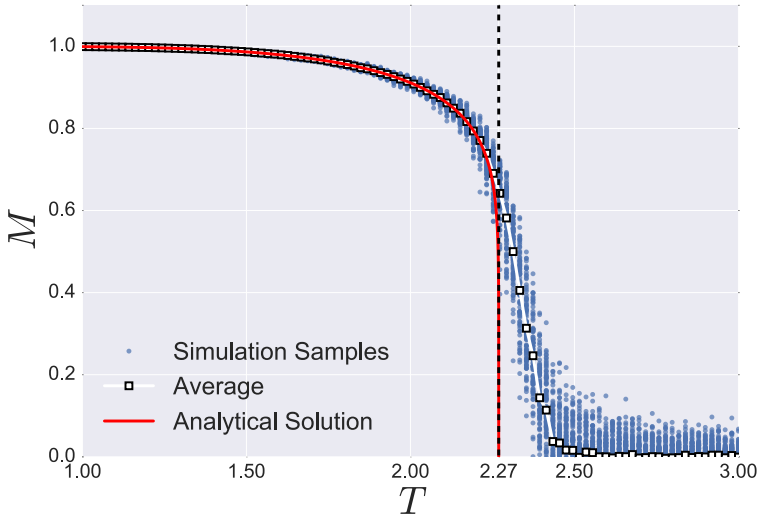

Figure 8 – Spontaneous magnetization as a function of temperature for the Ising model. The simulations were performed in a 128×128 square lattice. As temperature rises, thermal fluctuations dominate the spin dynamics destroying the correlations. Above the critical temperature of $T_c = 2/\log(1+\sqrt{2}) \approx 2.269$ the value of M should reach zero, although due to finite size effects we still observe some magnetization beyond this point. The red line shows the illustrious solution developed by Onsager [7], where $M = \left[1 - (\sinh 2/T)^{-4}\right]^{1/8}$.

uniformly distributed on the substrate, they will often, by pure chance, fall into clusters of neighboring holes, which are in fact just bigger holes. Water will be able to flow through the rock only if we have a cluster that traverse the system from one side to the other. This cluster is called the *percolating* (or spanning) cluster. So we can reframe the initial question

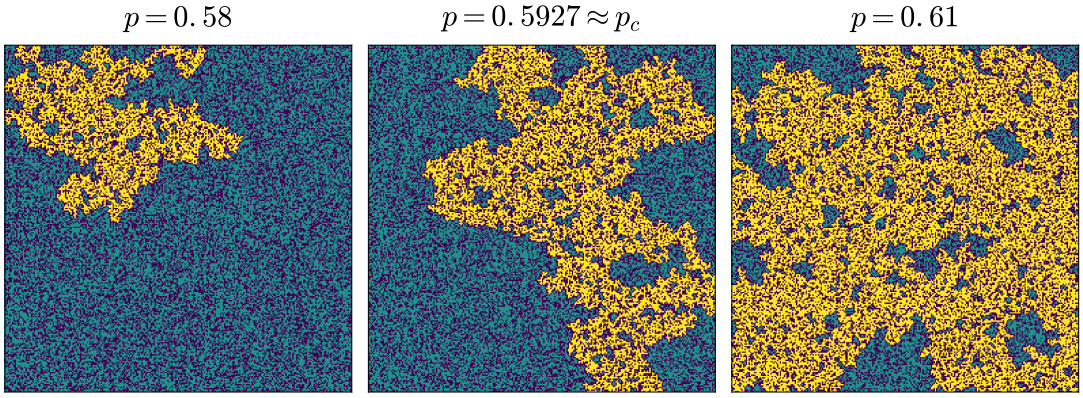

Figure 9 – Percolation model with three different occupation probabilities p. Black sites are unoccupied, blue ones are occupied, and the largest cluster is painted yellow. We only observe a spanning cluster connecting different sides of the system when $p \geq p_c$.

as follows: whats the smallest value of porosity where a percolating cluster will always be present in the system. A 0% porous rock would obviously always be impermeable, and a 100% porous rock is just no rock at all. But how about 50%, or 40%, or 60%? The answer naturally depends on the size of the lattice, but for a very large one we observe the existence of a critical porosity p_c below which we never observe a percolating cluster, while above p_c one is away present. See Figure 9 for some realizations of the percolation process in two dimensions in each state: subcritical, critical and supercritical.

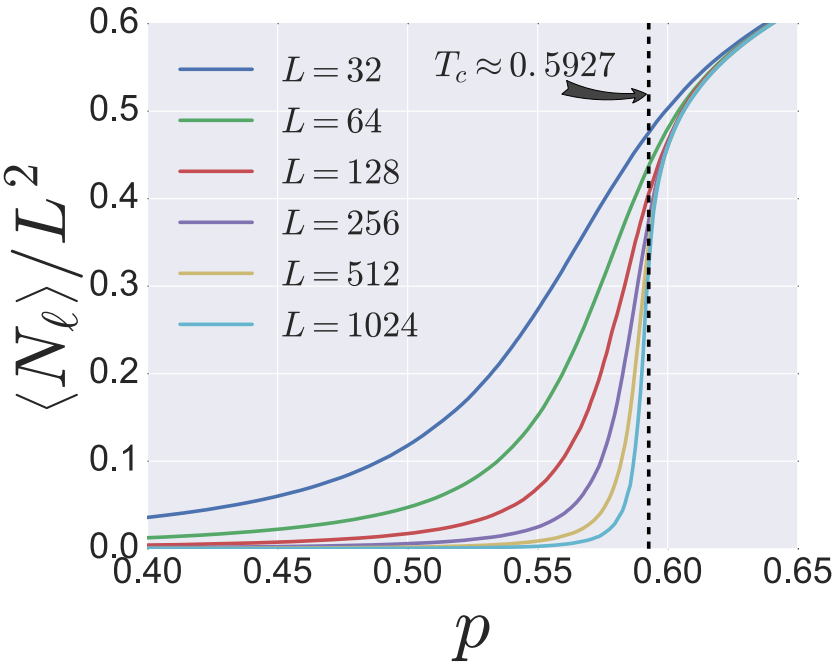

Figure 10 – The order parameter of the percolation model as a function of the occupation probability for various system sizes. The order parameter here is defined as the fraction of the system occupied by the largest cluster. In the thermodynamical limit, the largest cluster have a finite size for $T < T_c \approx 0.592746$, that is, it occupies a negligible fraction of the system. Above the critical point the largest cluster is infinite and occupies a finite fraction.

This is the core of percolation theory, initially motivated by a transport problem. From a more generic perspective, Stauffer summarizes it better [65]: "Each site of a lattice is occupied randomly with probability p independent of its neighbors. Percolation theory deals with the clusters of neighboring occupied sites thus formed". At this point it is clear the system goes through a phase transition, each phase defined by the presence or not of a spanning cluster, which promotes a global connectivity of the system. We can study its properties by defining an order parameter P as the fraction of the system occupied by the largest cluster, that is $P = N_\ell/N$ (N being the number of sites in the lattice and N_ℓ the number of sites belonging to the largest cluster). For small values of p, the largest cluster occupies a finite area of the system, which is basically a null fraction for a large enough system. As p approaches a critical probability p_c, the largest cluster grows to the order of

the system size. Figure 10 shows how the order parameter behaves for various sizes of a square lattice. It shows that as the system reaches the thermodynamical limit, the order parameter closely resembles as a second order phase transition.

The type of percolation described so far, where we occupy the sites of a lattice is called *site percolation*. Alternatively we could instead occupy the bonds. It is as if we had an empty isolating substrate with a potential difference V put along it. We then randomly insert resistors between the sites with probability p. The system will have percolated when it has a bridge of resistors traversing it, along which electrical current can flow, thus passing from an isolating phase to a conductive one [66]. Figure 11 illustrate the difference between site and bond percolation.

The exact value of the critical point is non universal and depends on whether it is site or bond percolation and on the lattice choice. The two more notorious examples are site percolation on a square lattice, that has a critical point at $p_c \approx 0.592746$ and site percolation on a triangular lattice at $p_c = 0.5$. Values of the critical point for various other lattices are shown in Table 3.

The critical behavior of the percolation model is usually given by two critical exponents. The first is the *Fisher exponent* τ, related to the distribution of the cluster sizes at criticality

$$n_s \sim s^{-\tau}, \qquad p = p_c, \tag{2.47}$$

where s is the size of a cluster and n_s is the number of clusters with size s in the system. Below the critical point, the distribution has an exponential cutoff

$$n_s \sim s^{-\tau} e^{-cs}, \qquad p < p_c, \tag{2.48}$$

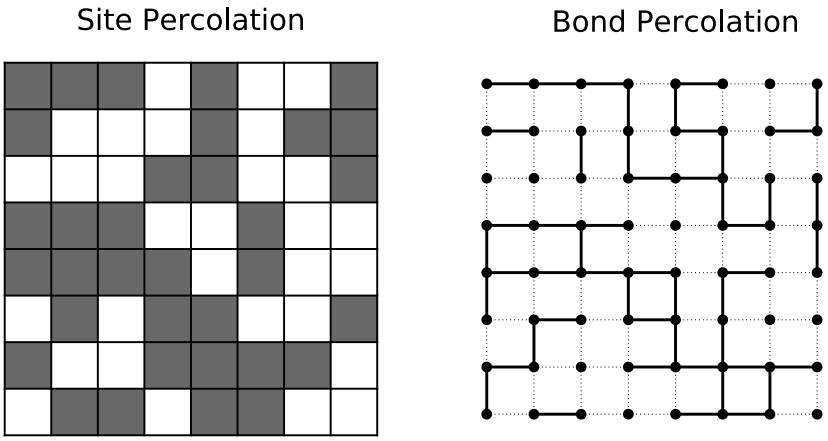

Figure 11 – Examples of site and bond percolation in a square lattice. In site percolation each site is occupied with probability p, while in bond percolation any two neighboring sites are connected with a bond with probability p.

Lattice	Site	Bond
Square	0.592746	0.5
Triangular	0.5	0.5
Honeycomb	0.6962	0.65271
Diamond	0.6962	0.65271
Simple Cubic	0.3116	0.2488
BCC	0.246	0.1803
FCC	0.198	0.119

Table 3 – Percolation threshold for site and bond percolation in several 2D and 3D regular lattices. Reproduced from [65].

where we define the other important critical exponent σ, related to the scaling of the cutoff parameter c

$$c \sim |p - p_c|^{-1/\sigma} . \tag{2.49}$$

From these two exponents, τ and σ, we can determine all others listed in Section 2.2. For instance take the order parameter as defined before. From Section 2.2 we know it scales as

$$P \sim |p - p_c|^{-\beta} . \tag{2.50}$$

We defined P as the expected size of the largest cluster, which we can assume should be distributed like $n_s(p_c) - n_s(p)$ for $p < p_c$. Therefore, using Eqs. 2.47 and 2.48

$$P \sim \int \left[n_s\left(p_c\right) - n_s\left(p\right)\right] s ds \tag{2.51}$$

$$\sim \int s^{1-\tau} \left[1 - e^{-cs}\right] ds \tag{2.52}$$

Integrating by parts and making the transformation $s \to z/c$ yields

$$P \sim c^{\tau-2} \int z^{2-\tau} e^{-z} dz \tag{2.53}$$

$$\propto c^{\tau-2} \tag{2.54}$$

$$\propto |p - p_c|^{(\tau-2)/\sigma} \tag{2.55}$$

which gives us the relation for β as a function of τ and σ

$$\beta = \frac{\tau - 2}{\sigma}. \tag{2.56}$$

In a similar way, we can find γ by using the susceptibility, defined in the percolation context as the second moment of the cluster size distribution

$$\chi = \int s^2 n_s ds \tag{2.57}$$

$$= \int s^{2-\tau} e^{-cs} ds \tag{2.58}$$

$$= c^{\tau-3} \int z^{2-\tau} e^{-z} dz \tag{2.59}$$

Since the integral term in Eq. 2.59 is a constant, we have

$$\chi \propto c^{\tau-3} \tag{2.60}$$

$$\propto |p - p_c|^{-(3-\tau)/\sigma} . \tag{2.61}$$

which leads, following the relation of the γ exponent

$$\gamma = \frac{3-\tau}{\sigma} \tag{2.62}$$

Once β and γ have been determined as a function of τ and σ, all other critical exponents can be derived using the scaling and hyperscaling relations (Eqs. 2.29–2.32, 2.40, and 2.41). Here are all of the others

$$\alpha = 1 - \frac{\tau-1}{\sigma} \tag{2.63}$$

$$\delta = \frac{1}{\tau-2} \tag{2.64}$$

$$\nu = \frac{\tau-1}{\sigma d} \tag{2.65}$$

$$\eta = 2 - d\frac{3-\tau}{\tau-1} \tag{2.66}$$

From a numerical standpoint, percolation does not pose too much problem, as there are many algorithms around that allow for the simulation of very large lattices, basically limited only by the memory of the computer [67].

The critical exponents of two dimensional site percolation lattice have been exactly computed in the triangular lattice using Schramm Loewner Evolutions [53] (we will get there in Chapter 3). The values found are $\tau = 187/91$ and $\sigma = 36/91$. The other exponents can be found in Table 2. Other lattices have not been solved neither proved to be in the same universality class, although the numerical evidence that this is the fact is overwhelming.

Despite the initial motivation coming from transport theory, the percolation model is much more general than that, being applied to various other areas like the study of gelation of polymers [68], conductivity in semiconductors [69], and the dynamics of the immune system [70], among others [71].

Just like the Ising model, the simplicity of percolation is ripe for the development of derivative models, aiming to elucidate other aspects of phase transitions. These include co-operative sequential adsorption [72], explosive percolation [73] and invasive percolation [74], to name just a few.

2.5 Strongly Anisotropic Systems

By now it should be clear that the notion of scale invariance is a central tenet of the modern critical phenomena narrative. There is a class of critical systems that are

explicitly not scale invariant in its strictest sense, they have different properties depending on the direction in which you are looking, that is, they are *anisotropic*. Anisotropy can arise due to the presence competing interactions, stratified structures or simply due to the system being out of equilibrium.

One can easily induce anisotropy in a model by introducing asymmetric interactions, for example you could take the Ising model with different coupling parameters $J_{\parallel}$ and $J_{\perp}$ for different directions. These types of anisotropy however can be removed by the rescaling of one of the axes. Such systems are called weakly anisotropic. On the other hand, there are systems that cannot have their anisotropy removed by rescaling of the axes, in fact rescaling only exacerbates the anisotropy. These are called *strongly anisotropic* systems, and they present a significant, and often overlooked, challenge to those studying critical phenomena. That is because these systems are not scale invariant *per se*, so most of the results shown in Section 2.3 do not translate well into these systems. We can, however, assume that they are invariant under an *anisotropic* scale transformation. This means that the correlation functions transform like

$$C(\mathbf{r}) = C\left(\mathbf{r}_{\parallel}, \mathbf{r}_{\perp}\right) = b^{2x} C\left(b^{\theta}\mathbf{r}_{\parallel}, b\mathbf{r}_{\perp}\right) \tag{2.67}$$

where $\mathbf{r} = \mathbf{r}_{\parallel} + \mathbf{r}_{\perp}$ and the vectors $\mathbf{r}_{\parallel}$ and $\mathbf{r}_{\perp}$ represent preferential directions along which the critical properties of the system are different. The exponent θ is unique for each universality class and called *anisotropic exponent*, it basically quantifies the asymmetry between the directions.

Because the correlation functions are asymmetric, the critical exponents associated with it also have two different values $\eta_{\parallel}$, $\eta_{\perp}$. The correlation length also scales differently in each direction

$$\xi_{\parallel} = |T - T_c|^{-\nu_{\parallel}}, \quad \xi_{\perp} = |T - T_c|^{-\nu_{\perp}} \tag{2.68}$$

The anisotropic exponent relate to them through the relation

$$\theta = \frac{\nu_{\parallel}}{\nu_{\perp}}. \tag{2.69}$$

In dynamical phase transitions, where $\mathbf{r}_{\parallel}$ plays the role of time t, it is common to refer to the anisotropic exponent by the name dynamical exponent z, but all its properties remain the same [27].

Some effort has been put in order to include strongly anisotropic systems into the framework of modern critical systems. For instance, it has been determined that if $\theta = 2/N$, where N is a positive integer, these systems are invariant under local scale transformations [75], which is the same principle that motivated the introduction of conformal invariance (which is in fact the isotropic case $N = 2$). In the particular case of $\theta = 2$ correspond to systems invariant under the Schrödinger group [76]. This observation have been used to successfully study some equilibrium anisotropic systems, like the Liftshitz point in the ANNNI and spherical models [77].

2.5.1 Multi-Layered Percolation

The percolation model as presented in Section 2.4.2 was initially motivated by transport in disordered media, like porous rocks. However, the morphology of earth's crust is highly non-uniform and anisotropic [78], such as the case of stratified rocks formed by the layered deposition of different types of sediment, each with different physical properties such as density and porosity. This layered arrangement have a significant influence in the transport properties of these rocks. Aiming to model the structure of these kind of media, Dayan *et al.* [79] introduced a variant of the percolation model they called multi-layered percolation.

In this model we take a d-dimensional lattice composed of several $(d-1)$-dimensional sub-lattices (or layers) arranged in sequence as if they are stacked one over the other. Following convention, we will call the axis perpendicular to the layers the y-axis. We then perform the usual percolation process by randomly occupying the lattice sites. The key difference here is that each layer has its own occupation probability $p(y)$. For simplicity, it is common to take a two-probability approach, where each layer can have one of two values p_1 and p_2. These are the control parameters of the model, where the line $p_1 = p_2$ represents the regular isotropic percolation. The larger the difference between p_1 and p_2 the more accentuated is the anisotropy of the systems. To make this more evident it is common to redefine the control parameters by taking

$$\bar{p} = \frac{p_1 + p_2}{2}, \qquad \Delta = \frac{p_1 - p_2}{2} \tag{2.70}$$

such that $p_1 = \bar{p} + \Delta$ and $p_2 = \bar{p} - \Delta$. The parameter Δ can take any value in the interval

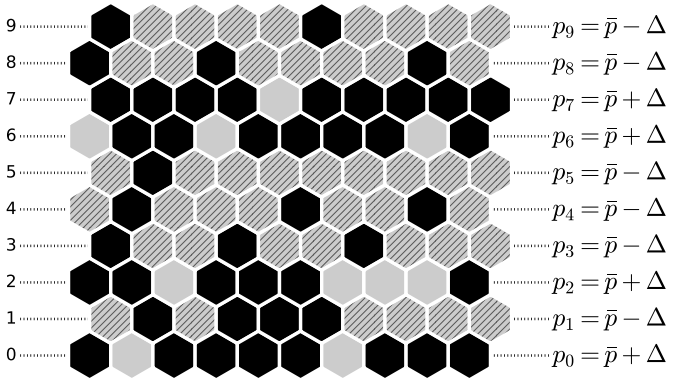

Figure 12 – Schematic representation of the multi-layered percolation model. Each layer (numbered 0 through 9 here) gets one of two probabilities of occupation ($\bar{p} \pm \Delta$), chosen randomly with equal probabilities. Otherwise, the percolation process goes as usual, occupying each site according to the probabilities of each layer.

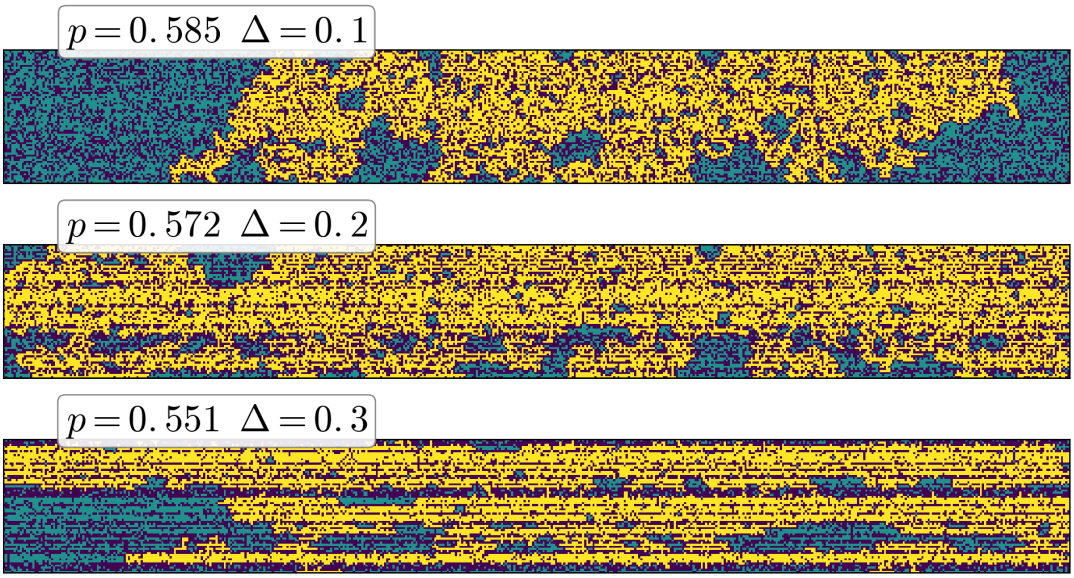

Figure 13 – Three realizations of the multi-layered percolation model in the square lattice. Black sites are unoccupied, dark cyan sites are occupied and yellow sites are represent the largest cluster of the system. All three realizations are in the critical point. The larger the value of Δ, the more anisotropic is the system, and the multi-layered structure of the system becomes more evident.

$[0.0, 0.5]$, and represents the degree of anisotropy of the system, where the system falls back to the isotropic case when $\Delta = 0$. See Figure 12 for an illustration of the multi-layered percolation process. Figure 13 shows three realizations of the model for three different values of Δ. The anisotropy can get very extreme, to the point where it is difficult to visualize the clusters.

Just like isotropic percolation, the multi-layered version also undergoes a second-order phase transition from a non-percolated to a percolated phase. The order parameter remains the same (the relative size of the largest cluster), but now we have two control parameters, p and Δ, so instead of a critical point we have a critical line separating the two phases, as you can see in the phase diagram show in Figure 14. In the case $\Delta = 0$ the value of p_c found is around 0.592 which is the same as isotropic percolation as expected, but it falls continuously to $p_c = 0.5$ as $\Delta \to 0.5$.

Because actually generating clusters of multi-layered percolation can be a complicated matter and the model has no analytical solution, the critical properties were determined numerically through analysis of the cluster perimeters [79, 80, 81]. This is done by generating cluster perimeters in a finite lattice, each defined by sequence of N points at positions $\mathbf{r}_i = X_i\mathbf{x} + Y_i\mathbf{y}$. The root means square of the displacement in each direction

$$F_X(n) = \sqrt{\frac{1}{N-n}\sum_i (X_{i+n-1} - X_i)^2}, \tag{2.71}$$

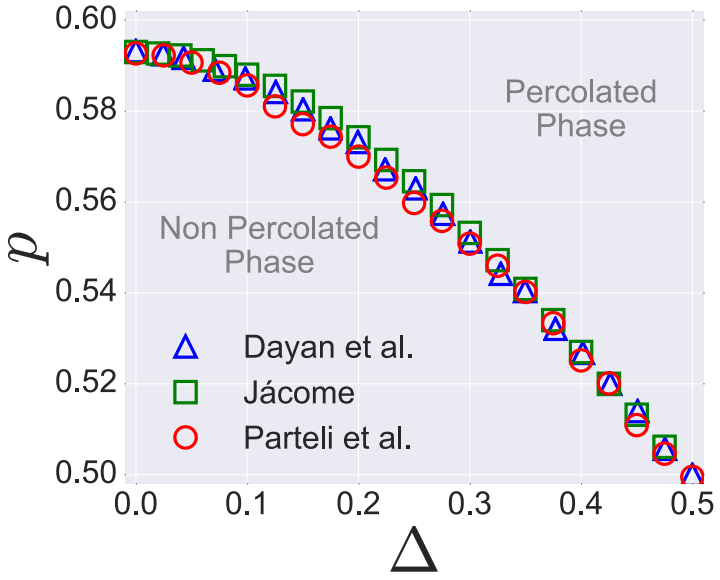

Figure 14 – Phase diagram of the multi-layered percolation model on a square lattice showing the critical line separating the two phases computed in three different occasions by Dayan [79], Jácome [80], and Parteli [81]. We observe that $p_c \approx 0.592$ for for $\Delta = 0$, which is the expected value for isotropic percolation.

(and analogously for Y and F_Y) scale like

$$F_X(n) \sim n^{-\bar{\nu}_x}, \qquad F_Y(n) \sim n^{-\bar{\nu}_y}. \tag{2.72}$$

The exponents $\bar{\nu}_i$ relate to the actual ν_i though the relation

$$\bar{\nu}_i = \nu_i \bar{\sigma} \tag{2.73}$$

where $\bar{\sigma}$ is defined similarly as the σ given in Eq. 2.49, but for perimeter lengths instead of cluster sizes. What was found is that as $n \to \infty$, the $\bar{\nu}_i$ are independent of Δ (as long as it is larger that zero). This means that all the Δ belong to the same universality class with $\bar{\nu}_x = 0.94 \pm 0.01$ and $\bar{\nu}_y = 0.21 \pm 0.01$, and indicates that $\nu_x = 13/6$ and $\nu_y = 1/2$.

2.5.2 Directed Percolation

Another very important universality class of strongly anisotropic systems is yet another variation of the percolation model. Called *directed percolation*, this model can be seen as a spreading process. Starting from some initial condition, any occupied site can spread and occupy an adjacent site along a preferential direction with probability p; spread is prohibited in all other directions. Figure 15 illustrate the process, and Figure 16 shows the process in the three regimes: subcritical, critical and supercritical.

Directed percolation is part of a larger group called dynamical phase transitions, where there is a strict order of cause and effect which allows one to interpret the preferred

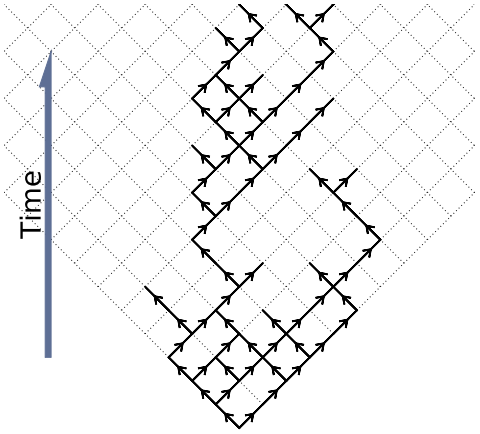

Figure 15 – Simple representation of bond directed percolation in a square lattice. Here, the time flows upwards (although the time direction can be chosen arbitrarily). A previously occupied bond has a probability p of occupying any of its two neighbors along the time direction.

direction as a temporal coordinate. In the case of directed percolation, the configuration of occupied sites in each row is strictly determined by the state of the previous row alone. Because of this, directed percolation is also an absorbing phase transitions, where the system can reach a state from which it cannot leave, as is happens when a row is left completely unoccupied. Systems below the critical point are expected to always reach the absorbing state. This can be seen by looking at the average occupation at time t, namely $\langle N(t)\rangle$, which can be seen in Figure 17. For $p < p_c$ we have that $\lim_{t\to\infty}\langle N(t)\rangle = 0$. At the critical point however, we find the scaling relation

$$\langle N\,(t)\rangle \sim t^{\Theta}, \qquad p = p_c \tag{2.74}$$

with the universal exponent $\Theta \approx 0.302$ [82]. So we can define the order parameter as the probability that the system never reaches the absorbing state. This probability is null for $p \leq p_c$ but grows continuously towards unity, just like a second-order phase transition should.

Unlike isotropic percolation, directed percolation is not an exactly solved model. Its critical exponents can only be determined through numerical methods and field theoretical expansions. In the $(1+1)$-dimensional case the values found were $\nu_{\parallel} = 26/15$ and $\nu_{\perp} = 79/72$ [83] (the rational forms are conjectured, but experimental values are very close with errors in the order of 10^{-4}). Furthermore Owczarek *et al.* [84] analyzed the cluster perimeters in a similar way done with multi-layered percolation, finding consistent values of exponents, including $\bar{\nu}_{\perp} \approx 0.557(5)$ and $\bar{\nu}_{\parallel} \approx 0.879(4)$, which implies $\bar{\sigma} \approx 0.507$.

Experimental realizations of directed percolation are hard to come by as critical exponents are notoriously difficult to measure. A illustrious success was found in turbulent liquid crystal transitions. More recently, experiments and simulations on fluid dynamics

indicate that the transition from laminar to turbulent flow also belongs to the same universality class [85].

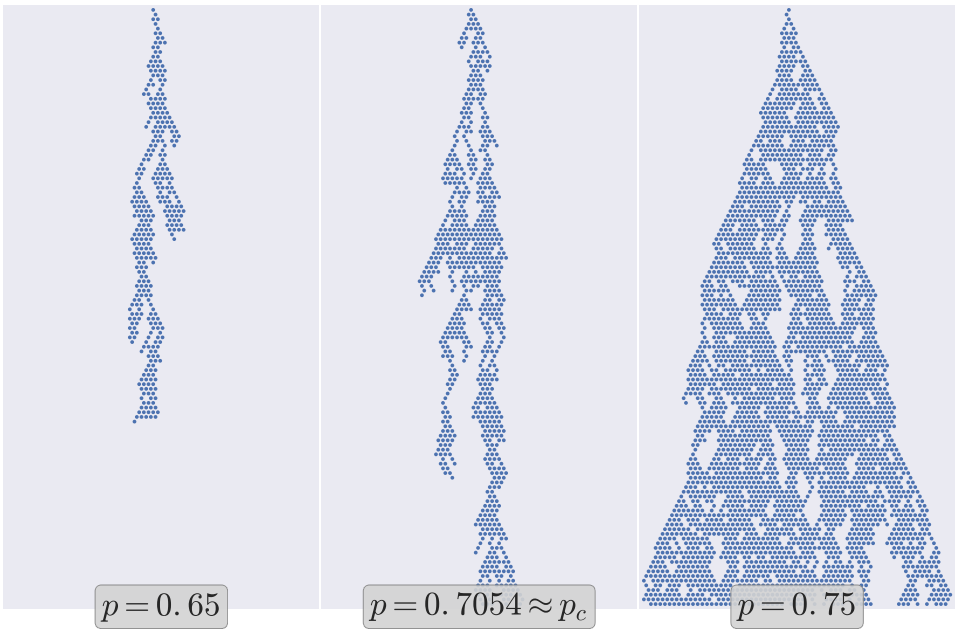

Figure 16 – Three realizations of site directed percolation on a square lattice (here the time flows downwards). Being a absorbing phase transition model, the system have a probability of entering a state that it cannot leave, in this case a fully unoccupied state, like it happens in the left panel. Above the critical point however the probability of reaching an absorbing state becomes vanishing.

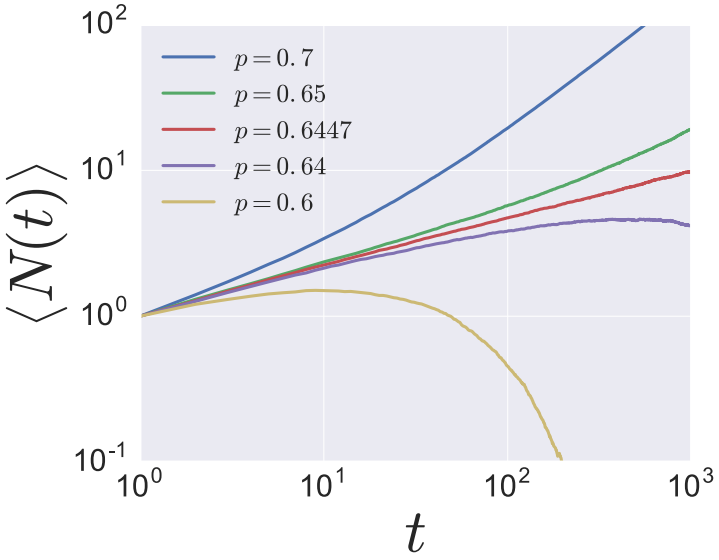

Figure 17 – Expected population of bond directed percolation as a function of time for various values of p. The critical point ($p_c \approx 0.6447$) is the lowest value of p such that $\lim_{t\to\infty} \langle N(t) \rangle > 0$.

2.6 Conformal Invariance

In Section 2.3 we talked about the principle of scale invariance and how incredibly useful it is. It is based on the fact that the correlation functions transform covariantly under a change in scale $\mathbf{r} \to b\mathbf{r}$. A *global* change in scale, that is. One could imagine a transformation $\mathbf{r} \to f(\mathbf{r})$ in which the scaling factor b depends on the position. This would be a *local* change of scale. This kind of transformation would deform the overall shape of the system, but in the direct vicinity of a point it would look like a regular scale transformation with possibly a rotation and translation. Surely we don not expect every possible functional form of f to behave like that, some of them would deform the geometry of the system even at the very small scales, so we must be careful when trying to generalize scale invariance. Luckily there is a class of functions that look like exactly what we want, these are called *conformal transformations* or *conformal maps*.

A transformation $\mathbf{r} \to \mathbf{r}'$ is conformal when it preserve the angle between any two vectors, that is

$$\theta = \arccos \frac{\mathbf{r}_1 \cdot \mathbf{r}_2}{|\mathbf{r}_1|\,|\mathbf{r}_2|} = \arccos \frac{\mathbf{r}'_1 \cdot \mathbf{r}'_2}{|\mathbf{r}'_1|\,|\mathbf{r}'_2|} = \theta', \tag{2.75}$$

as illustrated in Figure 18. More formally, they are coordinate changes that that keep the metric $g_{\mu\nu}$ invariant up to a local scaling factor $\Omega(\mathbf{r})$

$$g'_{\mu\nu}(\mathbf{r}') = \Omega(\mathbf{r})\, g_{\mu\nu}(\mathbf{r})\,. \tag{2.76}$$

Figure 19 shows an example of the same conformal map being applied to a large and a small image, showing how it does not deform the latter, it can only scale, translate or rotate it. Because of that, translational, rotational, and scaling invariance are obvious

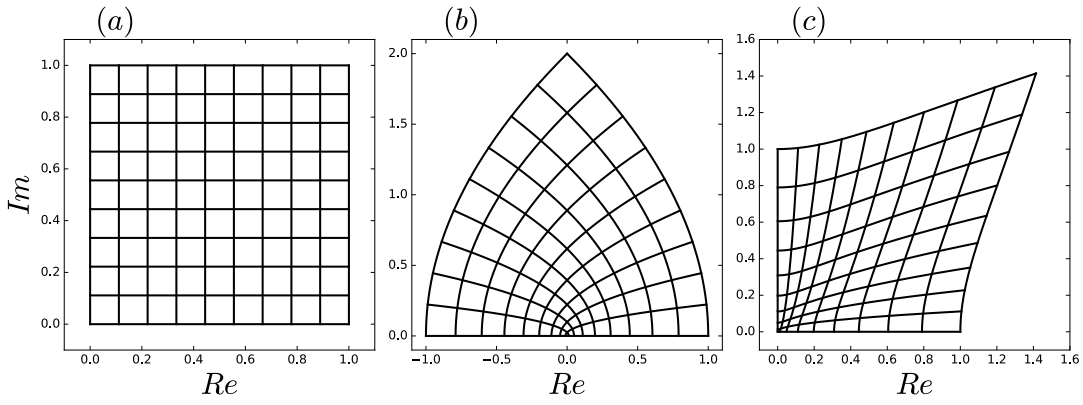

Figure 18 – Coordinates transformations in the complex plane can be divided into conformal and non-conformal. Conformal transformations preserve the intersection angles between lines, unlike the non-conformal. The transformation from the square lattice in (a) into (b) is conformal ($f(z) = z^2$), while the one from (a) to (c) ($f(z) = z|z|$) is not.

properties a system must have in order to be conformally invariant. Another important ingredient is locality, that is, the presence of short range interactions. That is because if different parts of the system will be rescaled by different factors, they must not exert direct influence over one another (they can exert *indirect* influence through long range correlations though). The recipe for conformal invariance is, as Cardy [86] puts it

$$\left.\begin{array}{l}\text{Scale Invariance}\\ \quad + \quad \text{Translation Invariance}\\ \quad + \quad \text{Rotational Invariance}\\ \quad + \quad \text{Short-range Interactions}\end{array}\right\} \Rightarrow \text{Conformal Invariance.}$$

If any of these criteria is not met, conformal invariance breaks down, which is the case of non-local models like minimum spanning trees (given a fully connected graph with randomly weighted edges, the minimum spanning tree is a loopless sub-graph that connects all vertices while minimizing the sum of the weights) [87], or even anisotropic systems as described in Section 2.5.

We can implement the idea of conformal invariance in a similar way we did for scale invariance in Eqs. 2.20 and 2.21. This way, the n-point correlation function of any set of field operators $\{\phi_i\}$ should transform as follows

$$\langle \phi_1(\mathbf{r}_1)\,\phi_2(\mathbf{r}_2)\cdots\phi_N(\mathbf{r}_N)\rangle = \prod_{i=1}^{N} J(\mathbf{r}_i)^{-x_i}\,\langle \phi_1(\mathbf{r}'_1)\,\phi_2(\mathbf{r}'_2)\cdots\phi_N(\mathbf{r}'_N)\rangle\,, \tag{2.77}$$

where in this case J stands for the Jacobian of the transformation $J(\mathbf{r})^d = \det(\partial\mathbf{r}/\partial\mathbf{r}')$, and the x_i are the scaling dimension of each operator. Figure 20 shows how the Ising model in the critical (and conformally invariant) point behave under a conformal transformation. Despite being deformed, the cluster structure remains statistically similar, while above the critical point, which is not conformally invariant, the cluster structure is clearly non uniform after a deformation, as shown in Figure 21.

In $d > 2$ the group of conformal transformations is finite dimensional, and it is composed of only translations, rotations, dilations and the special transformation

$$\mathbf{r} \to \mathbf{r}' = \frac{\mathbf{r} + \mathbf{a}r^2}{1 + 2\mathbf{a}\cdot\mathbf{r} + a^2r^2}. \tag{2.78}$$

These maps are known as projective conformal transformations, and are capable of completely computing 2-point and 3-point correlation functions. Higher order correlators, however, cannot be determined using conformal invariance. Determining these correlators are important in determining the critical exponents through field theoretical series expansions [15].

In $d = 2$, however, the conformal group is infinite dimensional and homeomorphic to the set of all analytical functions. This makes conformal invariance an incredibly powerful

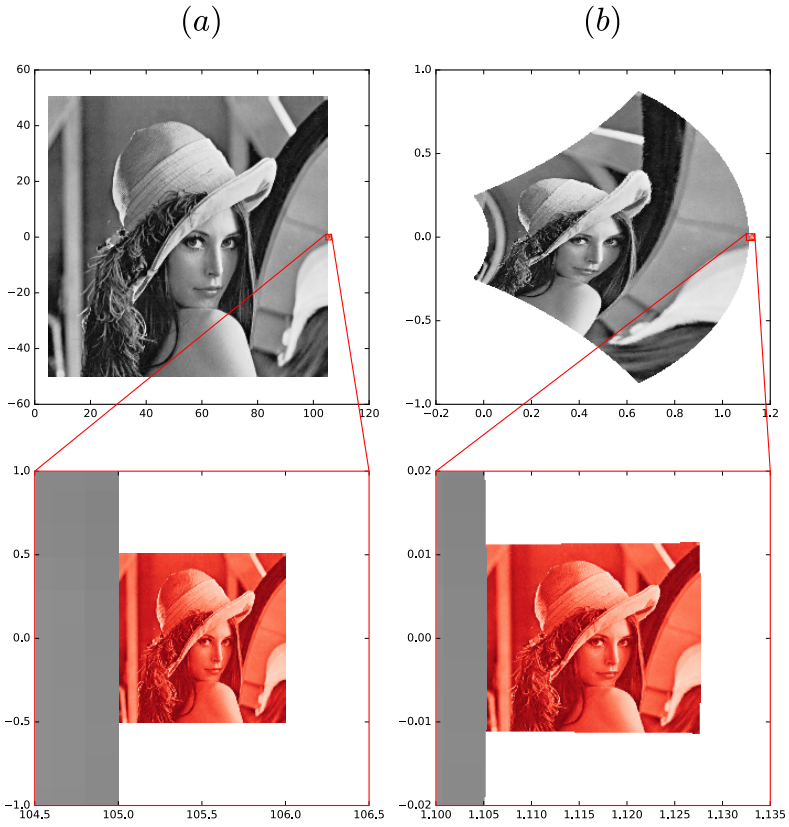

Figure 19 – Two identical images, one large (in grayscale) and the other small (in red, shown in the zoom), are transformed from (a) to (b) using a conformal map $f(z) = z/(200 - z)$. While the large one is heavily deformed, the smaller one was only translated and shrunk. This illustrates the fact that conformal maps behave locally as a scale transformation.

tool to analyze and characterize conformal field theories in two dimensions, since more symmetries implies more constraints over the behavior of the system.

Since the mathematics of analytical functions live and thrive in the complex plane, it is common to shift the analysis to it by making the transformations

$$z = x + iy, \quad \bar{z} = x - iy \tag{2.79}$$

This way, all projective transformations can be condensed into one functional form

$$w(z) = \frac{az + b}{cz + d}, \qquad ad - bc = 1. \tag{2.80}$$

Operators that transform according to Eq. 2.77 when subject to projective transformations are called quasi-primary operators. As mentioned before, the two-point correlation function is fixed and given by

$$\langle \phi_1(z_1)\, \phi_2(z_2) \rangle = \frac{1}{|z_1 - z_2|^{2(h_1+h_2)}}. \tag{2.81}$$

Where $h_{1,2}$ are called the conformal weights. This relation is consistent with Eq. 2.16 and indicates that $\eta = 4h$ when $h_1 = h_2$.

Fields covariant under any conformal map are called primary operators. The magnetization density and energy density fields of the ising model are primary operators, for example. We can derive an important result of critical phenomena by looking at how primary operators transform under the map $f(z) = L\log(z)/2\pi$, which maps the whole plane to an infinite strip of width L. Applying it to Eqs. 2.77 and 2.81 we get a relation between the scaling dimension x of the operator, correlation length ξ and system size L

$$\xi = \frac{L}{2\pi x}. \tag{2.82}$$

Therefore, conformal invariance produced a prediction of the finite-size scaling of the correlation length on a finite system.

A particularly important quasi-primary operator is the stress-energy tensor $T_{\mu\nu}$, related to the "stiffness" of the action when the system is subject to a small deformation $\mathbf{r} \to \mathbf{r} + \epsilon(\mathbf{r})$, which should transform like

$$\delta S = -\frac{1}{2\pi}\int d^2 r \partial^\mu \epsilon T_{\mu\nu}\left(\mathbf{r}\right). \tag{2.83}$$

Although it is a rank-2 tensor, it has ony one degree of freedom, namely $T = (T_{11} - T_{22} - 2iT_{12})/4$, which can be described by the expansion

$$T\left(w\right)T\left(z\right) = \frac{c}{2(w-z)^4} + \frac{2}{(w-z)^2}T\left(z\right) + \frac{1}{w-z}\partial T\left(z\right) + \text{regular} \tag{2.84}$$

If T were a primary operator the first term would no exist. So the constant c called the *central charge*, measures how "non-primary" the stress tensor is. A specific conformal field theory (and as a consequence, the model being studied) is characterized by its central charge. The ising model, for example, has $c = 1/2$ and the 3-state Potts model has $c = 4/5$ [88].

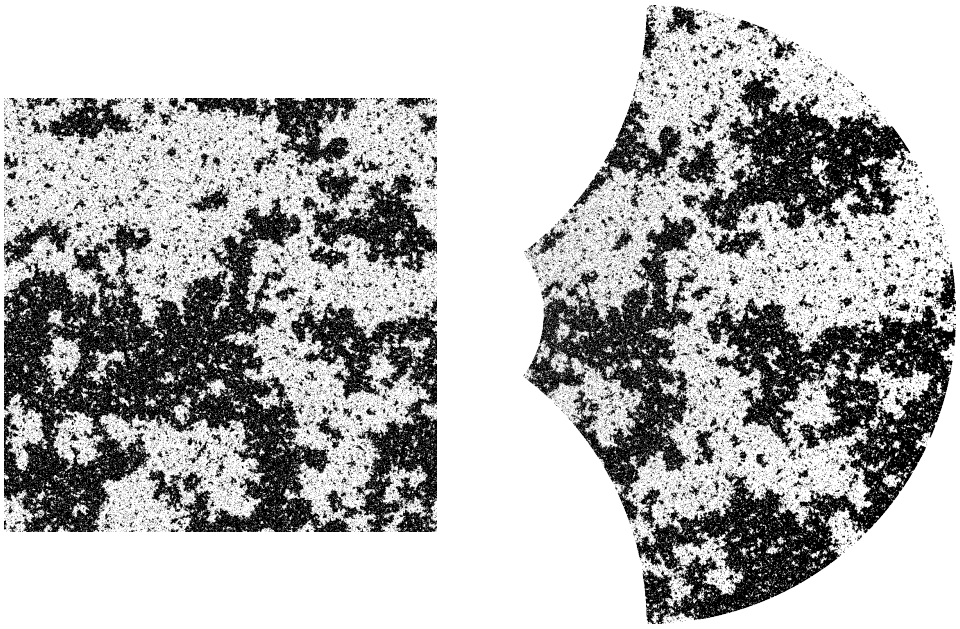

Figure 20 – Illustration of the Ising model at the critical point when transformed under a conformal map $f(z) = z/(2 - z)$. The deformed image still looks statistically similar to the original, which is a consequence of conformal invariance.

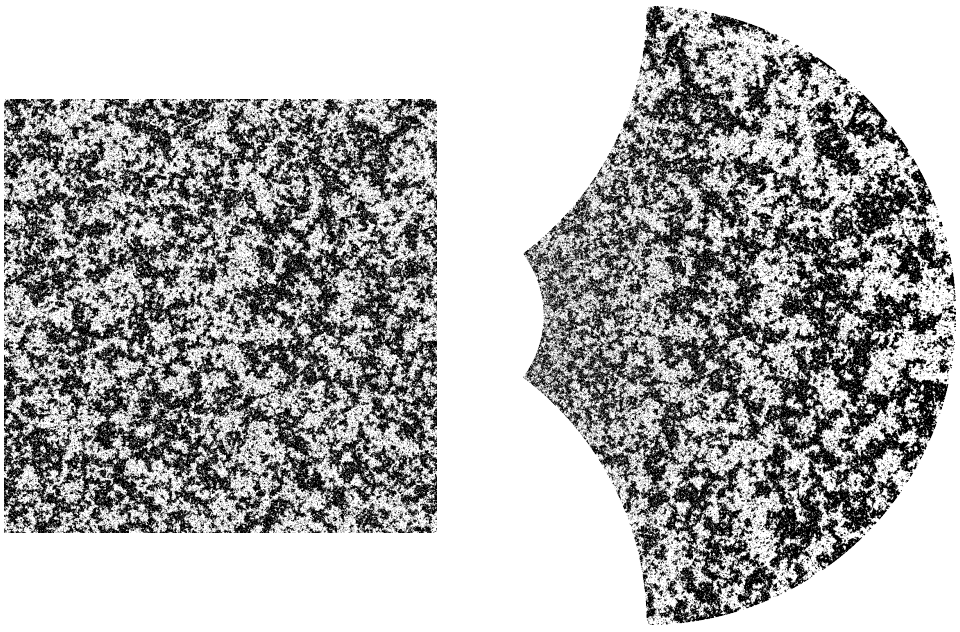

Figure 21 – Illustration of the Ising model above the critical point when transformed under a conformal map $f(z) = z/(2 - z)$. In the deformed image, the spin configuration is no longer homogeneous, because outside the critical point the system is no longer conformally invariant.

3 Schramm-Loewner Evolutions

The most exciting advances in natural sciences happen when two previously unrelated or loosely related fields are brought together to give new insight into old problems. That is what happened when Descartes and Fermat joined algebra (which had just recently reached Europe) and geometry to form analytic geometry [89], an indispensable part of the modern science and engineering mathematical toolbox. Or when Einstein applied the abstract and esoteric non-Euclidian geometry to the physical world with his theory of gravity.

The area of critical phenomena is fortunate enough to see this happen twice. The first was the introduction of conformal invariance and conformal field theory, which were first developed in the 50's by field theorists as a means of creating exactly solvable toy models [90], but in the 80's were very successfully used to compute the critical properties of several two-dimensional systems [91]. Conformal field theory, however, was not free of criticism, specially from mathematicians. Notions like renormalization and field operators are not well defined and often behave, as Cardy puts it, "according to rules that seem to be a matter of cultural convention rather than rigorous logic" [22]. That and the inability of answering some very important questions [21] led mathematicians to search for alternative approaches.

In 2000, a remarkable development happened when Oded Schramm published his theory of Stochastic Loewner Evolutions [24] (SLE). Combining ideas from complex analysis and measure theory, SLE looks not at the fields themselves, but at the random curves that the form the boundary of clusters. This theory was an astounding success, not only rigorously reproducing previously established results, but also answering long standing unsolved problems, like Mandelbrot's conjecture that the boundary of a 2D Brownian motion has fractal dimension of 4/3 [92].

3.1 Loewner Equation

The "Loewner Evolution" part of SLE came much earlier, it was proposed in 1923 by Charles Loewner in the context of the Bieberbach conjecture [23], which concerned some properties of Taylor expansions of analytical function, which was completely proved by de Branges in 1985 [93]. The starting point of the process described by Loewner is the Riemann mapping theorem [94]. This theorem guarantees the existence of a conformal transformation (as defined in Section 2.6) that maps any two regions of the complex plane into one another, as long as these regions are simply connected, that is, they should have no holes in them. The theorem also assures that the boundary of one region gets mapped

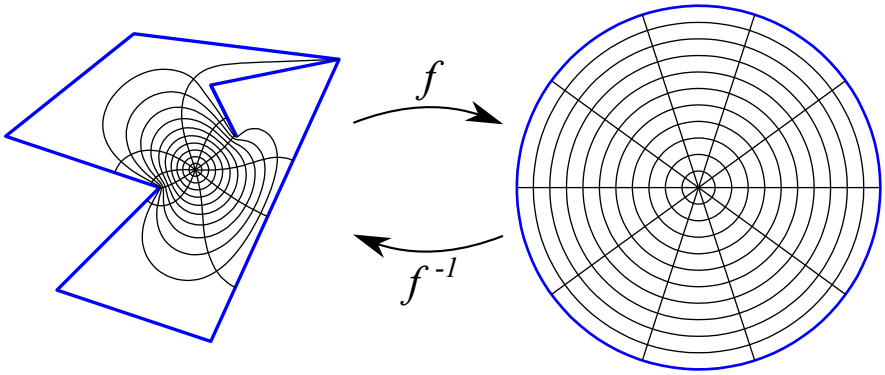

Figure 22 – The Riemann mapping theorem guarantees the existence of at least one conformal mapping f that maps any two simply connected two-dimensional domains. In $2D$ any conformal map is invertible. Generated using th Schwarz-Christoffel toolbox for MATLAB [96].

onto the boundary of the other. In other words, we can transform a region of the complex plane into any shape we want by using a suitable conformal map, as illustrated in Figure 22. Luckily conformal maps are also bijective, so the inverse process is always possible too. In the majority of cases there is no simple form for the map, but they can be constructed at least numerically using Schwarz-Christoffel maps [95]. There is no restriction for the form of the domains involved, they can be as simple or complicated as desired, as long as they do not have any holes in it, and their boundary has more than one point.

To define the Loewner process, we firstly take any simply connected domain D which will serve as a standard domain. Now we imagine making a crack in this domain, like shown in Figure 23. This crack has no width, so it can be described as a curve γ which starts at some point r_1 at the boundary ∂D and ends at a point r_2 which may be an interior or boundary point. As long as γ does not touch itself, the cracked domain $D \setminus \gamma$[1] is also simply connected. Because of that, the Riemann mapping theorem assure us that we can "fix" this crack by finding the conformal transformation g that maps the cracked domain into the uncracked standard domain, or in math lingo $g : D \setminus \gamma \to D$. This is called a *uniformizing map*, and the crack γ goes by the more formal name *trace*. We distinguish two types of traces. If r_2 is an interior point of D, the trace is said to be *radial*, and if it belongs to the boundary ∂D it is called *chordal*.

Let us parametrize the trace using a positive real parameter t such that $\gamma_0 = r_1$ and $\gamma_\infty = r_2$. For now we will leave the parametrization choice free. We denote $\gamma_{[0,t]}$ the whole extent of the trace from γ_0 up to the tip γ_t. Therefore, for every value of t we have a different uniformizing map $g_t : D \setminus \gamma_{[0,t]} \to D$. We can imagine t as a sort of time, and the evolution of the tip γ_t as a growth process. An immediate question one might ask is, what

[1] $\cdot \setminus \cdot$ being the set-minus operator.

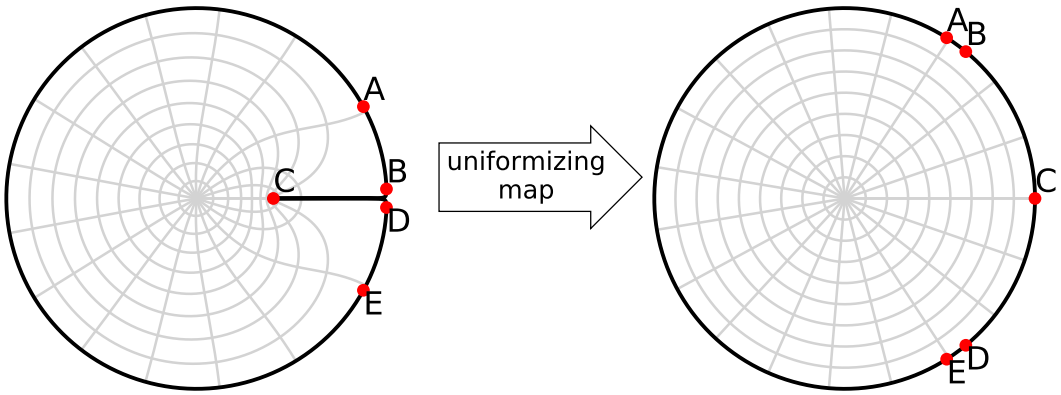

Figure 23 – Using a suitable conformal transformation it is possible to remove a slit in the domain, mapping it to the circular boundary. Points close to each other in the slitted domain (B and D) get mapped far apart in the one without the slit.

is the relation between D, γ and the g_t? Are they uniquely defined? Is there a kind of equation that relates these objects? Loewner's answer is "yes", as long as you are willing to make a few compromises.

We can construct an equation for g_t by shifting our attention from the trace itself. You see, since the tip of the trace γ_t is part of the boundary of $D \setminus \gamma_{[0,t]}$, it will necessarily get mapped to a point $U_t = g_t(\gamma_t)$ in the border of the standard domain D. If we follow the time evolution of this point, we get a function $U_t : \mathbb{R}^+ \to \partial D$. This is called the *driving function* of the trace in question. An schematic representation of the whole process in shown Figure 24. In his work, Loewner showed that the trace, the uniformizing on map, and the driving function are connected by a differential equation.

Before we can write down this equation we need to make a series of assumptions. One of them is to decide if we want to deal with radial or chordal traces. Other is to determine the standard domain in which the trace will grow. In his original work, Loewner chose the unit disc $\mathbb{D} = \{z||z| \leq 1\}$, with $\gamma_0 = 1$ and $\gamma_\infty = 0$ for the radial case. For the chordal case, the most commonly used domain is the upper half plane $\mathbb{H} = \{z|\text{Im}\{z\} \geq 0\}$ with $\gamma_0 = 0$ and $\gamma_\infty = \infty$, which offers the practicality that $\partial\mathbb{H} = \mathbb{R}$, so the driving function is real valued. In physical applications, it is much more common to use the chordal version, and it is the version we will focus here. Figure 25 show two examples of radial and chordal traces in these domains.

In order to determine the chordal Loewner equation we need first to impose some conditions on the conformal map g_t, otherwise there are an infinity of maps that connect $\mathbb{H}\setminus\gamma_{[0,t]}$ to $\mathbb{H}$. To induce uniqueness, we impose what is called a *hydrodynamic normalization*.

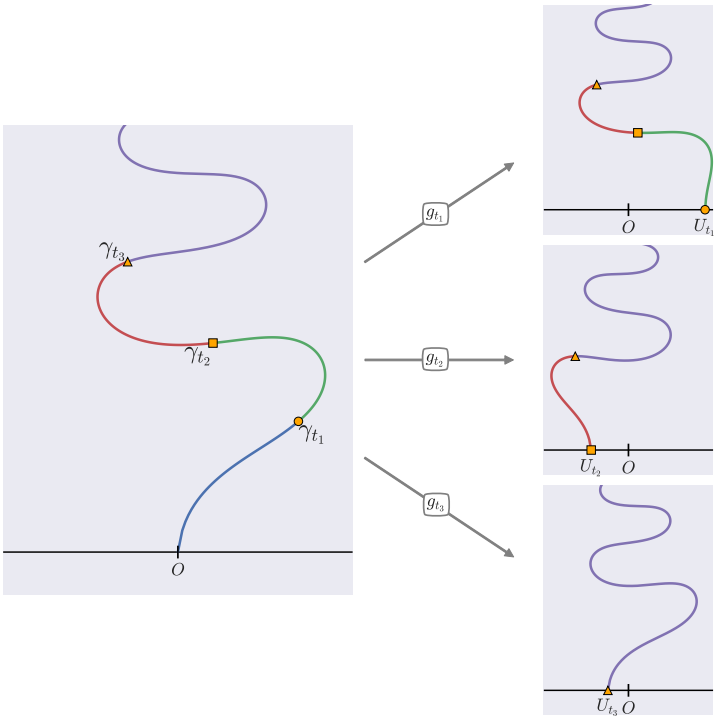

Figure 24 – How the chordal Loewner evolution works. We define the trace γ parametrized by a time t. At each time instant there is a conformal map g_t that maps the upper half plane minus the trace up to time t to the upper half plane itself, that is, $g_t : \mathbb{H} \setminus \gamma_{[0,t]} \to \mathbb{H}$. The tip of the trace always get mapped to the real line. If we track the point where the tip is mapped, we get a function U_t called driving function, that is $U_t = g_t(\gamma_t)$. The trace, driving function and uniformizing maps are all related through Loewner's equation (Eq. 3.2).

This means that far from the origin, the uniformizing maps behave as

$$g_t(z) \approx z + \frac{a(t)}{z} + O\left(z^{-2}\right), \qquad z \to \infty. \tag{3.1}$$

This way, points at infinity get mapped into themselves. The coefficient $a(t)$ is called the half plane capacity, and can take any form as long as it obeys a number of properties, including positivity, monotonicity and continuity [97]. The choice of capacity is intrinsically connected with the parametrization of the trace (the SLE time t) and it is far from a trivial point, which has drawn some attention from mathematicians [98]. Here, we will go with the most common choice of $a(t) = 2t$.

With all these properties laid out, the chordal Loewner equation takes the (deceptively) simple form

$$\partial_t g_t(z) = \frac{2}{g_t(z) - U_t}, \qquad g_0(z) = z, \tag{3.2}$$

where $U_t \in \mathbb{R}$ and the trace can be obtained by taking the limit

$$\gamma_t = \lim_{z \to 0} g_t^{-1}(U_t + z), \tag{3.3}$$

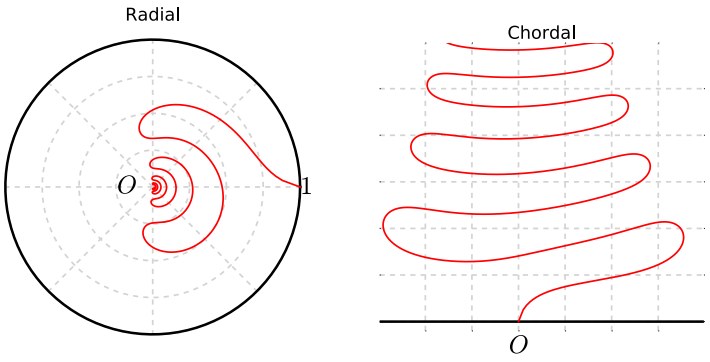

Figure 25 – Radial versus chordal Loewner traces generated using the same driving function $U_t = 2\sin(2\pi t)$ (in the radial case you have to use $\exp(iU_t)$). Radial curves are contained inside the unit circle $\mathbb{D} = \{z||z| \leq 1\}$ and start at $z = 1$ growing towards the origin. Chordal traces are contained in the upper half plane $\mathbb{H} = \{z|\text{Im}\{z\} \geq 0\}$ starting at the origin and growing towards infinity.

since the Loewner equation is not well defined for $g_t(z) = U_t$. The derivation of Loewner's equation is outlined in Appendix A and a example of a chordal trace obtained from it in Figure 26. Furthermore, working only on the upper half plane seems restrictive, but remember that any two domains can be mapped into one another through conformal transformations. So to get the trace in a domain D that connects two points $r_1, r_2 \in \partial D$, all you have to do is to find the function $f : \mathbb{H} \to D$, where $f(0) = r_1$ and $f(\infty) = r_2$. Under similar assumptions, the radial Loewner equation in the unit disc is

$$\partial_t g_t(z) = g_t(z)\frac{e^{iU_t} + g_t(z)}{e^{iU_t} - g_t(z)}, \qquad g_0(z) = z. \tag{3.4}$$

with $U_t \in \mathbb{R}$. Figure 25 shows the trace obtained in both cases for a simple driving function.

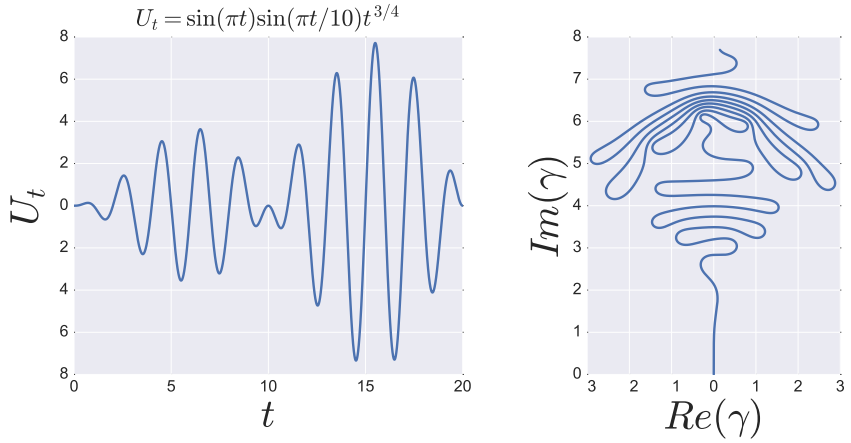

Figure 26 – Example of a Loewner trace generated by the driving function $U_t = \sin(\pi t)\sin(\frac{\pi t}{10})t^{3/4}$. The trace γ is defined by the relation $\gamma_t = g_t^{-1}(U_t)$, where g_t is the solution of the Loewner differential equation (Eq. 3.2).

Not surprisingly, the topological and geometric properties of the trace γ_t are intimately connected with the analytical properties of the driving function U_t. Some properties include [99]:

1. if U_t is smooth, with a derivative well defined, then γ_t never intersects itself;
2. if U_t is periodic, γ_t is self-similar;
3. if U_t is Hölder continuous with exponent $1/2$ with constant larger than 4, meaning that there is a finite constant C such that

$$4 < \lim_{s \to 0^+} \left| \frac{U_{t-s} - U_t}{s^{1/2}} \right| < C, \tag{3.5}$$

then the trace does touch itself.

This last one might require some clarification. We established that the Riemann mapping theorem is valid only for simply connected domains. If the trace touches itself at an instant τ, then $D \setminus \gamma_{[0,t\geq\tau]}$ is not simply connected, and the existence of g_t cannot be guaranteed. This confusion comes from an innocent omission made at the beginning of this section (made to keep things simple). The uniformizing map that satisfy the Loewner equation does not in fact map $D \setminus \gamma_{[0,t]}$ to D. It actually maps $D \setminus K_t$ to D, where the *hull* K_t is the set comprising the trace $\gamma_{[0,t]}$ *and* all the space trapped inside the loops formed when the trace touches itself. One can easily see that K_t is always simply connected and if the trace is simple $K_t = \gamma_{[0,t]}$.

The overall behavior of the trace follows that of the driving function, so a very complicated U_t tend to generate very intricate traces. One could imagine a driving function

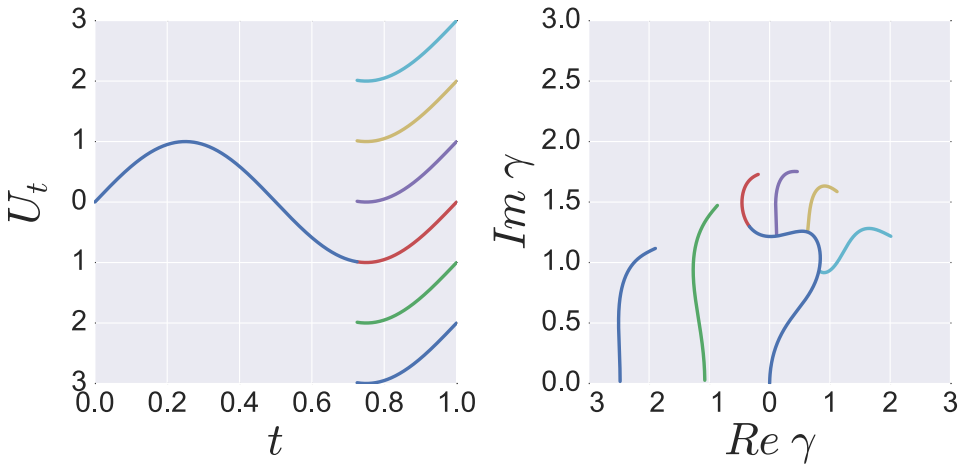

Figure 27 – The Loewner trace driven by discontinuous functions with several sizes of discontinuity. The resulting trace is also discontinuous taking a tree-like structure, where new branches can start at real line or at the older branches depending on the size of the discontinuity.

that has a discontinuous jump, for example. In this case, the trace will have also display a break, starting a new branch coming out of the real line or from the old segment depending on the size of the discontinuity, giving the trace a tree-like aspect, like shown in Figure 27.

3.2 Stochastic Loewner Evolutions

A big breakthrough in the area of critical phenomena happened when Oded Schramm used Loewner evolutions to study the interfaces that form in critical systems, like the perimeter of a percolation cluster. He did that by showing that all properties of conformally invariant models are codified in a family of Loewner evolutions driven by a fairly simple driving function. In this section we will give an outline of this theory, but there is an abundance of material for the reader interested in digging deeper [22, 97, 100].

If we want to describe conformally invariant critical systems using Loewner processes, we need to redefine the concept conformal invariance. The definition given in terms of the covariance of field operators (Eq. 2.77) does not translate well into the framework of Loewner evolutions because there is no way to incorporate the notion of field. Instead we need to define it in terms of the curves that form the boundaries of clusters, which are meant to be the traces. To do that we take a measure theory approach (the more general mathematical theory of probability) [101]. In this context, we define conformal invariance as follows: let f be a conformal map between two domains D and D' such that $D' = f(D)$, then the measure $\mu_D(z, w)$ over the set of traces that connect two points $z, w \in \partial D$ should behave like [22]

$$f \circ \mu_D (z, w) = \mu_{f(D)} (f(z), f(w)) . \tag{3.6}$$

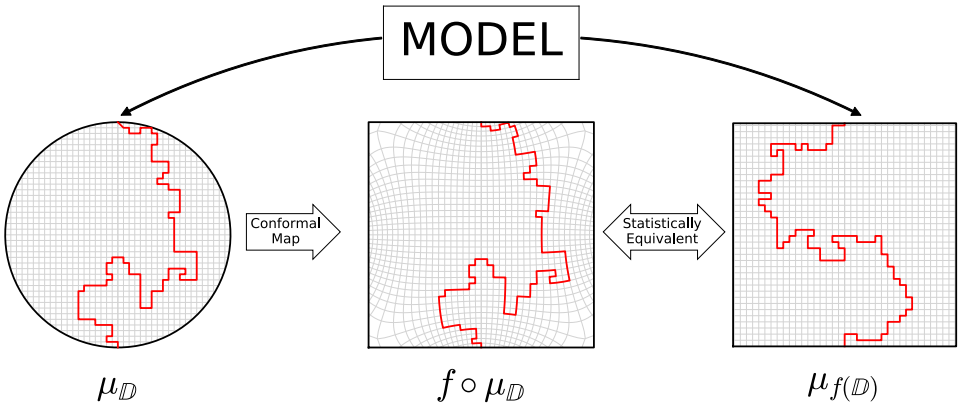

Figure 28 – In the context of SLE, conformal invariance is defined in terms of the distribution of traces. For example, let f be a conformal map from the unit disk $\mathbb{D}$ to a square domain $f(\mathbb{D})$, then the distribution $f \circ \mu_{\mathbb{D}}$ of the traces generated in $\mathbb{D}$ and mapped to $f(\mathbb{D})$ should be the same as the distribution $\mu_{f(\mathbb{D})}$ of the traces generated directly in the square domain, in the continuum limit.

That is to say, suppose you want to generate a curve in a, say, triangular region. You can do this in two ways, one by simply applying you lattice model to the triangular domain, or you can apply the lattice model in a square domain and then conformally map the resulting trace to a triangular domain. Conformal invariance states that, in the *continuum limit*, these two processes are statistically identical, as illustrated in Figure 28. Here we used the term *measure* instead of probability distribution, because the latter cannot be actually be defined for traces in the continuum limit, but the more general concept of measure can be applied.

Conformal invariance, however, is not enough to pinpoint a general driving function for critical systems. In his work, Schramm identified another fundamental property that lattice models must have in the continuum limit, and indeed tend to obey. It is called *domain Markov property*, and refers to the measure of a trace segment γ_2 conditioned by a fixed initial segment γ_1,

$$\mu_D\left(\gamma_2|\gamma_1\right) = \mu_{D\setminus\gamma_1}\left(\gamma_2\right). \tag{3.7}$$

It means that the conditional measure of family of curves γ_2 that have the same start γ_1 in a domain D is the same as that of γ_2 in the same domain with γ_1 removed, that is, $D \setminus \gamma_1$. In the same line of conformal invariance, domain Markov property can be understood in the following way: if you use a model to generate a set of curves in D that all have the same start γ_1, the curves γ_2 obtained would have the exact same properties as if you generated the curves by applying the model to $D \setminus \gamma_1$. And just like conformal invariance, this is only expected to hold in the continuum limit. A visual explanation can be seen in Figure 29.

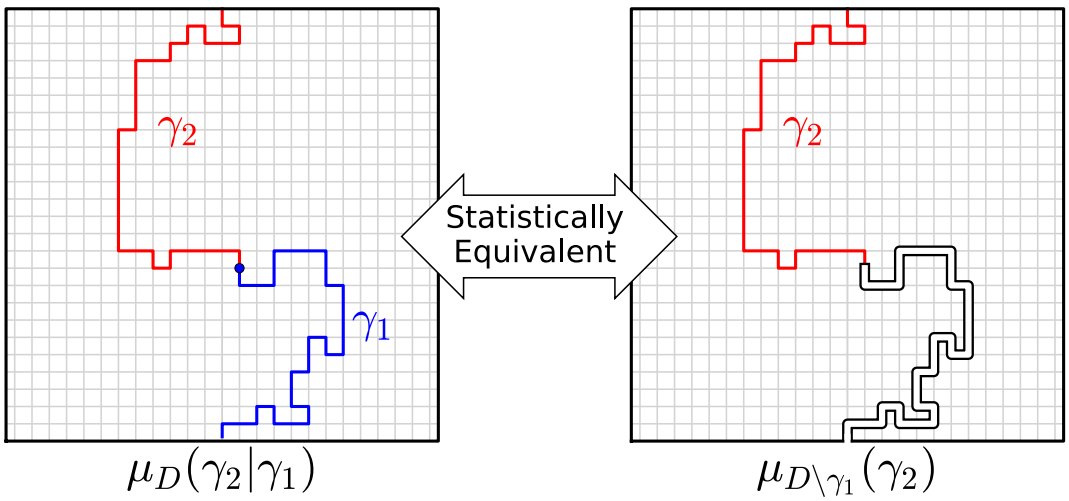

Figure 29 – The domain Markov property states that the conditional distribution of γ_2 given a fixed γ_1 in a domain D, $\mu_D(\gamma_2|\gamma_1)$, is the same of γ_2 in the same domain with γ_1 removed, that is, $\mu_{D\setminus\gamma_1}(\gamma_2)$.

The interfaces present in critical systems are usually random curves, so it is only safe to assume that their driving functions should also be stochastic processes. The climax is Schramm's work was the proof that systems that obey conformal invariance and domain Markov property, as defined above, can only have as a driving function

$$U_t = \sqrt{\kappa} B_t, \tag{3.8}$$

where B_t is a Brownian motion, also known as Wiener process. It is defined as having the following properties [102]:

- $B_0 = 0$;
- The increments $B_t - B_s$ with any $t > s$ are always independent from one another;
- The increments $B_t - B_s$ with any $t > s$ are distributed according to a normal distribution with zero mean and variance $\sigma^2 = t - s$;
- B_t is almost surely continuous.

This is a striking result. Using only a family of driving functions with a single parameter, κ, which plays the role of the diffusion coefficient of the Brownian motion. With it, we are able to describe all properties of many criticality models. In the inaugural paper of SLE, Schramm showed that loop-erased random walks (random walks with the loops removed in chronological order) and uniform spanning trees converge to SLE with $\kappa = 2$ and $\kappa = 8$ respectively. Figure 30 shows a realization of SLE with $\kappa = 2$.

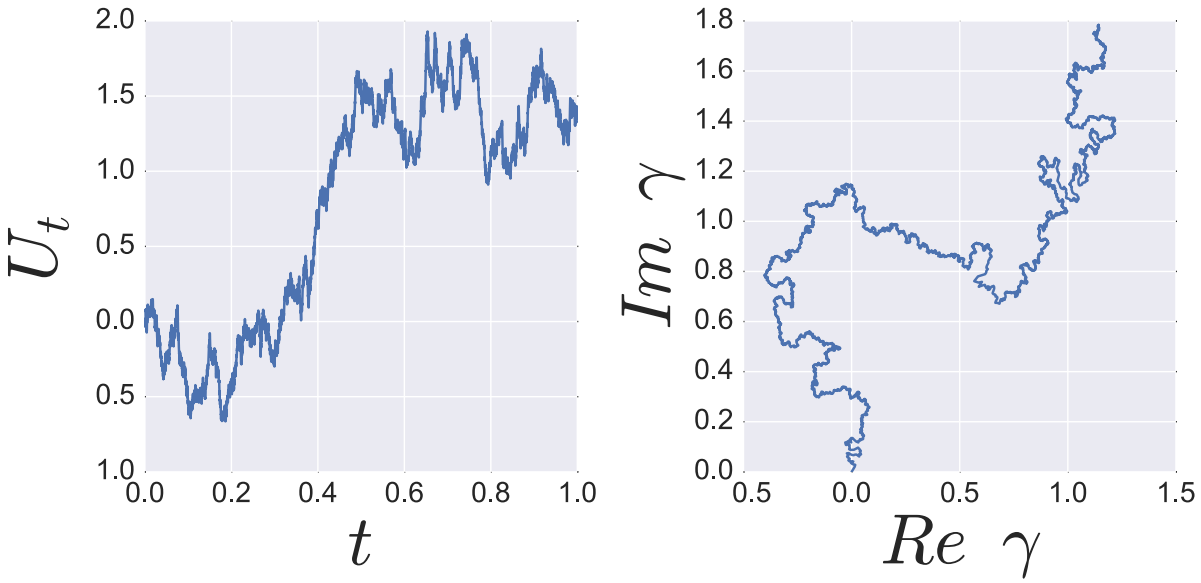

Figure 30 – Example of a Schramm-Loewner evolution, which is a Loewner evolution driven by a Browninan motion, in this case with diffusion coefficient $\kappa = 2$.

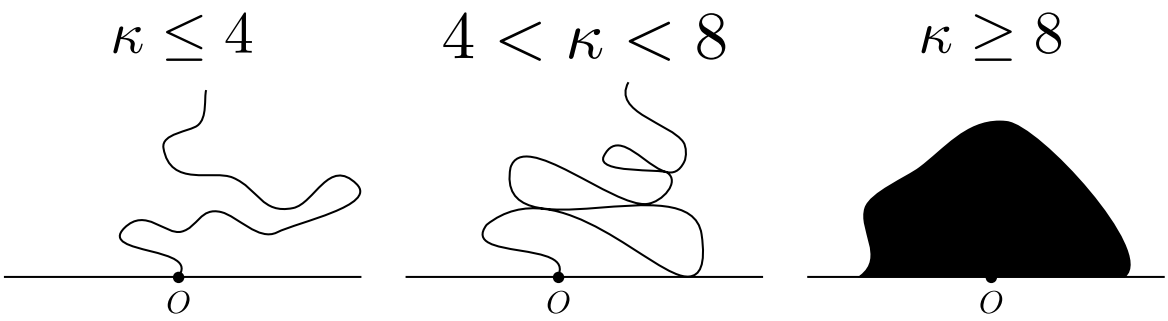

Figure 31 – The SLE trace display three different behaviors depending on the value of κ. For $\kappa \leq 4$ the trace is simple, so it does not touch itself. For $4 < \kappa < 8$ the trace touches itself. And for $\kappa \geq 8$ the trace is space filling.

Mathematicians and physicists were quickly drawn to this new theory, unveiling various interesting properties. One that stands out is how the trace looks with different values of κ [103]. You see, the Brownian motion is basically a function that varies randomly with time. This random variation gives the wiggly aspect of the trace, as seen in Figure 30. This means that the higher the value of κ, the larger will be the variations of the Brownian motion, and the more wiggly the trace will be. When the value of κ is less or equal than 4 the trace will not wiggle so wildly to the point of touching itself. So in this case the trace is a simple curve, as we already suggested in the last section with Eq. 3.5. When $\kappa > 4$, however, the trace almost surely touch itself in all length scales, to the point that the hull (the trace plus the regions inside the loops it forms) eventually swallows the whole upper half plane. If $\kappa \geq 8$ not only the trace touches itself, but it does so on *every* point of the domain, so there is no point in $\mathbb{H}$ that does not eventually belong to the trace, we say the curve is space filling. The general aspect of the tree phases can be seen in Figure 31.

The behavior of the trace in each of the three distinct phases is closely related to its fractal dimension. The fractal dimension d_f of a curve if usually defined by counting the number N of circles of radius ϵ needed to cover the whole curve. This should behave as [104]

$$N \sim \epsilon^{-d_f}. \tag{3.9}$$

The relationship between κ and the fractal dimension was determined by Beffara [105] and given by

$$d_f = \min\left(1 + \frac{\kappa}{8}, 2\right). \tag{3.10}$$

We see that for $\kappa \geq 8$ implies that $d_f = 2$, which is exactly what we would expect from a space filling curve. You can see several realizations of SLE for different values of κ and how the trace and its fractal dimension behave in Figure 32.

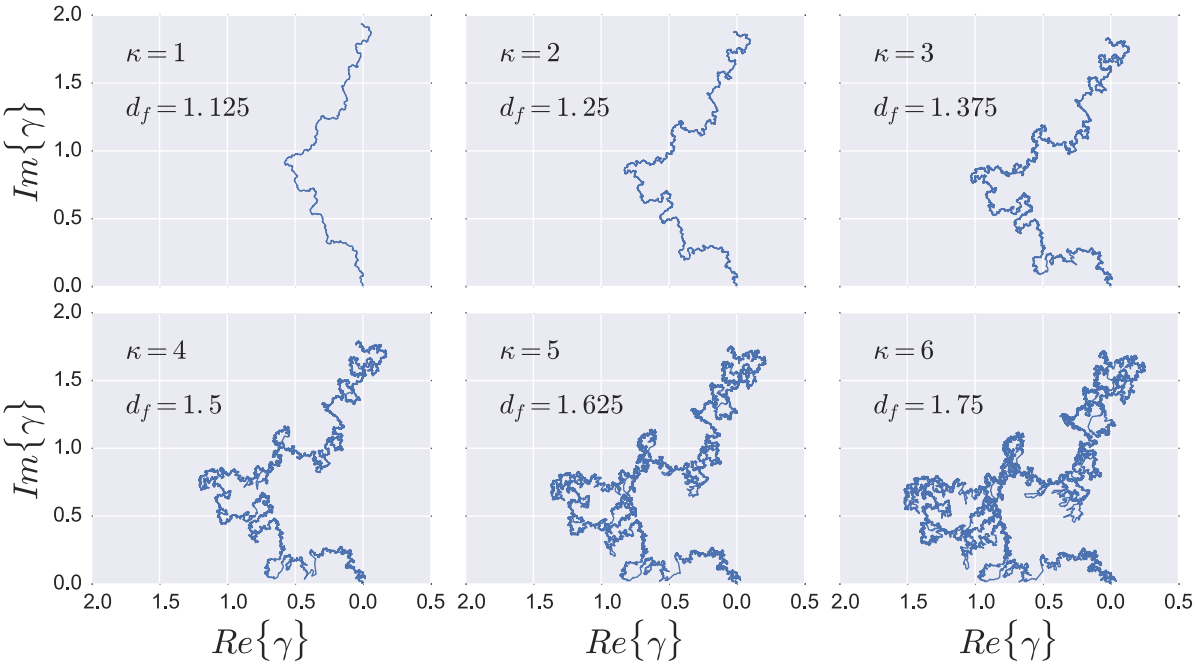

Figure 32 – Examples of several SLE traces generated using the same underlying Brownian motion, but with different κ. The fractal dimension is given by $d_f = \min(1 + \kappa/8, 2)$.

Some other properties are useful to know if one is trying to determine if a model can be represented by a SLE, specially if the investigation is numerical. The probability that a point $z = |z|e^{i\theta}$ is to the left of the trace, for instance, depends only on θ and is given by

$$P = \frac{1}{2} + \frac{\Gamma\left(4/\kappa\right)}{\sqrt{\pi}\Gamma\left(\left(8-\kappa\right)/\left(2\kappa\right)\right)} \cot\left(\theta\right) {}_2F_1\left(\frac{1}{2}, \frac{4}{\kappa}, \frac{3}{2}; -\cot^2\theta\right), \tag{3.11}$$

where ${}_2F_1$ is the Gaussian hypergeometric function. A good evidence that a model can be described by SLE is to generate various traces and estimate the value of κ using equation 3.11. This value should be consistent with the coefficient of diffusion of the computed driving function (see Section 3.4 for how to compute the drive of a trace), which should behave as

$$\left\langle U_t^2 \right\rangle = \kappa t. \tag{3.12}$$

The point of contact between statistical physics and SLE happen at the central charge of a conformal field theory. Bauer and Bernard [106] showed that κ and c are connected by the relation

$$c = \frac{\left(3\kappa - 8\right)\left(6 - \kappa\right)}{2\kappa}. \tag{3.13}$$

One might notice that each central charge value corresponds to two values of κ, namely κ and $16/\kappa$. This is connected the notion of duality of SLE, first suggested by Duplantier [107] who noticed that if we remove the loops of an SLE trace with $\kappa > 4$ we would be left

with yet another SLE trace (at least locally) this time with $\tilde{\kappa} = 16/\kappa$. This was eventually proved for that case $\kappa = 6$ [108], which has a dual $\tilde{\kappa} = 8/3$, suspected to be the same as the self-avoiding walk.

Since Schramm's first publication, various lattice models have been shown to converge to SLE, which is a testament to the success of the theory. Some of the values of κ identified include

- $\kappa = 2$: loop-erased random walk [24];
- $\kappa = 8/3$: suspected to be self-avoiding walk [109], proved to be the border of a 2D random walk [92];
- $\kappa = 3$: cluster boundaries of the Ising model [110];
- $\kappa = 4$: harmonic explorer [111];
- $\kappa = 6$: boundaries of percolation clusters [112];
- $\kappa = 8$: uniform spanning trees [24].

Furthermore, there's several models that have been conjectured to be conformally invariant and have their own value of of κ estimated numerically. These include 2D and 3D turbulence [113, 114], shortest path of percolation clusters [115] and watersheds [116].

3.3 Lévy Processes, Anomalous Diffusion, and SLE

As mentioned so far, SLE is a theory concerned with conformally invariant families of curves, which are always driven by a Brownian motion. In cases where the driving function is a more general stochastic process, the curves themselves are not required to be conformally invariant, even though the Loewner equation describes the time evolution of a conformal map [100]. This opens space for the study of stochastic Loewner evolutions driven by processes that deviate from the Brownian motion. This is the case of the work of Rushkin *et al.* [117, 118], who studied SLE driven by Lévy processes, L_t, which behave pretty much like the Brownian motion described in Section 3.2, except the increments are distributed according to a power law in the limit of large x

$$P(L_{t+dt} - L_t \in [x, x+dx]) \propto \frac{1}{|x|^{1+\mu}} dx dt, \qquad 0 < \mu < 2. \tag{3.14}$$

In general, stochastic processes can be classified according to the behavior of the mean square displacement, which usually goes like

$$\left\langle U_t^2 \right\rangle \propto t^{\alpha}. \tag{3.15}$$

For the Brownian motion, $\alpha = 1$, which is referred as regular diffusion. Lévy processes are called superdiffusive because $\alpha = 2/\mu > 1$. Some processes can also present the case $\alpha < 1$, called subdiffusive. The exact effect of the value of the diffusion exponent α on the properties of the trace is yet unknown, but it was noted that the traces (which are not continuous, for L_t is also not continuous), present an anisotropic scaling with time. This means the typical width and height of the hull, $X(t)$ and $Y(t)$ respectively, scale with different exponents following the relations

$$X(t) \sim t^{1/\mu}, \quad 0 < \mu < 2 \tag{3.16}$$

$$Y(t) \sim \begin{cases} A + Bt^{1-1/\mu}, & \mu \neq 1 \\ \log(t), & \mu = 1. \end{cases} \tag{3.17}$$

3.4 Numerical Methods

The crux of the Schramm Loewner Evolution problem (at least from a physicist's standpoint) is determining whether or not a given model converges to it in the continuum limit, and what is the value of κ for each specific model. We mentioned several models that have show such convergence, the most illustrious being Smirnov's demonstration that percolation in a triangular lattice is an SLE with $\kappa = 6$ [112]. Nonetheless, just like nobody would expect every critical system to have an exact solution similar to the Ising model, one may not expect to be able to prove the SLE convergence for every conceivable model. This is where numerical analysis comes into the scene. By comparing the statistical behavior of the model with the expected SLE trace, we can infer if the hypothesis holds true.

In this section we will present some algorithms for computing Loewner evolutions out of any given driving function, as well as the opposite task, computing the driving function from any given trace.

3.4.1 Euler's Method

Euler's method for solving ordinary differential equations is arguably the simplest [119]. It is used to solve equation of the type $y'(t) = f(y,t)$ and it basically consists in taking a first order approximation of the solution

$$y(t) = y(t_0) + \int_{t_0}^{t} f(y(\tau), \tau)\, d\tau \approx y(t_0) + (t - t_0) f(y(t_0), t_0), \tag{3.18}$$

as long as $t - t_0$ is small enough. This way, the equation can be solved recursively by providing a discretized driving function U_{t_i} with $t_0 = 0 < t_1 < \cdots < t_N$ and. Applying it to Loewner's equation (Eq. 3.2) we have, with initial condition $g_0(z) = z$,

$$g_{t_{i+1}}(z) = g_{t_i}(z) + (t_{i+1} - t_i)\frac{2}{g_{t_i}(z) - U_{t_i}}. \tag{3.19}$$

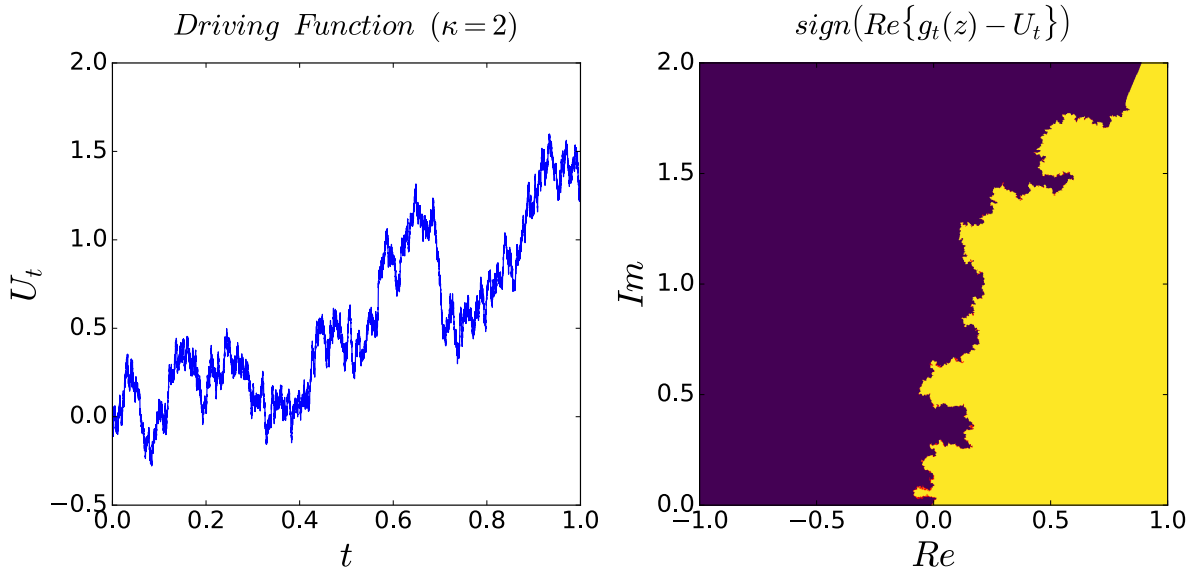

Figure 33 – Simulation of an SLE process with $\kappa = 2$ using the Euler method with $\Delta t = 10^{-5}$ in a grid of resolution $(1024, 1024)$. Because at time t $g_t(\gamma_t) - U_t = 0$, if we color the upper half plane according to which side of the real line each point is mapped, the border between the regions should indicate the position of the trace γ_t. The red points are the points where the method failed and were mapped outside the upper half plane. The smooth "tail" of the trace happens because these points have not yet been mapped to the real line.

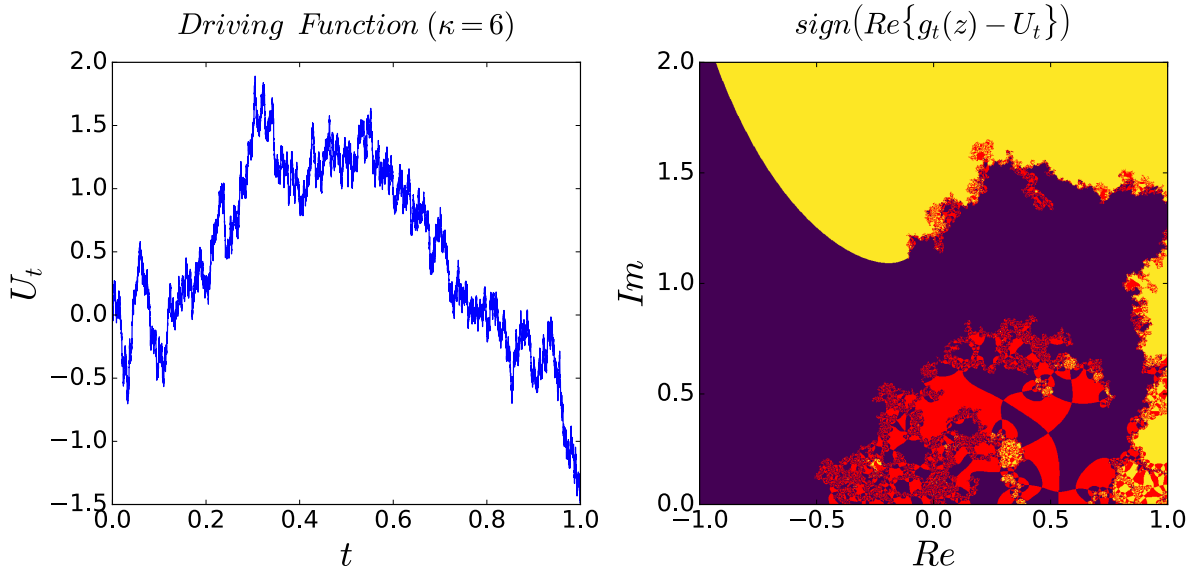

Figure 34 – Simulation of an SLE process with $\kappa = 6$ using the Euler method with $\Delta t = 10^{-5}$ in a grid of resolution $(1024, 1024)$. The red points are the points where the method failed and were mapped outside the upper half plane. The algorithm performed much worse than the case $\kappa = 2$.

In order to obtain the trace from g_t we take the fact that

$$g_t(\gamma_t) = U_t. \tag{3.20}$$

You can use your favorite method of root finding to solve Eq. 3.20 for γ_t. Figure 33 shows a realization for $\kappa = 2$. In it we colored the grid according to the sign of $Re\{g_t(z) - U_t\}$. The border between the positive and negative sides should be around the region where the trace is. We also observe the most blatant drawback of the method: it fails in several points, where they get mapped outside the upper half plane, which is not allowed in chordal Loewner's evolutions. This problem accentuates quickly as the value of κ rises, to the point where the case $\kappa = 6$ (Figure 34) has barely any discernible trace.

Other problem with Euler's method in the context of Loewner evolutions is computational complexity. It requires $O(N)$ for each point of the space where you compute $g_t(z)$, considering that you use a (M, M) regular grid, the whole algorithm have complexity $O(NM^2)$. This is further aggravated by the fact the most points are not necessary to actually compute the trace, making most of the computational effort useless. One possible advantage is the fact that this algorithm is highly parallelizable, although this is hardly an advantage faced with the other drawbacks.

3.4.2 Zipper Algorithm

Since the Euler's method perform so poorly in the task of computing the SLE trace, a better method is needed. The one described here is called the *zipper algorithm*, and it is used throughout this work. It is based on the idea of discrete Loewner evolutions [120, 121], series of smaller simpler Loewner evolutions.

For starters, we take a driving function U_t sampled in a set of $N + 1$ time instants $0 = t_0 < t_1 < \cdots < t_N$. As we already established, the solution of the Loewner's equation for U_t is g_t, which maps $\mathbb{H} \setminus \gamma_{[0,t_k]}$ to $\mathbb{H}$. We then define the helper function

$$G_k = g_{t_k} \circ g_{t_{k-1}}^{-1}, \tag{3.21}$$

which maps $\mathbb{H} \setminus \gamma_{[0,t_{k-1}]}$ to $\mathbb{H} \setminus \gamma_{[0,t_k]}$. This way the solution of Loewner's equation can be rewritten

$$g_{t_k} = G_k \circ G_{k-1} \circ \cdots \circ G_2 \circ G_1. \tag{3.22}$$

The G_k however are not solutions of Loewner's equation, as the trace they generate do not start at the origin. We fix that by shifting the function by $U_{t_{k-1}}$

$$g_k = G_k\left(z + U_{t_{k-1}}\right) - U_{t_{k-1}}. \tag{3.23}$$

Note that in the notation adopted (taken from [121]) g_{t_k} and g_k are different functions. The g_k are the solution of Loewner's equation with driving function $\tilde{U}_t$ such that $\tilde{U}_0 = 0$

and $\tilde{U}_{\Delta t_k} = \Delta U_k$, where $\Delta t_k = t_k - t_{k-1}$ and $\Delta U_k = U_k - U_{k-1}$. Since we are trying to construct the trace starting from the drive, we need to take the inverse of g_k

$$f_k = G_k^{-1}\left(z + U_{t_{k-1}}\right) - U_{t_{k-1}}. \tag{3.24}$$

The k-th point of the trace γ_{t_k} is then determined by

$$\gamma_{t_k} = f_1(\cdots f_{k-1}(f_k(\Delta U_k) + \Delta U_{k-1}) \cdots + \Delta U_1). \tag{3.25}$$

For convenience we define

$$h_k = f_k\left(z + \Delta U_k\right), \tag{3.26}$$

so the γ_t can be computed by applying the relation

$$\gamma_k = h_1 \circ h_2 \circ \cdots \circ h_k\left(0\right). \tag{3.27}$$

If this helper function zoo looks confusing, Figure 35 shows where they fit in the actual Loewner evolution process taking place.

Once the functional form of the h_k is know, the algorithm is surprisingly simple, it just consists of applying Eq. 3.27 for each value of k. The form of h_k however is dependent on the interpolation drive $\tilde{U}$. The choice is basically free, however a convenient one should have an analytical solution. The two most common are the vertical and tilted slits.

The vertical slit is done by making

$$\tilde{U}(t) = \Delta U, \tag{3.28}$$

which generate a vertical trace going from ΔU to $\Delta U + i2\sqrt{\Delta t}$. This is not strictly a Loewner evolution because the trace does not start at the origin, but this is a numerical approximation where the actual trace is a composition of many vertical slits, and the limit $\Delta t \to 0$ converges to an actual SLE trace. The h_k in this case is given by [122]

$$h_k(z) = i\sqrt{4\Delta t - z^2} + \Delta U. \tag{3.29}$$

The tilted slit is done by interpolating the drive with the function.

$$\tilde{U}(t) = \frac{2\left(1-2\alpha\right)}{\sqrt{\alpha\left(1-\alpha\right)}}\sqrt{t} \tag{3.30}$$

where

$$\alpha = \frac{1}{2} - \operatorname{sign}\left(\Delta U\right)\frac{1}{2}\sqrt{\frac{v}{16+v}}, \qquad v = \frac{\Delta U^2}{\Delta t}. \tag{3.31}$$

It generates a trace that is a tilted line that starts at the origin makes an angle $\alpha\pi$ with the positive real line. The h_k in this case is given by

$$h_k(z) = \left(z + 2\sqrt{\frac{\left(1-\alpha\right)\Delta t}{\alpha}}\right)^{1-\alpha}\left(z - 2\sqrt{\frac{\alpha\Delta t}{1-\alpha}}\right)^{\alpha}. \tag{3.32}$$

This discretization is more rigorous than the vertical slit, however in practice they yield very similar results. See Figure 36 for an illustration of the whole process of applying repeated tilted slits to obtain an SLE trace.

You can see in Figure 37 how the zipper algorithm performs in the high κ regime. The result is not perfect, the jump size $|\gamma_k - \gamma_{k-1}|$ is very non-uniform due to the high volatility of the driving function. Nevertheless, the result is still much better than the one obtained by using Euler's method, and the defects can be mitigated by simply adding more points to the discretized driving function. This is not so simple, however. Since each k-th point require k application of the h_i, the algorithm scales as $O(N^2)$, which can get unwieldy for very large N. One possible solution is making use of parallelization, since each γ_k can be computed independently from one another. There's also more complex approximative algorithms with better time complexity, up to $O(N^{1.4})$ [123].

The next challenge is to do the opposite task, obtaining a driving function from a given trace γ_k. This is much simpler when using a vertical slit. First let us invert Equation 3.27

$$0 = h_k^{-1} \circ h_{k-1}^{-1} \circ \cdots h_1^{-1}(\gamma_k). \tag{3.33}$$

We know that the vertical slit maps the origin to $\Delta U + i2\sqrt{\Delta t}$, that is

$$h_k(0) = \Delta U + i2\sqrt{\Delta t}. \tag{3.34}$$

Combining Eq. 3.33 and Eq. 3.34 we have

$$\Delta U_k + i2\sqrt{\Delta t_k} = h_{k-1}^{-1} \circ \cdots h_1^{-1}(\gamma_k). \tag{3.35}$$

This way we can determine the t_k and U_{t_k} of given discretized trace by simply taking

$$U_{t_k} = \sum_{i=1}^{k} \mathrm{Re}\{\omega_i\}, \qquad t_k = \frac{1}{4}\sum_{i=1}^{k} \mathrm{Im}\{\omega_i\}^2 \tag{3.36}$$

where

$$\omega_k = h_{k-1}^{-1} \circ h_{k-2}^{-1} \circ \ldots \circ h_1^{-1}(\gamma_k). \tag{3.37}$$

The h_k^{-1} can be easily determined by inverting Eq. 3.29

$$h_k^{-1}(z) = i\sqrt{-Im\{\omega_k\}^2 - (z - \mathrm{Re}\{\omega_k\})^2}. \tag{3.38}$$

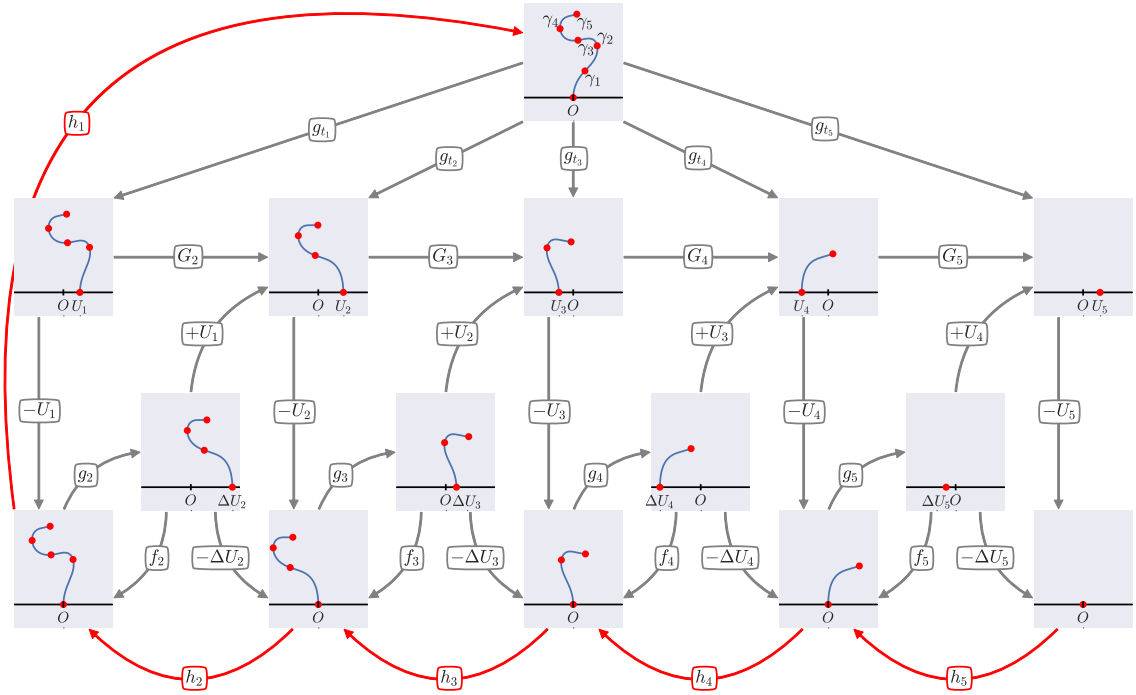

Figure 35 – Schematic representation of how the zipper algorithm fits in the Loewner evolution framework. At the top, we have the full trace up to time t_5, which we want to reach starting from the empty upper half plane (right most panel on the fourth row). To compute the trace from a given discretized driving function, one must take the red path. This is achieved by using the interpolating maps g_i that are the solution of the Loewner equation with driving function $\tilde{U}_0 = 0$ and $\tilde{U}_{\Delta t} = \Delta U$. The choice of interpolation function $\tilde{U}$ is arbitrary, but usually taken from the few options that have an analytical solution.

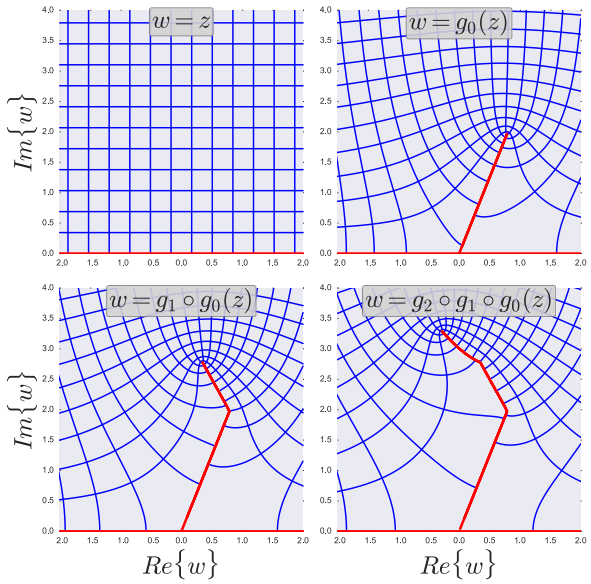

Figure 36 – Result of applying the first three iterations of the zipper algorithm with the tilted slit approximation. In the limit $\Delta t \to 0$ the red line converges to an SLE trace.

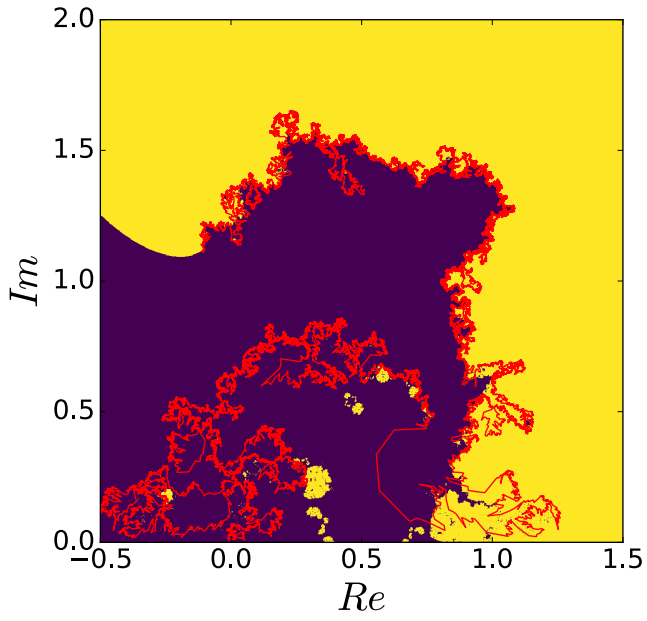

Figure 37 – Comparison of the traces obtained by using the zipper algorithm (red line) and Euler's method. Although it presents large jumps in the trace due to large displacements in the driving function, zipper it still performs better than the Euler's.

4 Loewner Evolutions of Anisotropic Systems

In this work we explore the possibility of using Loewner evolutions to study anisotropic fractal systems, i.e., systems with different critical exponents in each direction. These systems are not scale invariant, therefore not conformally invariant either. We are particularly interested in the two variants of the percolation model that show anisotropic behavior presented in Sections 2.5.1 and 2.5.2, namely, multi-layered percolation and directed percolation. Precisely, we generate the border of percolating clusters (see Figure 38), numerically compute their corresponding driving function, and then analyze the diffusive properties of these numerical sequences. In the general case, we expect that the mean square displacement of U_t behaves like,

$$\left\langle U_t^2 \right\rangle \to bt^{\alpha} \tag{4.1}$$

as $t \to \infty$. In the case of traditional SLE, $\alpha = 1$ and $b = \kappa$. The driving functions of anisotropic percolation models, we found, display very distinctive anomalous diffusive behavior ($\alpha \neq 1$). We also look at the presence of long range correlations in the driving function using the detrended fluctuation analysis (DFA). Finally, we show that our approach is also valid in the opposite direction, that SLE consistently leads anomalously diffusive driving functions to traces that display clear anisotropic scaling. To test that, we generate Loewner traces driven by fractional Brownian motions with different values of b and $H = \alpha/2$, which we will refer as $SLE(b, H)$, and compare the scaling properties of the traces obtained with those of the lattice models.

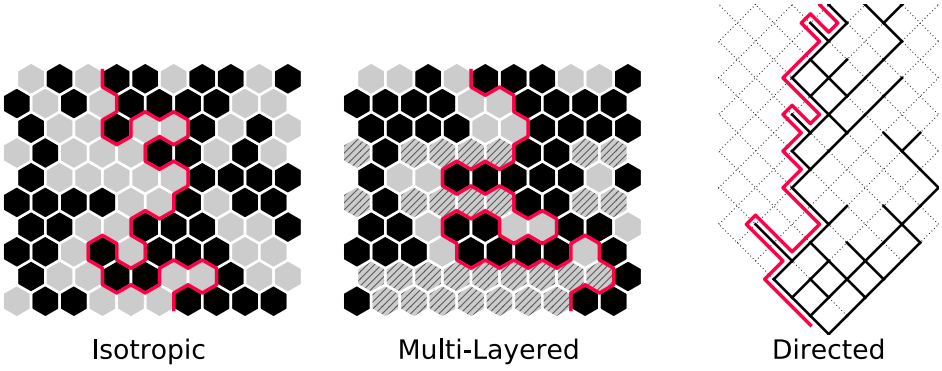

Figure 38 – Percolation models used to generate the SLE curves. Isotropic percolation (left), where each site is occupied with the same probability p. Multi-layered percolation (middle), where some rows are occupied with probability $p + \Delta$ (dark gray rows) and others with $p - \Delta$ (light gray rows). Directed percolation (right) is a spreading process which starts at the bottom of the tilted lattice and can only advance upwards with probability p. The trace is defined as the perimeter of the percolating cluster.

4.1 Methods

Before delving into our results, we shall give a brief overview of some of the most important methods used in the simulation and analysis of both traces and driving functions.

4.1.1 Generating Large Percolation Traces

Simulating the percolation process and extracting the percolating cluster perimeter is very straightforward and a number of good algorithms are available. However, because of the spotty behavior of the zipper algorithm (see Fig. 37) in the high κ (> 4) domain, we need very large traces in order to obtain reliable results. The usual algorithms are normally very memory hungry because you need to store the state of all sites of the lattice. Since we are only interested in obtaining the perimeter of the percolating cluster, which consists of only a small portion of the lattice, one might imagine if there is a more efficient way of simulating these curves. Luckily there is, thanks to the locality property of the percolation model. The method is called the *percolation exploration process* [22].

The exploration process is easier to define in the triangular lattice, because at any given time the walker is always facing a single site, unlike the square lattice, in which it faces two sites at once, complicating things a little (it does not make it impossible, though). In the exploration process, a walker is put in an initial position at the bottom of the

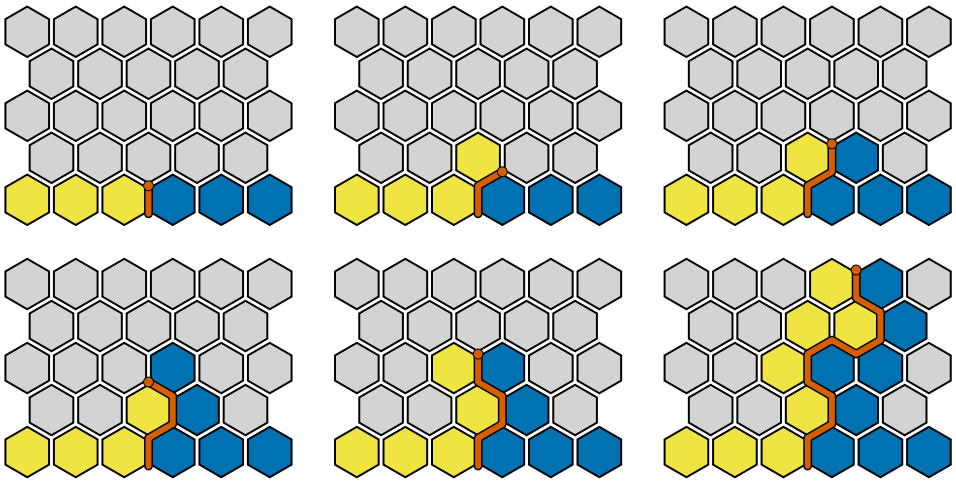

Figure 39 – The first few steps of a percolation exploration process with closed boundary conditions in a triangular lattice, which means the left side of the bottom row is always unoccupied (yellow) and the right side is always occupied (blue). At each step, the walker checks the status of the site right in front of it. If it is yellow, the walker turns clockwise and takes a step. If it is blue it turns counter-clockwise before taking a step. This method is superior because you only need to store the information about the sites adjacent to the curve, saving RAM and allowing for simulations of very large traces.

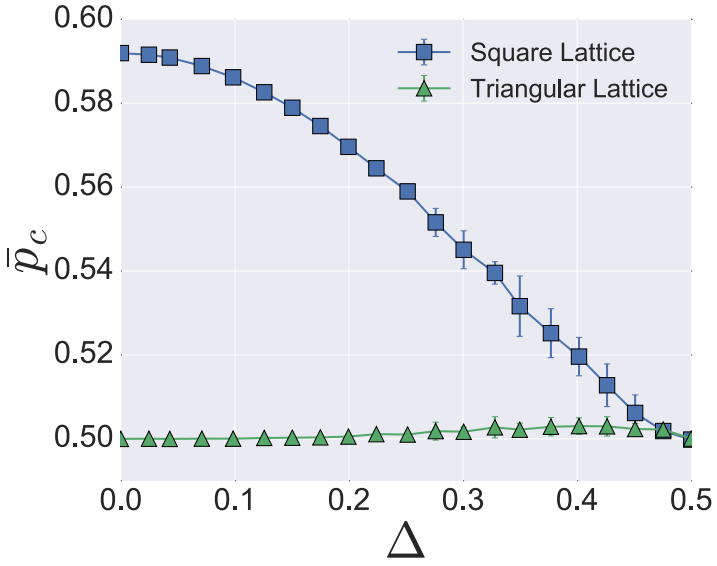

Figure 40 – Critical point of multi-layered percolation as computed using the cluster perimeter method. This is done by generating several percolation perimeters without boundary conditions until they form a loop. In the critical point the loop has equal probabilities of being a internal or external perimeter. We found that in the triangular lattice, $p_c = 0.5$ for every value of Δ, unlike the square lattice.

lattice. The walker observes the state of the site right in front of him. If it is unoccupied, the walker turns clockwise, otherwise it turns counter-clockwise. Then the walker takes a step in the direction it is facing. This process is then repeated until one obtain a curve long enough. The algorithm guarantees that the curve will not self-intersect and will not get trapped.

Because we restrict ourselves to chordal SLE, the walker can never leave the upper-half plane. To assure this, we impose closed boundary conditions in which the left side of the bottom row of the lattice is always unoccupied and the right side is always occupied. This way the trace will always turn away from the real line.

It is pretty clear the advantage of this method, you only need to store the information about the sites directly adjacent to the perimeter, which can be cached in your container of preference, like a hash table (also known as maps or dictionaries), as illustrated in Figure 39. This allow us to simulate traces with up to million points. In fact we could easily go above that, the limiting factor being the time the zipper algorithm takes to compute the driving function.

We used the exploration process to generate the traces for isotropic and multi-layered percolation in a triangular lattice. However, the critical point of multi-layered percolation have not yet been determined in the triangular lattice. To compute $p_c(\Delta)$ we made use the cluster perimeter method [124]. We basically use the exploration process

with no boundary condition to generate curves until they form a loop. If the loop is formed clockwise, this means it represents the perimeter of a hole inside a cluster. If it is counterclockwise, it means the curve is the outside perimeter of cluster. On the critical point, the probability that a loop is internal or external is the same. We found, somewhat surprisingly, that in the triangular lattice, $p_c = 0.5$ for every value of Δ, unlike the square lattice, as shown in Figure 40.

This algorithm is not appropriate for the simulation of directed percolation traces, because the occupation probability of any given site is not independent from its neighbors. In this case we decided for a more standard approach, growing a cluster using a graph data structure to save memory, and finding the perimeter using a simple walker algorithm, where the trace is the trajectory of a particle that moves along the border of the cluster while keeping the cluster always at to right hand side.

4.1.2 Detrended Fluctuation Analysis

We want to test whether or not the driving functions present long range correlations. Other works have shown that some form of anisotropy can be observed in SLE traces driven by Lévy processes. We have good reasons to believe this is not the case for multi-layered and directed percolation, because Lévy processes do not show subdiffusion and they generate discontinuous traces.

In order to close the issue we perform one last test: check for the presence of long range correlations. To do that we employ a method called Detrended Fluctuation Analysis (DFA), which is an adaptation of an older algorithm called simply fluctuation analysis. It is specially designed for the analysis of non stationary series [125, 126] with the objective of computing their Hurst exponent H. This quantity measure the presence of long term correlations, and is found in the interval $H \in [0, 1]$, where $H = 0.5$ means that the series has no long range correlations. The case $H < 0.5$ means the series is anti-persistent, so fluctuations in one direction tend be followed by fluctuations in the opposite direction. When $H > 0.5$, the series is persistent [127] and fluctuations tend to happen in the same direction.

Given a time series of N data points $\{x_i\}$, we first generate a random walk out of it by making the cumulative profile of the series

$$X_i = \sum_{j=1}^{i} (x_j - \langle x \rangle) \,. \tag{4.2}$$

The accumulated series is then divided in m non overlapping partitions, each with $s = N/m$ elements. In case N is not divisible by m we can still make use of the last elements of the series by taking $s = \lfloor N/m \rfloor$ and reflecting it in the end the following way

$$X \to \{X_1, \ldots, X_{ms}, X_N, X_{N-1}, \ldots, X_{N-ms}\} \,. \tag{4.3}$$

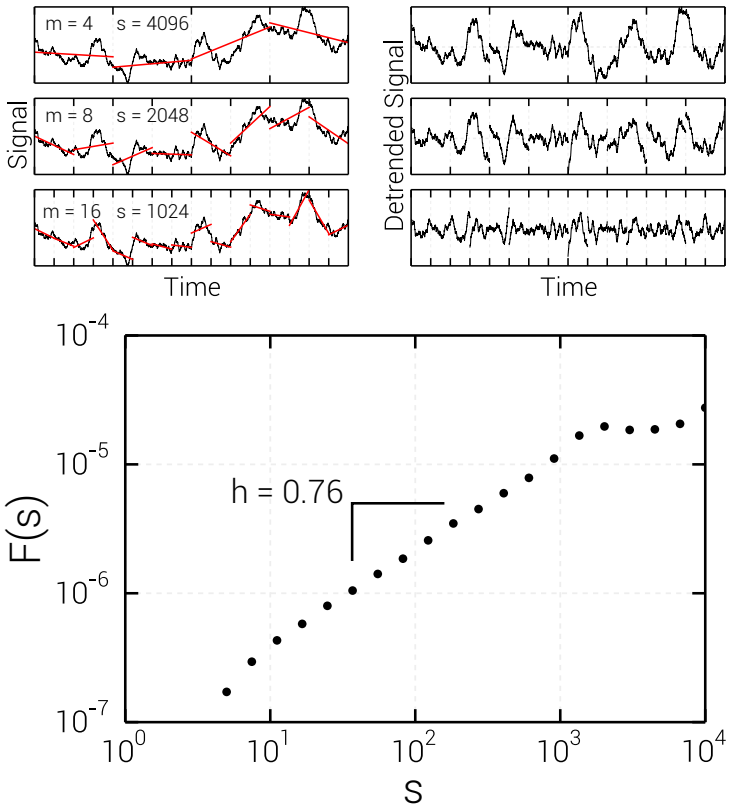

Figure 41 – The Detrended Fluctuation Analysis (DFA) of a time series of $N = 16,384$ data points. First we divided the series in m partitions with s points each (top-left), then fitted each separately with a first order polynomial $f_1(i)$ (red lines), obtaining the detrended series by subtracting the signal by the trend (top-right). The fluctuation function (the standard deviation of the detrended signal) is computed for various values of s (bottom). The Hurst exponent is then determined by fitting the fluctuation function with a power law $F(s) \sim s^h$.

In this case we actually changed the series size to $N \to 2ms$ and the number of intervals to $m \to 2m$, so this should be taken in account in later equations. This step is optional, but useful in order to use all the information embedded in the time series.

We then determined the trend of each partition by fitting them separately using a polynomial of degree v. Usually a first or second degree polynomial is chosen. The series is detrended by taking the difference of the signal value and the trend

$$Y_i = \sum_{i=1}^{N} X_i - f_v(i), \tag{4.4}$$

where $f_v(i)$ is the value of the trend in the point i. We define the fluctuation function as the standard deviation of the detrended signal, which is a function of the number of points s in each partition of the time series

$$F(s) = \sqrt{\frac{1}{N} \sum_{i=1}^{N} Y_i^2}. \tag{4.5}$$

A plot of $F(s)$ vs. s in a log-log scale should show a straight line for well a behaved series (see Fig. 41). The Hurst exponent of the series can be determined by fitting the fluctuation function with a power law

$$F(s) \sim s^H. \tag{4.6}$$

4.1.3 Generating Fractional Brownian Motions

We want to generate fractional Brownian motions B_t such that

$$\left\langle B_t^2 \right\rangle = bt^{2H}. \tag{4.7}$$

There are several methods to generate this process numerically, but not all of them give you ample control over the prefactor b, although most are very accurate in H. A method that adequately fulfills this criterion is the Davies-Harte algorithm [128]. It can be used to generate any stationary Gaussian process for which the autocovariance sequence is known. In the case of the fractional Brownian motion, it takes the form

$$c_i = \frac{b}{2}\left(|i+1|^{2H} + |i-1|^{2H} - 2\,|i|^{2H}\right) \tag{4.8}$$

To obtain a series of length N we generate the following sequence of $2N$ points

$$s_i = \{c_0, c_1, \ldots, c_N, c_{N-1}, \ldots, c_1\} \tag{4.9}$$

and compute its discrete Fourier transform, that is

$$g_i = \sum_j s_j e^{-i\pi kj/N}. \tag{4.10}$$

This operation can be done in $O(N \log N)$ operations using a fast Fourier transform [129]. The g_i are real valued, but a necessary condition for the Davies-Harte algorithm to work is that they also be nonnegative. It is important to check for this condition even if just for debugging purposes, as it catches a lot of small mistakes.

Finally, we define a series $W_{i\in[0,N]}$ to be a sequence of $N+1$ random complex numbers where the real and imaginary parts are independently distributed according to a normal distribution with zero mean and unit variance. We then construct the series

$$Y_{i\in[0,2N-1]} = \begin{cases} \sqrt{2Ng_i}\,\mathrm{Re}\,\{W_i\} & \text{if } i = 0, N \\ \sqrt{Ng_i}\,W_i & \text{if } i \in [1, N-1] \\ \sqrt{Ng_i}\,W^*_{2N-i} & \text{if } i \in [N+1, 2N-1] \end{cases}, \tag{4.11}$$

where W^* is the complex conjugate. The fractional Brownian motion B_t is obtained by computing the inverse Fourier transform of this series. Although the obtained series have $2N$ points we discard the second half, as it is not guaranteed to be well behaved. The B_t

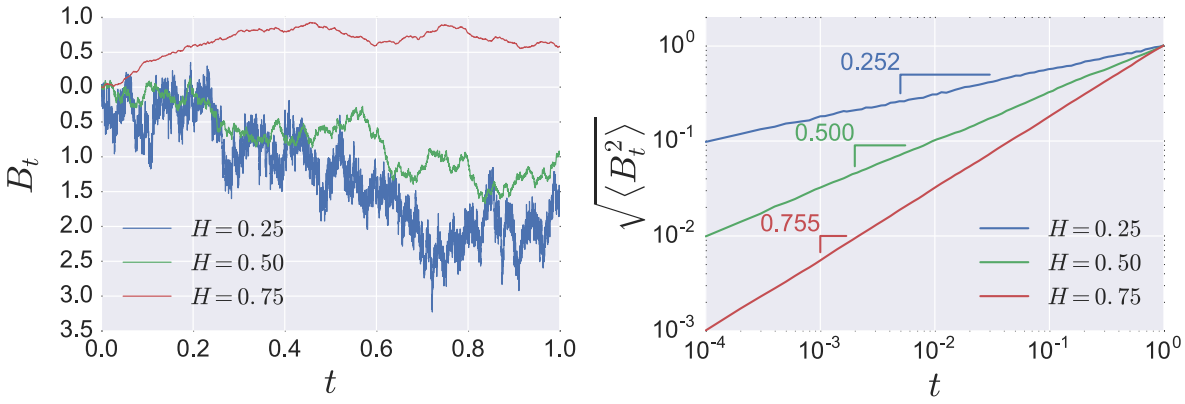

Figure 42 – Example of three fractional Brownian motions generated using the Davies-Harte algorithm (left). They all have $b = 1.0$ and different values of H. We also show the behavior of the mean square displacement of the scaling properties of the curves. We found that the mean square displacement scales as $\sqrt{\langle B_t^2 \rangle} = \sqrt{b} t^H$ with parameters very similar to the input given.

are defined for $t \in 0, 1, \ldots, N-1$, but the series can easily be rescaled for any timespan desirable by applying the relation

$$B_{t\in[0,t_f]} = \left(\frac{t_f}{N}\right)^H B_{t\in[0,N]}. \tag{4.12}$$

In Figure 42, we show some examples of fractional Brownian motion generated using this algorithm. We also show that the mean squared displacement behaves as described by Eq. 4.7.

4.2 Results and Discussion

As mentioned, we set up to study the properties of the driving functions of traces generated by multi-layered and directed percolation. As a control for our tests we also analyzed isotropic percolation, which is well understood theoretically.

We generated an ensemble of 10^4 cluster perimeters for each model at criticality. Isotropic and multi-layered curves were generated on a triangular lattice, while the directed percolation ones were done in a square lattice. The traces had a length of 10^5 lattice units. Using the zipper algorithm described in Section 3.4.2, we computed the driving function of each curve. The output of the algorithm is a sequence of time instants and their respective value of the drive, $\{(t_0 = 0, U_{t_0} = 0), (t_1, U_{t_1}), \ldots, (t_N, U_{t_N})\}$. This algorithm, however, does not guarantee that the discretized times t_i are equally spaced, even for curves of same length and step size. To facilitate further analysis, we create a new sequence $\{(\tilde{t}_0, U_{\tilde{t}_0}), (\tilde{t}_1, U_{\tilde{t}_1}), \ldots, (\tilde{t}_M, U_{\tilde{t}_M})\}$, where $\tilde{t}_k = t_f^{k/M}$ and $U_{\tilde{t}_k}$ is computed through a linear interpolation of the U_{t_i}. We used $M = 20,000$ and the values of t_f were different for each

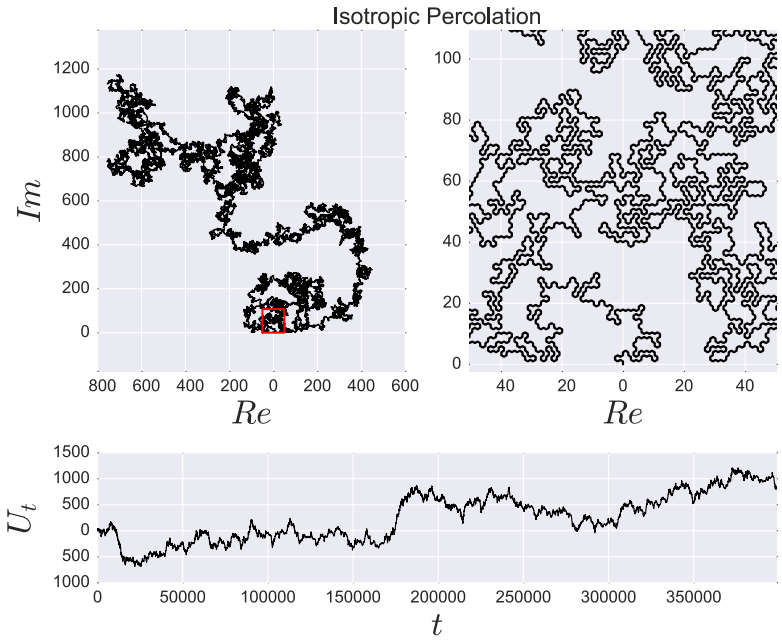

Figure 43 – Example of a cluster perimeter of the isotropic percolation model in the triangular lattice with a detail shown. The bottom graph is the driving function obtained by applying the zipper algorithm to this trace.

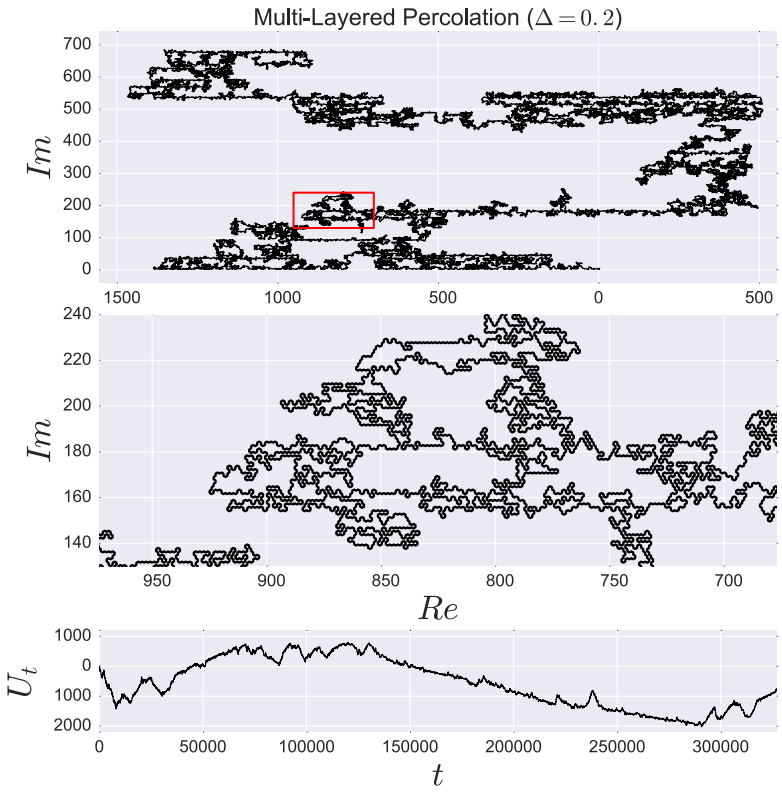

Figure 44 – Example of a cluster perimeter of the multi-layered percolation model in the triangular lattice ($\Delta = 0.2$) with a detail shown. The bottom graph is the driving function obtained by applying the zipper algorithm to this trace.

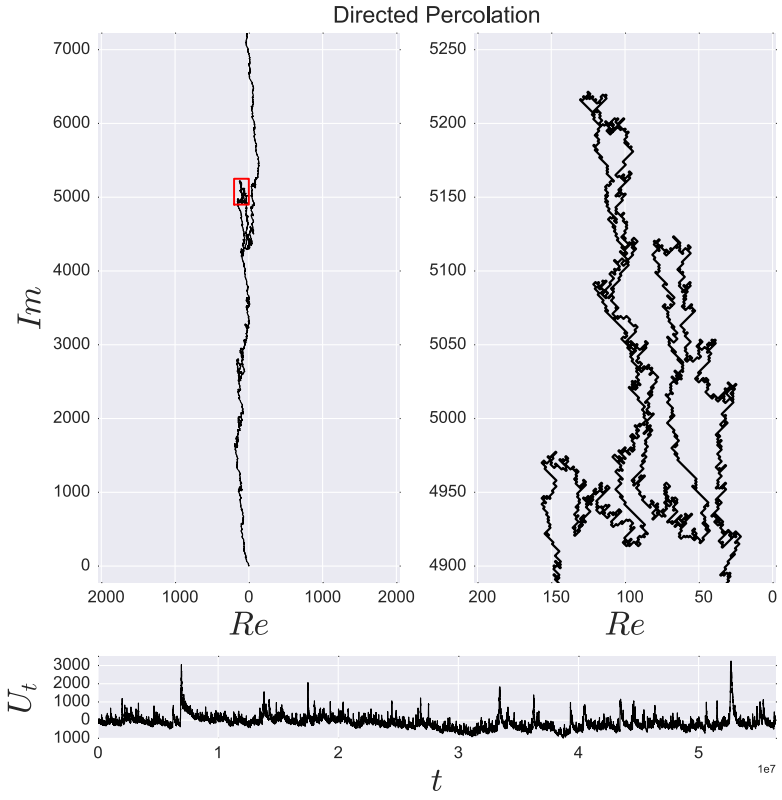

Figure 45 – Example of a cluster perimeter of the bond directed percolation model in the square lattice with a detail shown. The bottom graph is the driving function obtained by applying the zipper algorithm to this trace.

model chosen as the smallest value of t_N among all the samples. The exact values can be found in Table 5. Figures 43, 44, and 45 show examples of the kind of curves obtained as well as their computed driving function.

4.2.1 Diffusion analysis

We can now analyze the diffusive properties of the driving function. We do this by looking at the mean square displacement, that it, $\langle U_t^2 \rangle$, where $\langle \cdot \rangle$ is the mean over the samples. As mentioned in Section 3.3, we expect that

$$\left\langle U_t^2 \right\rangle \sim bt^{\alpha}. \tag{4.13}$$

In a log-log graph the means squared displacement should appear as a line, so we can obtain the values of b and α through an ordinary least square fitting. Figure 46 show the results and the exact values of b and α obtained can be found in Table 4. We observed the expected behavior from the isotropic percolation with $\alpha \approx 1.0$ and $b \approx 6.2 \pm 0.3$, which is coherent with the expected value of $b = \kappa = 6$. The large error bar is a result of the spotty behavior of the zipper algorithm in the high (> 4) κ [123].

In the multi-layered case, the mean square displacement exhibits characteristic superdiffusive behavior for every value of $\Delta > 0$. As can be observed in Figure 46, however, a long transient behavior is present for small values of Δ before a distinctive power-law behavior is established. For $\Delta = 0.4$, after a short transient, the fit of the data gives a power-law with $b = 10.38 \pm 0.68$ and $\alpha = 1.78 \pm 0.01$, which extends over more than three orders of magnitude. The multi-layered model is expected to have the same continuum limit for every value of $\Delta > 0$ [79], which should translate in driving functions with identical exponents as $t \to \infty$ in all cases. While a qualitative assessment of Figure 46 indicates that this seems to be the case, we could not establish this hypothesis numerically as it demands simulations of even larger traces; not possible with our current computational power in a timely manner.

Again, using the same simulation setup, we tested the perimeters of the spanning clusters of directed percolation. From the ensemble of the generated driving functions, once more the resulting mean square displacement displays a characteristic anomalous behavior. Precisely, the least-squares fit to the data in the scaling region yields subdiffusive diffusion, as shown in Figure 46, with a pre-factor $b = 3.74 \pm 0.07$ and an exponent $\alpha = 0.676 \pm 0.001$.

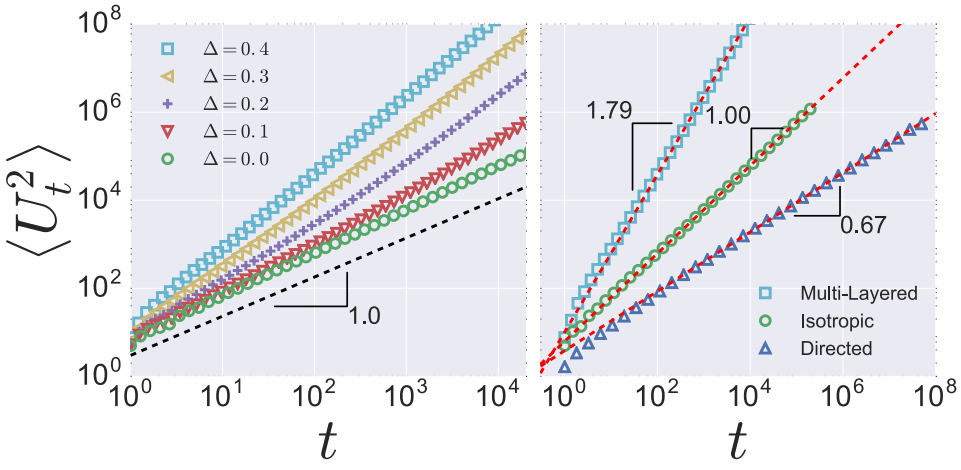

Figure 46 – Mean squared displacement of the driving functions for the three percolation models studied. The curves are the results of the numerical procedure described in the text applied to 10^4 realizations of each type of percolation model. As expected, in the case of isotropic percolation, the displacement scales linearly with time, while it shows instead a distinctive subdiffusive behavior for directed percolation, with an exponent $\alpha \approx 0.67$. In the case of multi-layered percolation, a clear superdiffusive behavior, with an exponent $\alpha \approx 1.79$, can be observed for $\Delta = 0.4$. The left graph shows this anomalous diffusion regime is gradually achieved as we increase the degree of anisotropy Δ.

Model	b	α
Isotropic	6.27 ± 0.30	0.996 ± 0.005
Multi-Layered	10.38 ± 0.68	1.78 ± 0.01
Directed	3.74 ± 0.07	0.676 ± 0.001

Table 4 – Diffusive properties of the driving function obtained from the cluster perimeters of each percolation model studied. In the general case the the mean square displacement evolves like $\langle U_t \rangle \sim bt^{\alpha}$. We observe the isotropic percolation display regular diffusion, as expected, while multi-layered and directed percolation are superdiffusive and subdiffusive respectively. The multi-layered case used $\Delta = 0.4$.

4.2.2 Hurst exponents

To get a better feel of what kind of stochastic process is behind the driving functions of our test models, we checked for the presence of long range correlations using the detrended fluctuation analysis (DFA, see Secion 4.1.2). The results are found in Figure 47. As expected, the Brownian motion of isotropic percolation is uncorrelated, with $H = 0.5$. Multi-layered percolation shows a strongly correlated exponent of $H = 0.8$, which is consistent with the superdiffusive behavior we found. The results of directed percolation, however, were not conclusive. The fluctuation function does not have a power-law behavior, so a Hurst exponent cannot be determined. This kind of anomaly can be caused by processes that are non-stationary in non-trivial ways [130, 131]. This suggests that the driving functions of directed percolation might be of a more complicated nature than that of isotropic and multi-layered percolation. Furthermore, we also added the DFA of Lévy processes, since these are the only kind of processes studied so far that are related to anisotropic scaling in SLE traces. This kind of process however have no long range correlations, as evidenced by the fact that $H = 0.5$, so the behaviors of multi-layered and directed percolation are not consistent with this kind of process.

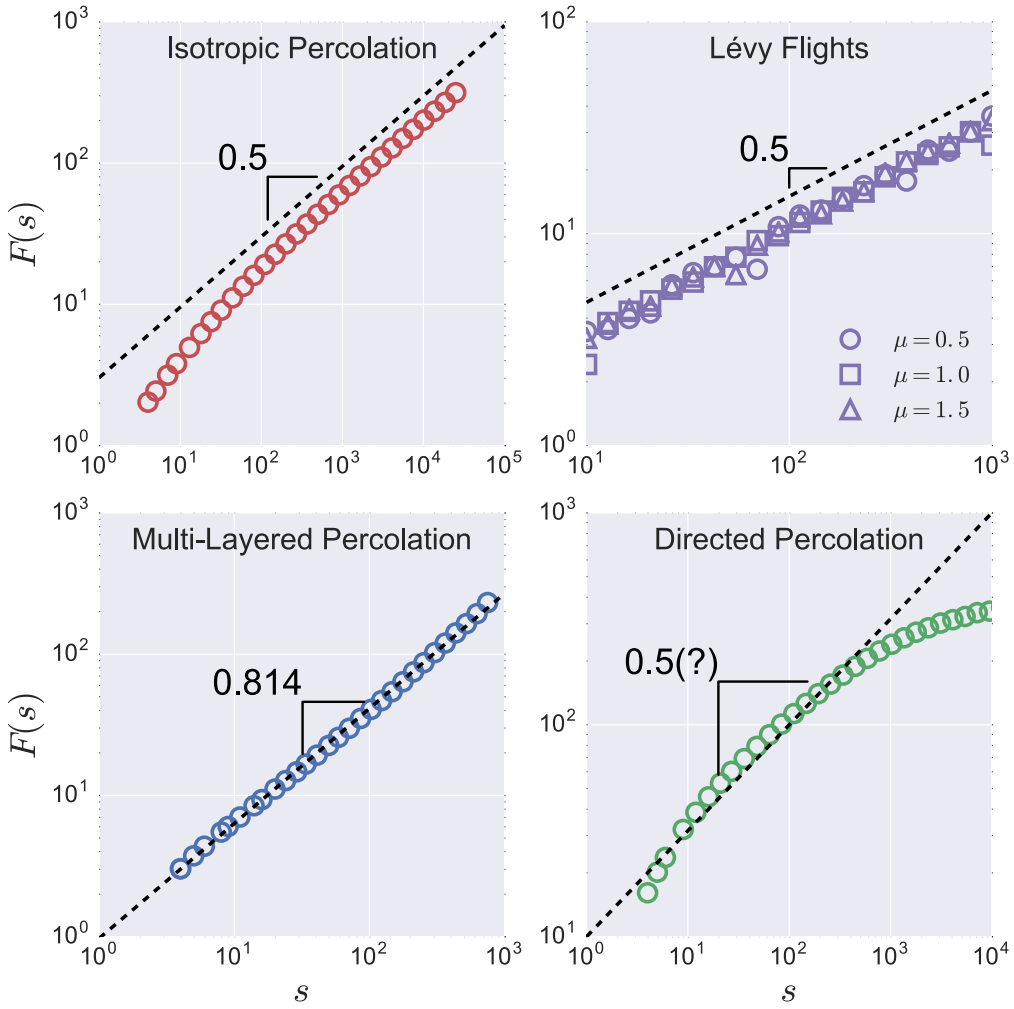

Figure 47 – Results of detrended fluctuation analysis (DFA) of the driving functions of percolation models. As expected, the driving function of the isotropic percolation (top left) is a Brownian motion, therefore have $H = 0.5$. For comparison the DFA of Lévy flights with several α is shown (top right). Despite displaying anomalous diffusion, it still have $H = 0.5$. Multi-layered percolation however shows a very distinct exponent $H = 0.814$, which is consistent with the diffusion exponent shown in Figure 46. The fluctuation function of directed percolation does not have a power-law behavior, which could be a result of non-trivial non-stationarity in the series..

4.2.3 SLE driven by fractional Brownian motions

The diffusion and DFA results suggest that the presence of long-range correlations and anomalous diffusion in the driving function should lead, through the Loewner evolution process, to the anisotropic fractal traces observed here, and vice-versa. In order to test this hypothesis, we analyze the behavior of traces driven by stochastic processes exhibiting both these characteristics. We choose to use fractional Brownian time series generated according to a given Hurst exponent H, which is related to the diffusion exponent by $\alpha = 2H$ [132]. So the mean square displacement evolves like

$$\left\langle U_t^2 \right\rangle \sim bt^{2H}. \tag{4.14}$$

We will refer to this variant of SLE, driven by fractional Brownian motion, as SLE(b, H).

We generated the drive U_t as a fractional Brownian Motion with Hurst exponent H and diffusion constant b in N time steps t_i uniformly spaced in the interval $[0, t_f]$. In order to simulate fractional Brownian motions with reasonable control over the diffusive constant b, we used the Davies-Harte algorithm (see Section 4.1.3). The γ_{t_i} were computed from U_{t_i} using the zipper algorithm (Eq. 3.36). We generated three ensembles of traces, each with a different set of parameters chosen according to the results of the diffusion and DFA analysis. Each ensemble has a reference model. The ensemble based on isotropic percolation had $H = 0.5$ and $b = 6$, as these are the theoretical values expected. The ensemble based on multi-layered percolation used $H = 0.8$ and $b = 16.0$, because these were approximately the values obtained in the previous analyses. And the direct percolation ensemble used $H = 0.33$ and $b = 3.8$, based on the diffusion exponent $\alpha = 0.66$ since we could not obtain an estimate of H. The values of all the parameters used can be seen in Table 5. The fractional Brownian motions generated are much like the ones in Figure 42 and some examples of the resulting traces are shown in Figure 48.

To generate traces long enough to allow for the next analyses, we relied on a GPU (graphics processing unit) parallelized [133] version of the Zipper algorithm. The parallelization was fairly straightforward, where each thread of execution computed a single point of the trace. We used a used a Nvidia graphics card model Quadro K5000 with 1536 CUDA cores.

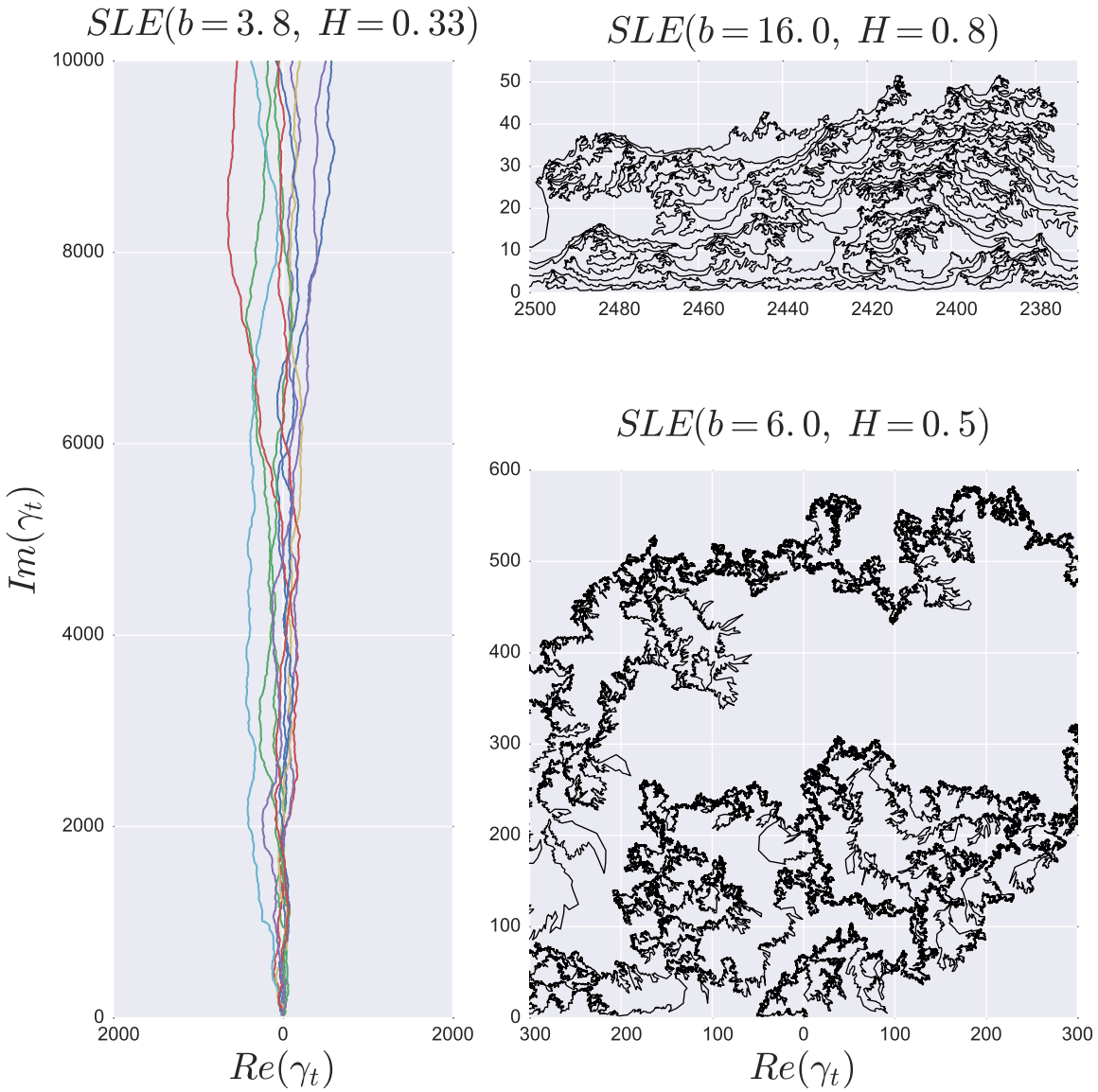

Figure 48 – Examples of $SLE(b, H)$ generate using the three sets of parameters that we drew from the diffusion analysis (Figure 46). For the correlated ($H > 0.5$) and uncorrelated ($H = 0.5$) we show one example of each. In the anticorrelated we show several instances. We used the zipper algorithm with 10^6 points equally spaced in the interval $t \in [0, t_f]$, where the values of t_f used can be found in Table 5.

4.2.4 Scaling analysis

We now set to study the scaling properties of the SLE(b, H) traces and compare with their respective reference models.

First we look at the spatial scaling, which amounts to measure the critical exponents $\bar{\nu}_x$ and $\bar{\nu}_y$. To do that, we reparametrize the trace as a function of its length instead of the time. This means we will have a sequence of points $\{\gamma(\ell_i)\}$, where

$$\ell_i = \sum_{j=1}^{i} |\gamma_j - \gamma_{j-1}| \,. \tag{4.15}$$

We then interpolate the trace $\gamma(\ell)$ in M equally spaced points $\ell_i \in [0, \ell_{\max}]$. The choices of M and $\ell_{\max}$ are shown in Table 5. We then compute the the root mean squared estimation of the displacement of the trace, that is,

$$F_X(id\ell) = \sqrt{\frac{1}{M-i} \sum_{j=0}^{M-i} [X(\ell_{j+i}) - X(\ell_j)]^2}, \tag{4.16}$$

where $X(\ell) = \mathrm{Re}\{\gamma(\ell)\}$ and $d\ell = \ell_i - \ell_{i-1} = \ell_{\max}/M$. Analogously, $F_Y(id\ell)$ is defined taking instead $Y(\ell) = \mathrm{Im}\{\gamma(\ell)\}$. These quantities should scale like, by taking $id\ell = \Delta\ell$,

$$F_X(\Delta\ell) \sim \Delta\ell^{\bar{\nu}_x}, \qquad F_Y(\Delta\ell) \sim \Delta\ell^{\bar{\nu}_y}. \tag{4.17}$$

This analysis was performed in the three ensembles of SLE(b, H) traces as well their reference models. The results are shown in Figure 49 and Table 6. Both isotropic percolation and $SLE(6.0,\ 0.5)$ yielded the expected value determined theoretically [124],

$$\bar{\nu}_x = \bar{\nu}_y = \frac{\nu}{1+\nu} = \frac{4}{7} \approx 0.571. \tag{4.18}$$

While the multi-layered and directed percolation exponents do not have theoretical values, they have established numerical values in the literature [79, 84]. We observed that the exponents for the multi-layered case and the SLE(16.0, 0.8) are also coherent with one another. However, the directed percolation case does not seems to match $SLE(3.8,\ 0.33)$. This is not completely unexpected in light of the results we got from the DFA. We did however found anisotropic exponents with the same preferential direction $\bar{\nu}_y > \bar{\nu}_x$.

We also looked at how the traces scale with the SLE time. To do this we looked at the characteristic length scales of the traces, $X(t)$ and $Y(t)$, equivalent to the width and height of the hull at time t. Much like with the spatial scaling, we compared the percolation models and their equivalent SLE(b, H). The results are shown in Figure 50. The isotropic percolation and SLE(6.0, 0.5) both have $X \approx Y\ t^{0.5}$, is in accordance with Eq. 3.16 with $\mu = 2$, again as expected. The multi-layered case is also behaves very similarly with the SLE(16.0, 0.8). Now, somewhat surprisingly, the directed percolation result seems to match

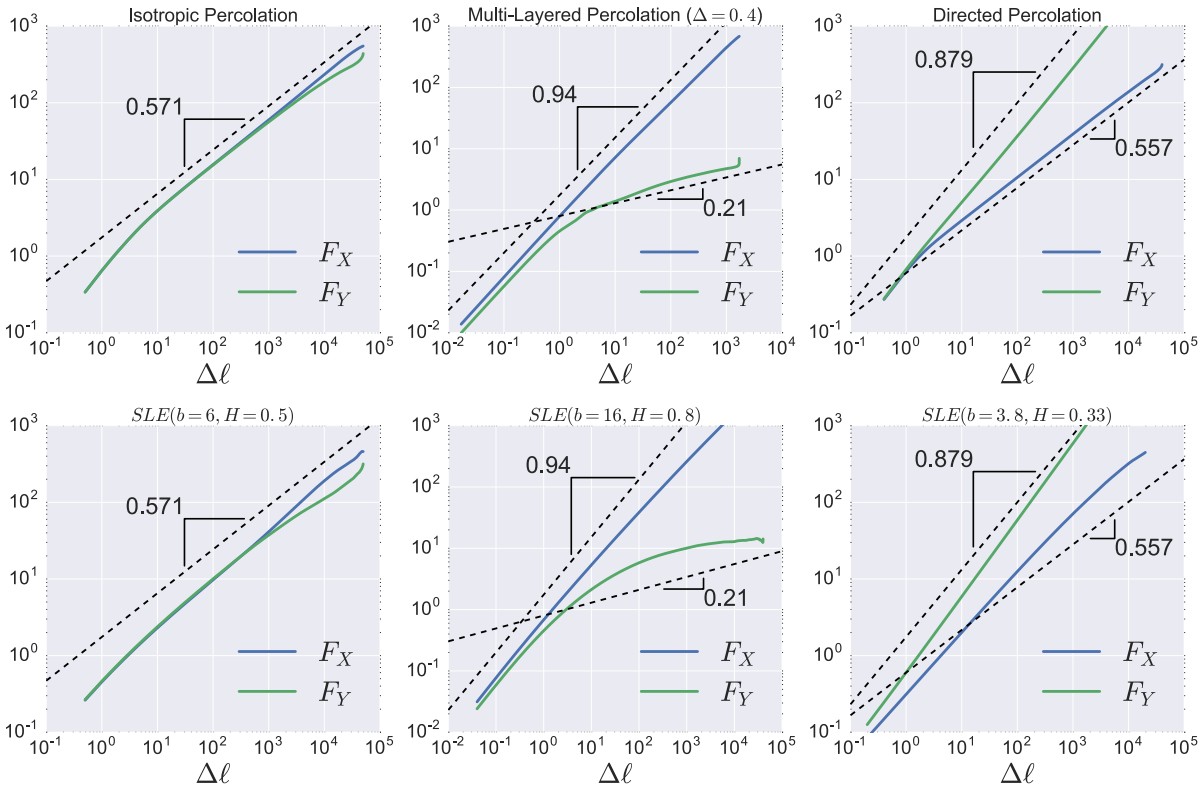

Figure 49 – Root mean squared estimations of the displacements in the X and Y-directions of SLE traces driven by long-range power-law correlated time series (fractional Brownian motion). The simulation parameters (H, b and t_f) were chosen based on the results shown in Fig. 46 (see Table 5 for the numerical values). Good agreement is observed between the uncorrelated result ($H = 0.5$) and isotropic percolation, as it is expected. The correlated trails ($H = 0.8$) are also compatible with multi-layered percolation (inset on the bottom). In the anti-correlated case ($H = 0.33$), the same kind of anisotropy present in the directed percolation is observed, however the exponents are not an exact match. These results support our hypothesis that long-term correlations in the driving functions, i.e., the presence of anomalous diffusion, are responsible for the anisotropic behavior of the traces. For the values of the exponents found, see Table 6.

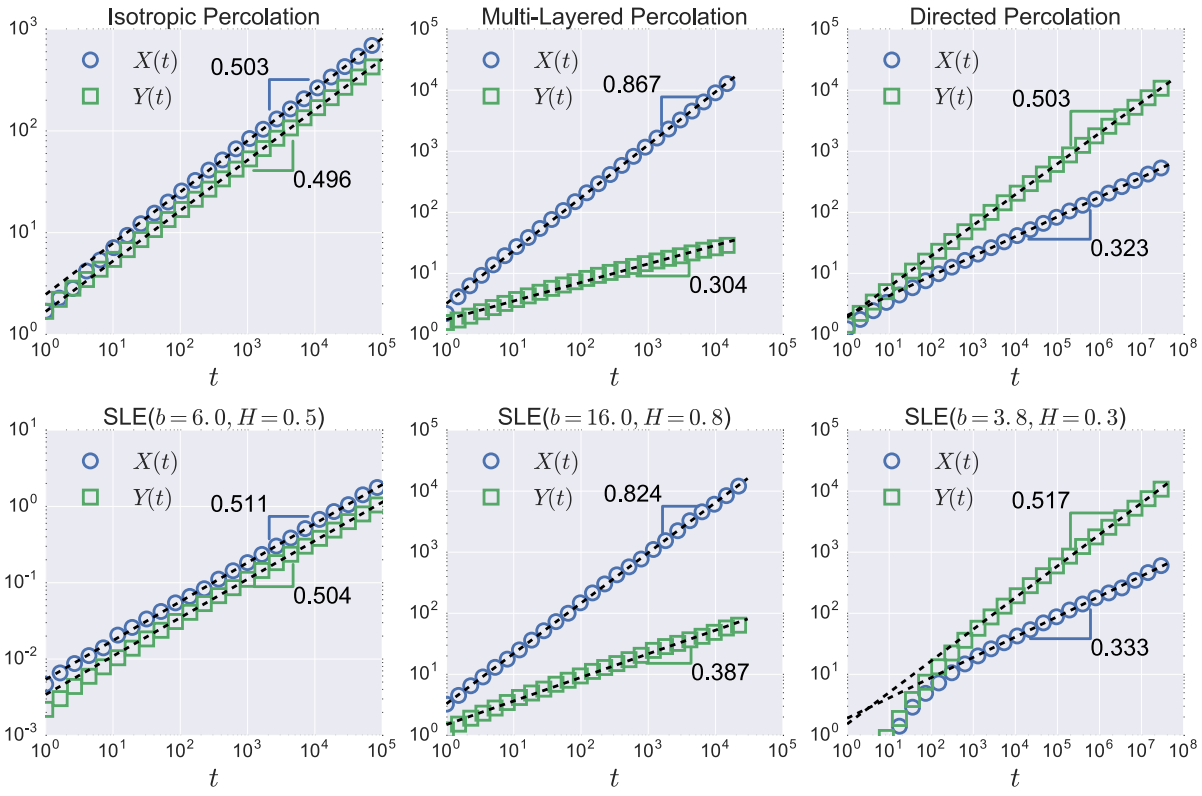

Figure 50 – Scaling analysis of the percolation models and their SLE equivalents. Here we observe how the total width, $X(t)$, and and height, $Y(t)$, of the traces evolve in time. According to the SLE time.

Reference Model	$\boldsymbol{H}$	$\boldsymbol{b}$	$\boldsymbol{t_f}$	$\boldsymbol{N}$	$\boldsymbol{M}$	$\boldsymbol{\ell_{\max}}$
Isotropic	0.5	6.0	2×10^5	10^6	10^5	2×10^4
Multi-Layered	0.8	16.0	3×10^4	10^6	10^5	8×10^4
Directed	0.33	3.8	5×10^7	10^6	10^5	2×10^4

Table 5 – Simulation parameters used to generate the SLE traces. H is the Hurst exponent and b is the diffusion coefficient of the fractional Brownian motion used as driving function. The curves were computed for N time instants t_i equally spaced in the interval $[0, t_f]$. The resulting trace is reparametrized as a function of its length and interpolated in M points equally spaced in the interval $[0, \ell_{\max}]$.

pretty closely the SLE$(3.8, 0.33)$ exponents, with $X \sim t^{0.33}$ and $Y \sim t^{0.5}$ approximately. It is unclear why this particular test showed similar exponents, while the spatial scaling did not. One possibility is that the temporal scaling of the traces is more influenced by the diffusive properties of the drive than by the presence of long range correlations.

		Isotropic	**Multi-Layered**	**Directed**
Literature	$\bar{\nu}_x$	0.571	0.94 ± 0.01	0.557 ± 0.001
	$\bar{\nu}_y$	0.571	0.21 ± 0.01	0.879 ± 0.001
MC Estimation	$\bar{\nu}_x$	0.573 ± 0.001	0.894 ± 0.001	0.559 ± 0.004
	$\bar{\nu}_y$	0.565 ± 0.001	0.289 ± 0.005	0.898 ± 0.001
SLE(b, H) **Estimation**	$\bar{\nu}_x$	0.62 ± 0.01	0.863 ± 0.003	0.73 ± 0.01
	$\bar{\nu}_y$	0.55 ± 0.01	0.21 ± 0.01	1.000 ± 0.001

Table 6 – Critical exponents $\bar{\nu}_x$ and $\bar{\nu}_y$ relative to the spatial scaling of the cluster perimeters in the three percolation models studied here. Literature values were taken from [124, 79, 84]. Isotropic percolation is the only one for which the exact value is know, $\bar{\nu}_x = \bar{\nu}_y = 4/7 \approx 0.571$. We estimated the exponents of each model using Monte Carlos methods, by generating cluster perimeters and using Eq. 4.16. We also estimated the exponents of their possible SLE(b, H) (using the parameters given in Table 5). There's reasonable accordance between the exponents of multi-layered and isotropic percolation, considering the limitations of the method. Directed percolation, however, is not a match, suggesting that it may not be described by a SLE(b, H).

5 Conclusion

So we reach the end of this work. We hope that by now we made clear the importance and impact that the study of critical systems has had in both physics and mathematics. In our research we took to ourselves to explore two little understood areas: strongly anisotropic systems and Schramm-Loewner evolutions driven by non-Brownian stochastic processes.

Strong anisotropy is the observed property that some systems have where several quantities behave differently depending on which direction you are measuring them. Particularly, we looked at two variants of the percolation model that display anisotropy. The first, Multi-layered percolation, was designed to simulate the transport properties in stratified (layered) media. The second, directed percolation, mimics the filtering of a fluid along a porous medium under the effect of gravity, so it flows only along a predetermined direction.

We generated an ensemble of cluster perimeters in isotropic, multi-layered, and directed percolation, then used the zipper algorithm to compute the driving function from these curves and, looking at their diffusive properties, we found that they are anomalously diffusive. Multi-layered percolation is associated with superdiffusive driving functions while directed percolation with subdiffusive ones. This is the first time a physical model has been associated to driving functions with these properties.

Furthermore, a detrended fluctuation analysis of the driving functions yielded mixed results. Multi-layered percolation showed a discernible positive correlation with a Hurst exponent $H \approx 0.8$. Directed percolation however had inconclusive results, where the fluctuation function did not behave as a power law, as it would be expected. This could happen because of irregular behaviors in the series, like non-stationarity or the presence of singularities.

In the second part of this work, we went one step further and looked at the opposite procedure, that is, what kind of traces we would obtain if we used anomalously diffusive processes as driving functions. We chose to use fractional Brownian motions with the parameters obtained from the previous analysis. We found that the resulting traces have a scaling behavior consistent with the multi-layered percolation. For directed percolation, again results were mixed. While the traces do not have spatial scaling exponents consistent with lattice model, the scaling in SLE time was surprisingly close.

In summary, our numerical analysis offers compelling evidence that a variation of the Stochastic Loewner Evolution, obtained by taking as driving function a stochastic process with anomalous diffusion, may be the scaling limit of anisotropic critical models.

In particular, multi-layered percolation seems to have as scaling limit an SLE driven by a fractional Brownian motion with hurst exponent $H \approx 0.8$ and diffusive constant $b \approx 16$. The same could not be asserted for the directed percolation case, indicating that there is more to strong anisotropy than simply anomalous diffusion. We expect that the further developments of this new variant of SLE may provide some insight on the critical behavior of anisotropic systems, the same way the original SLE was to isotropic systems.

APPENDIX A – Deriving Loewner's Equation

In this appendix we shall give an overview of the demonstration of Loewner's equation. For the mathematically inclined, a more detailed derivation can be found in [134]. Let us do this [97].

In Chapter 3 we defined the uniformizing map g_t as a conformal transformation that maps $\mathbb{H} \setminus \gamma_{[0,t]}$ to $\mathbb{H}$. The same way, for a given $dt > 0$ there is a map g_{t-dt} that takes $\mathbb{H} \setminus \gamma_{[0,t-dt]}$ to $\mathbb{H}$. We define a transition map $G_{t,dt} = g_t \circ g_{t-dt}^{-1}$ that maps $\mathbb{H} \setminus \gamma_{[0,t-dt]}$ to $\mathbb{H} \setminus \gamma_{[0,t]}$. For a reference of the relationship between these functions see Fig. 51.

We use the fact that a conformal map $f(z)$ is completely defined by its value on the boundary (which in the case of the upper half plane is the real line). The value of the function on the whole domain can be recovered by using the Schwartz integral formula [94]

$$f(z) = \frac{1}{\pi} \int_{-\infty}^{\infty} \frac{\text{Im } f(\xi)}{\xi - z} d\xi. \tag{A.1}$$

Since $\text{Im}\{\xi - f(z)\} = -\text{Im } f(z)$ for ξ real we can write

$$z - G_{t,dt}^{-1}(z) = \frac{1}{\pi} \int_a^b \frac{\text{Im } G_{t,dt}^{-1}(\xi)}{z - \xi} d\xi. \tag{A.2}$$

Where the interval $[a, b]$ is the (assumed finite) region where $\text{Im } G_{t,dt}^{-1}(z) > 0$. Making the substitution $z \to G_{t,dt}(z)$ we obtain

$$G_{t,dt}(z) - z = \frac{1}{\pi} \int_a^b \frac{\text{Im } G_{t,dt}^{-1}(\xi)}{G_{t,dt}(z) - \xi} d\xi. \tag{A.3}$$

Multiplying both sides by z and taking the limit $z \to \infty$ we obtain a formula for the half plane capacity

$$a_{t,dt} = \frac{1}{\pi} \int_a^b \text{Im } G_{t,dt}^{-1}(\xi)\, d\xi. \tag{A.4}$$

As mentioned in Section 3.1, the choice of capacity is mostly arbitrary, but a common choice is

$$a_t = 2t, \tag{A.5}$$

which, based on the additivity property

$$a_t = a_{t-dt} + a_{t,dt}, \tag{A.6}$$

yields the relation

$$\int_a^b \text{Im } G_{t,dt}^{-1}(\xi)\, d\xi = 2\pi dt. \tag{A.7}$$

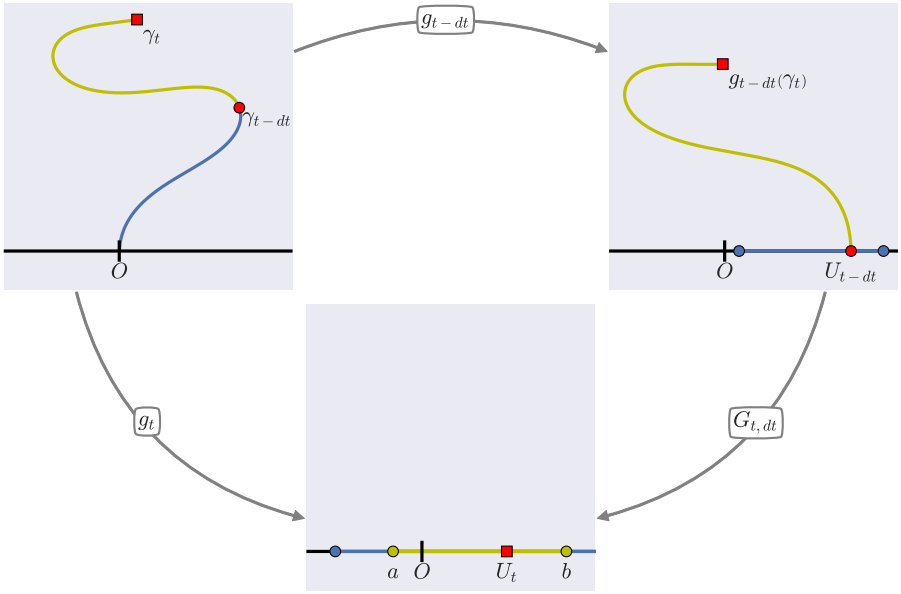

Figure 51 – Construction of the transition map $G_{t,dt} = g_t \circ g_{t-dt}^{-1}$. The interval $[a, b]$ is the region where $\text{Im}\, G_{t,dt}(z) > 0$.

We can now tackle the time derivative of the uniformizing map g_t

$$\frac{\partial g_t(z)}{\partial t} = \lim_{dt\to 0} \frac{g_t(z) - g_{t-dt}(z)}{dt}. \tag{A.8}$$

Using the fact that $g_t = G_{t,dt}(g_{t-dt}(z))$, and Eqs. A.3 and A.7 we obtain

$$\frac{\partial g_t(z)}{\partial t} = \lim_{dt\to 0} \frac{2}{\int_a^b \text{Im}\, G_{t,dt}^{-1}(\xi)\, d\xi} \int_a^b \frac{\text{Im}\, G_{t,dt}^{-1}(\xi)}{G_{t,dt}(g_{t-dt}(z)) - \xi} d\xi. \tag{A.9}$$

The second mean value theorem [135] for definite integrals states that it exists a $c \in (a, b]$ such that

$$\int_a^b G(\xi) f(\xi)\, d\xi = \lim_{y\to a^+} G(y) \int_a^c f(\xi)\, d\xi. \tag{A.10}$$

Applying that to Eq. A.9 leaves us with

$$\frac{\partial g_t(z)}{\partial t} = \lim_{dt\to 0} \frac{2}{G_{t,dt}(g_{t-dt}(z)) - a} \frac{\int_a^c \text{Im}\, G_{t,dt}^{-1}(\xi)\, d\xi}{\int_a^b \text{Im}\, G_{t,dt}^{-1}(\xi)\, d\xi}. \tag{A.11}$$

Since in the limit of $dt \to 0$, $\text{Im}\, G_{t,dt}^{-1}(z)$ is zero except for $z = U_t$, in other words, $a = b = U_t$. This means that the two integrals in Eq. A.11 take the same value and cancel each other. Add the fact that $\lim_{dt\to 0} G_{t,dt}$ is the identity map, and this leaves us with Loewner's equation

$$\frac{\partial g_t(z)}{\partial t} = \frac{2}{g_t(z) - U_t}. \tag{A.12}$$

Bibliography

1 DELATOUR, C. Exposé de quelques résultats obtenus par l'action combinée de la chaleur et de la compression sur certains liquides, tels que l'eau, l'alcool, l'ether sulfurique et l'essence de pétrole rectifiée. *Annales de Chimie et de Physique*, v. 21, p. 127–132, 1822.

2 ANDREWS, T. Bakerian lecture: On the continuity of the gaseous and liquid states of matter. *Proceedings of the Royal Society of London*, v. 18, p. 42–45, 1869.

3 CURIE, P. *Propriétés magnétiques des corps à diverses températures*. Paris: Gauthier-Villars et fils, 1895.

4 STANLEY, H. E. Scaling, universality, and renormalization: Three pillars of modern critical phenomena. *Review of Modern Physics*, v. 71, p. S358–S366, 1999.

5 GIBBS, J. W. *Elementary Principles in Statistical Mechanics*. New York: Charles Scribner's Sons, 1906.

6 ISING, E. Beitrag zur theorie des ferromagnetismus. *Zeitschrift für Physik*, v. 31, n. 1, p. 253–258, 1925.

7 ONSAGER, L. Crystal statistics. i. a two-dimensional model with an order-disorder transition. *Physical Review*, v. 65, p. 117–149, 1944.

8 BROADBENT, S. R.; HAMMERSLEY, J. M. Percolation processes. *Mathematical Proceedings of the Cambridge Philosophical Society*, v. 53, p. 629–641, 1957.

9 HELLER, P. Experimental investigations of critical phenomena. *Reports on Progress in Physics*, v. 30, n. 2, p. 731, 1967.

10 DOMB, C.; HUNTER, D. L. On the critical behaviour of ferromagnets. *Proceedings of the Physical Society*, v. 86, n. 5, p. 1147, 1965.

11 FISHER, M. E. The theory of equilibrium critical phenomena. *Reports on Progress in Physics*, v. 30, n. 2, p. 615, 1967.

12 STANLEY, H. E. *Introduction to Phase Transitions and Critical Phenomena*. Oxford: Clarendon Press, 1971.

13 KADANOFF, L. Scaling laws for Ising models near T_c. *Physics*, v. 2, n. 6, p. 263, 1966.

14 BELAVIN, A.; POLYAKOV, A.; ZAMOLODCHIKOV, A. Infinite conformal symmetry in two-dimensional quantum field theory. *Nuclear Physics B*, v. 241, n. 2, p. 333 – 380, 1984.

15 HENKEL, M. *Conformal invariance and critical phenomena*. New York: Springer Science & Business Media, 2013.

16 BAK, P.; TANG, C.; WIESENFELD, K. Self-organized criticality: An explanation of the $1/f$ noise. *Physical Review Letters*, v. 59, p. 381–384, 1987.

17 BAK, P. *how nature works, the science of self-organized criticality*. New York: Springer-Verlag, 1996.

18 CHRISTENSEN, K.; MOLONEY, N. *Complexity and Criticality*. London: Imperial College Press, 2005.

19 NIENHUIS, B. Critical behavior of two-dimensional spin models and charge asymmetry in the coulomb gas. *Journal of Statistical Physics*, v. 34, n. 5, p. 731–761, 1984.

20 MINNHAGEN, P. The two-dimensional coulomb gas, vortex unbinding, and superfluid-superconducting films. *Review of Modern Physics*, v. 59, p. 1001–1066, 1987.

21 LANGLANDS, R.; POULIOT, P.; SAINT-AUBIN, Y. Conformal invariance in two-dimensional percolation. *Bulletin of the American Mathematical Society*, v. 30, p. 1–61, 1994.

22 CARDY, J. SLE for theoretical physicists. *Annals of Physics*, v. 318, n. 1, p. 81–118, 2005.

23 LÖWNER, K. Untersuchungen über schlichte konforme abbildungen des einheitskreises. i. *Mathematische Annalen*, v. 89, n. 1, p. 103–121, 1923.

24 SCHRAMM, O. Scaling limits of loop-erased random walks and uniform spanning rees. *Israel Journal of Mathematics*, v. 118, n. 1, p. 221–288, 2000.

25 MACKENZIE, D. Perelman declines math's top prize; three others honored in madrid. *Science*, v. 313, n. 5790, p. 1027–1028, 2006.

26 KESTEN, H. The work of Stanislav Smirnov. In: BHATIA, R. (Ed.). *Proceedings of the International Congress of Mathematicians Hyderabad, India, 2010*. New Delhi: Hindustan Book Agency, 2010. v. 1, p. 73–84.

27 HENKEL, M. Schrödinger invariance and strongly anisotropic critical systems. *Journal of Statistical Physics*, v. 75, n. 5, p. 1023–1061, 1994.

28 BOYANOVSKY, D.; VEGA, H. J. D.; SCHWARZ, D. J. Phase transitions in the early and the present Universe. *Annual review of nuclear science*, v. 56, p. 441, 2006.

29 MATSUSHITA, M.; FUJIKAWA, H. Diffusion-limited growth in bacterial colony formation. *Physica A: Statistical Mechanics and its Applications*, v. 168, n. 1, p. 498 – 506, 1990.

30 FUKUI, M.; ISHIBASHI, Y. Self-organized phase transitions in cellular automaton models or pedestrians. *Journal of the Physical Society of Japan*, v. 68, n. 8, p. 2861–2863, 1999.

31 FISHER, D. S.; FISHER, M. P. A.; HUSE, D. A. Thermal fluctuations, quenched disorder, phase transitions, and transport in type-ii superconductors. *Physical Review B*, v. 43, p. 130–159, 1991.

32 CAMPOSTRINI, M. et al. Theoretical estimates of the critical exponents of the superfluid transition in ^{4}He by lattice methods. *Physical Review B*, v. 74, p. 144506, 2006.

33 SOLÉ, R. V. *Phase Transitions*. Princeton: Princeton University Press, 2011.

34 JAEGER, G. The Ehrenfest classification of phase transitions: Introduction and evolution. *Archive for History of Exact Sciences*, v. 53, n. 1, p. 51–81, 1998.

35 SENGERS, J. L. From Van der Waals equation to the scaling laws. *Physica*, v. 73, n. 1, p. 73 – 106, 1974.

36 KADANOFF, L. P. et al. Static phenomena near critical points: Theory and experiment. *Review of Modern Physics*, v. 39, p. 395–431, 1967.

37 AHLERS, G.; KORNBLIT, A.; SALAMON, M. B. Heat capacity of FeF_2 near the antiferromagnetic transition. *Physical Review B*, v. 9, p. 3932–3934, 1974.

38 AHLERS, G. Thermodynamics and experimental tests of static scaling and universality near the superfluid transition in He^4 under pressure. *Physical Review A*, v. 8, p. 530–568, 1973.

39 DIETRICH, O.; ALS-NIELSEN, J. Critical neutron scattering from beta-brass. In: US DEPARTMENT OF COMMERCE, NATIONAL BUREAU OF STANDARDS. *Critical Phenomena: Proceedings*. Washington, 1966. v. 13, p. 144.

40 GONZALO, J. A. Critical behavior of ferroelectric triglycine sulfate. *Physical Review*, v. 144, p. 662–665, 1966.

41 MA, S. keng. *Modern theory of critical phenomena*. New York: Perseus Publishing, 2000. (Advanced book classics).

42 CALLEN, H. B. *Thermodynamics and an Introduction to Thermostatistics*. 2nd. ed. Singapore: Wiley, 1985.

43 FERMI, E. *Thermodynamics*. New York: Dover Publications, 1956.

44 CHIARELLI, R. et al. A ferromagnetic transition at 1.48K in an organic nitroxide. *Nature*, v. 363, n. 6425, p. 147–149, 1993.

45 KEESOM, W. H.; KEESOM, A. P. New measurements on the specific heat of liquid helium. *Physica*, v. 2, n. 1, p. 557–572, 1935.

46 RESNICK, D. J. et al. Kosterlitz-Thouless transition in proximity-coupled superconducting arrays. *Physical Review Letters*, v. 47, p. 1542–1545, 1981.

47 KOSTERLITZ, J. M.; THOULESS, D. J. Ordering, metastability and phase transitions in two-dimensional systems. *Journal of Physics C: Solid State Physics*, v. 6, n. 7, p. 1181, 1973.

48 LANDAU, L. D.; LIFSHITZ., E. M. *Statistical physics Part 1*. 3. ed. Oxford: Pergamon, 1969. (Course of Theoretical Physics, v. 5).

49 WILSON, K. G.; FISHER, M. E. Critical exponents in 3.99 dimensions. *Physical Review Letters*, v. 28, p. 240–243, 1972.

50 EL-SHOWK, S. et al. Solving the 3D Ising model with the conformal bootstrap ii. c-minimization and precise critical exponents. *Journal of Statistical Physics*, v. 157, n. 4, p. 869–914, 2014.

51 GUILLOU, J. C. L.; ZINN-JUSTIN, J. Critical exponents for the n-vector model in three dimensions from field theory. *Physical Review Letters*, v. 39, p. 95–98, 1977.

52 WU, F. Y. The Potts model. *Review of Modern Physics*, v. 54, p. 235–268, 1982.

53 SMIRNOV, S.; WERNER, W. Critical exponents for two-dimensional percolation. *arXiv preprint math/0109120*, 2001.

54 KIM, H. K.; CHAN, M. H. W. Experimental determination of a two-dimensional liquid-vapor critical-point exponent. *Physical Review Letters*, v. 53, p. 170–173, 1984.

55 VOSS, R. F. The fractal dimension of percolation cluster hulls. *Journal of Physics A: Mathematical and General*, v. 17, n. 7, p. L373, 1984.

56 LAWLER, G. F.; SCHRAMM, O.; WERNER, W. One-arm exponent for critical 2d percolation. *arXiv preprint math/0108211*, 2001.

57 AIZENMAN, M.; DUPLANTIER, B.; AHARONY, A. Path-crossing exponents and the external perimeter in 2d percolation. *Physical Review Letters*, v. 83, p. 1359–1362, 1999.

58 RUSHBROOKE, G. S. On the thermodynamics of the critical region for the Ising problem. *The Journal of Chemical Physics*, v. 39, n. 3, p. 842–843, 1963.

59 GRIFFITHS, R. B. Thermodynamic functions for fluids and ferromagnets near the critical point. *Physical Review*, v. 158, p. 176–187, 1967.

60 NISHIMORI, G. O. H. *Elements of Phase Transitions and Critical Phenomena*. Oxford: Oxford University Press, USA, 2011.

61 PELISSETTO, A.; VICARI, E. Critical phenomena and renormalization-group theory. *Physics Reports*, v. 368, n. 6, p. 549 – 727, 2002.

62 PEIERLS, R. On Ising's model of ferromagnetism. *Mathematical Proceedings of the Cambridge Philosophical Society*, v. 32, p. 477–481, 1936.

63 PATHRIA, R. K. *Statistical Mechanics*. 2nd. ed. Oxford: Elsevier, 1996.

64 YANG, C. N. The spontaneous magnetization of a two-dimensional Ising model. *Physical Review*, v. 85, p. 808–816, 1952.

65 STAUFFER, A. A. D. *Introduction to percolation theory*. 2. ed. Boca Raton, FL: CRC Press, 1994.

66 KIRKPATRICK, S. Percolation and conduction. *Review of Modern Physics*, v. 45, p. 574–588, 1973.

67 NEWMAN, M. E. J.; ZIFF, R. M. Efficient Monte Carlo algorithm and high-precision results for percolation. *Physical Review Letters*, v. 85, p. 4104–4107, 2000.

68 CANDIA, A. de et al. Colloidal gelation, percolation and structural arrest. *Physica A: Statistical Mechanics and its Applications*, v. 358, n. 2–4, p. 239 – 248, 2005.

69 AMBEGAOKAR, V.; HALPERIN, B. I.; LANGER, J. S. Hopping conductivity in disordered systems. *Physical Review B*, v. 4, p. 2612–2620, 1971.

70 STEWART, J.; VARELA, F. J. Morphogenesis in shape-space. elementary meta-dynamics in a model of the immune network. *Journal of Theoretical Biology*, v. 153, n. 4, p. 477 – 498, 1991.

71 SAHIMI, M. *Applications of Percolation Theory*. Boca Raton, Florida: CRC Press, 1994.

72 ARAÚJO, E. B. et al. Geometrical and transport properties of sequential adsorption clusters. *International Journal of Modern Physics C*, v. 24, n. 06, p. 1350031, 2013.

73 ACHLIOPTAS, D.; D'SOUZA, R. M.; SPENCER, J. Explosive percolation in random networks. *Science*, v. 323, n. 5920, p. 1453–1455, 2009.

74 WILKINSON, D.; WILLEMSEN, J. F. Invasion percolation: a new form of percolation theory. *Journal of Physics A: Mathematical and General*, v. 16, n. 14, p. 3365, 1983.

75 HENKEL, M.; PLEIMLING, M. Local scale invariance as dynamical space-time symmetry in phase-ordering kinetics. *Physical Review E*, v. 68, p. 065101, 2003.

76 HENKEL, M. On the two-point correlation function in dynamical scaling and Schrödinger invariance. *International Journal of Modern Physics C*, v. 03, n. 05, p. 1011–1017, 1992.

77 HENKEL, M.; PLEIMLING, M. *Non-Equilibrium Phase Transitions Volume 2: Ageing and Dynamical Scaling Far from Equilibrium*. London: Springer, 2010.

78 ENGLMAN, R.; JAEGER, Z. *Fragmentation, form, and flow in fractured media: proceedings of the F3-Conference held at Neve Ilan (Israel), 6-9 January, 1986*. Michigan: A. Hilger, 1986. (Annals of the Israel Physical Society).

79 DAYAN, I.; GOUYET, J. F.; HAVLIN, S. Percolation in multi-layered structures. *Journal of Physics A: Mathematical and General*, v. 24, n. 6, p. L287, 1991.

80 JÁCOME, S. S. B. *Dynamic and Structural Aspects in Networks Models for Complex Systems*. Tese (Doutorado) — Universidade Federal do Ceará, Fortaleza, 2009.

81 PARTELI, E. J. R.; SILVA, L. R. da; JR, J. S. A. Self-organized percolation in multi-layered structures. *Journal of Statistical Mechanics: Theory and Experiment*, v. 2010, n. 03, p. P03026, 2010.

82 HENKEL, M.; HINRICHSEN, H.; LÜBECK, S. *Non-Equilibrium Phase Transitions Volume 1: Absorbing Phase Transitions*. Bristol: Springer, 2008.

83 HINRICHSEN, H. Non-equilibrium critical phenomena and phase transitions into absorbing states. *Advances in Physics*, v. 49, n. 7, p. 815–958, 2000.

84 OWCZAREK, A. L. et al. On the hulls of directed percolation clusters. *Journal of Physics A: Mathematical and General*, v. 30, n. 19, p. 6679, 1997.

85 LEMOULT, G. et al. Directed percolation phase transition to sustained turbulence in Couette flow. *Nature Physics*, v. 12, n. 3, p. 254–258, 2016.

86 DOMB, C.; LEBOWITZ, J. L. *Phase transitions and critical phenomena*. London: Academic Press, 1987.

87 WILSON, D. B. Red-green-blue model. *Physical Review E*, v. 69, p. 037105, 2004.

88 FRANCESCO, P. D.; MATHIEU, P.; SÉNÉCHAL, D. *Conformal Field Theory*. New York: Springer-Verlag, 1997.

89 STILLWELL, J. Analytic geometry. In: *Mathematics and Its History*. New York, NY: Springer, 2010. p. 109–125.

90 THIRRING, W. E. A soluble relativistic field theory. *Annals of Physics*, v. 3, n. 1, p. 91 – 112, 1958.

91 NAHM, W. Conformal field theory: a bridge over troubled waters. In: *Quantum Field Theory - A Twentieth Century Profile*. New Delhi: Hindustani Book Agency, 2000. p. 571–604.

92 LAWLER, G.; SCHRAMM, O.; WERNER, W. The dimension of the planar Brownian frontier is 4/3. *Mathematical research letters*, v. 8, n. 1, p. 13–24, 2001.

93 DEBRANGES, L. A proof of the Bieberbach conjecture. *Acta Mathematica*, v. 154, n. 1, p. 137–152, 1985.

94 AHLFORS, L. V. *Complex analysis: an introduction to the theory of analytic functions of one complex variable*. Auckland: McGraw-Hill, 1979.

95 DRISCOLL, T. A.; TREFETHEN, L. N. *Schwarz-Christoffel Mapping*. Cambrige, UK: Cambridge University Press, 2002.

96 DRISCOLL, T. A. Algorithm 843: Improvements to the Schwarz-Christoffel toolbox for MATLAB. *ACM Transactions on Mathematical Software*, v. 31, n. 2, p. 239–251, 2005.

97 KAGER, W.; NIENHUIS, B. A guide to stochastic Löwner evolution and its applications. *Journal of Statistical Physics*, v. 115, n. 5, p. 1149–1229, 2004.

98 LAWLER, G. F.; SHEFFIELD, S. A natural parametrization for the Schramm—Loewner evolution. *The Annals of Probability*, v. 39, n. 5, p. 1896–1937, 2011.

99 GRUZBERG, I. A.; KADANOFF, L. P. The Loewner equation: Maps and shapes. *Journal of Statistical Physics*, v. 114, n. 5, p. 1183–1198, 2004.

100 HENKEL, M.; KAREVSKI, D. *Conformal Invariance: an Introduction to Loops, Interfaces and Stochastic Loewner Evolution*. New York: Springer, 2012.

101 ASH, R. B.; DOLEANS-DADE, C. *Probability and measure theory*. San Diego: Academic Press, 2000.

102 DURRETT, R. *Stochastic calculus: a practical introduction*. New York: CRC press, 1996.

103 ROHDE, S.; SCHRAMM, O. Basic properties of SLE. In: BENJAMINI, I.; HÄGGSTRÖM, O. (Ed.). *Selected Works of Oded Schramm*. New York, NY: Springer New York, 2011. p. 989–1030.

104 MANDELBROT, B. B. *The fractal geometry of nature*. London: Macmillan, 1983.

105 BEFFARA, V. The dimension of the SLE curves. *The Annals of Probability*, Institute of Mathematical Statistics, v. 36, n. 4, p. 1421–1452, 2008.

106 BAUER, M.; BERNARD, D. SLE_κ growth processes and conformal field theories. *Physics Letters B*, v. 543, n. 1–2, p. 135–138, 2002.

107 DUPLANTIER, B. Conformally invariant fractals and potential theory. *Physical Review Letters*, v. 84, p. 1363–1367, 2000.

108 BEFFARA, V. Hausdorff dimensions for SLE_6. *The Annals of Probability*, v. 32, n. 3, p. 2606–2629, 2004.

109 KENNEDY, T. Monte Carlo tests of stochastic Loewner evolution predictions for the 2D self-avoiding walk. *Physical Review Letters*, v. 88, p. 130601, 2002.

110 CHELKAK, D. et al. Convergence of Ising interfaces to Schramm's SLE curves. *Comptes Rendus Mathematique*, v. 352, n. 2, p. 157 – 161, 2014.

111 SCHRAMM, O.; SHEFFIELD, S. Harmonic explorer and its convergence to SLE_4. *The Annals of Probability*, v. 33, n. 6, p. 2127–2148, 2005.

112 SMIRNOV, S. Critical percolation in the plane: conformal invariance, Cardy's formula, scaling limits. *Comptes Rendus de l'Académie des Sciences - Series I - Mathematics*, v. 333, n. 3, p. 239 – 244, 2001.

113 BERNARD, D. et al. Conformal invariance in two-dimensional turbulence. *Nature Physics*, v. 2, n. 2, p. 124–128, Feb 2006.

114 THALABARD, S. et al. Conformal invariance in three-dimensional rotating turbulence. *Physical Review Lett.*, v. 106, p. 204503, 2011.

115 POSÉ, N. et al. Shortest path and Schramm-Loewner evolution. *Scientific Reports*, v. 4, p. 5495EP, 2014.

116 DARYAEI, E. et al. Watersheds are Schramm-Loewner evolution curves. *Physical Review Letters*, v. 109, p. 218701, 2012.

117 RUSHKIN, I. et al. Stochastic loewner evolution driven by lévy processes. *Journal of Statistical Mechanics: Theory and Experiment*, v. 2006, n. 01, p. P01001, 2006.

118 OIKONOMOU, P. et al. Global properties of stochastic Loewner evolution driven by Lévy processes. *Journal of Statistical Mechanics: Theory and Experiment*, v. 2008, n. 01, p. P01019, 2008.

119 PRESS, W. H. et al. *Numerical recipes 3rd edition: The art of scientific computing*. Cambridge, UK: Cambridge university press, 2007.

120 BAUER, R. O. Discrete Löwner evolution. *Annales de la Faculté des sciences de Toulouse : Mathématiques*, v. 12, n. 4, p. 433–451, 2003.

121 KENNEDY, T. Numerical computations for the Schramm-Loewner evolution. *Journal of Statistical Physics*, v. 137, n. 5, p. 839–856, 2009.

122 KAGER, W.; NIENHUIS, B.; KADANOFF, L. P. Exact solutions for Loewner evolutions. *Journal of Statistical Physics*, v. 115, n. 3, p. 805–822, 2004.

123 KENNEDY, T. A fast algorithm for simulating the chordal Schramm–Loewner evolution. *Journal of Statistical Physics*, v. 128, n. 5, p. 1125–1137, 2007.

124 ZIFF, R. M. Test of scaling exponents for percolation-cluster perimeters. *Physical Review Letters*, v. 56, p. 545–548, 1986.

125 PENG, C.-K. et al. Long-range anticorrelations and non-gaussian behavior of the heartbeat. *Physical Review Letters*, v. 70, p. 1343–1346, 1993.

126 HARDSTONE, R. et al. Detrended fluctuation analysis: a scale-free view on neuronal oscillations. *Frontiers in physiology*, v. 3, 2012.

127 MATOS, J. A. et al. Time and scale Hurst exponent analysis for financial markets. *Physica A: Statistical Mechanics and its Applications*, v. 387, n. 15, p. 3910 – 3915, 2008.

128 DAVIES, R. B.; HARTE, D. S. Tests for hurst effect. *Biometrika*, v. 74, n. 1, p. 95–101, 1987.

129 Frigo, M.; Johnson, S. G. *FFTW: Fastest Fourier Transform in the West*. 2012. Astrophysics Source Code Library.

130 HU, K. et al. Effect of trends on detrended fluctuation analysis. *Physical Review E*, v. 64, p. 011114, 2001.

131 CHEN, Z. et al. Effect of nonstationarities on detrended fluctuation analysis. *Physical Review E*, v. 65, p. 041107, 2002.

132 MANDELBROT, B. B.; NESS, J. W. V. Fractional brownian motions, fractional noises and applications. *SIAM Review*, v. 10, n. 4, p. 422–437, 1968.

133 CHE, S. et al. A performance study of general-purpose applications on graphics processors using CUDA. *Journal of Parallel and Distributed Computing*, v. 68, n. 10, p. 1370 – 1380, 2008.

134 MONACO, A. del; GUMENYUK, P. Chordal Loewner equation. *arXiv preprint arXiv:1302.0898*, 2013.

135 COMENETZ, M. *Calculus: The elements*. River Edge, NJ: World Scientific, 2002.